POLITECNICO DI TORINO

Master's Degree in Biomedical Engineering

Master's Degree Thesis

Hand Gesture Recognition: Multichannel sEMG-driven Classification for Finger-level Motor Rehabilitation

Supervisors

Prof. Danilo DEMARCHI

Ph.D. Fabio ROSSI

Ph.D. Andrea MONGARDI

M.Sc. Andrea PRESTIA

Candidate

Nicolò TOSETTO

March 2025

Summary

In recent years, the need to enhance interaction between therapists and patients during rehabilitation sessions has grown, leading to the increasing use of engineering systems that incorporate algorithms for movement recognition. This work focuses on developing a classifier for finger gestures, as hand rehabilitation is crucial for post-stroke patients with motor impairments that may prevent or hinder their movements.

This thesis proposes the development of a classifier that uses an Artificial Neural Network (ANN) to recognize and differentiate hand movements. Specifically, the study focuses on finger movements, such as counting, which are essential for hand functionality and rehabilitation. A preliminary study was conducted using the publicly available GRABMyo and Hyser datasets to extract valuable information for constructing a custom dataset. The GRABMyo dataset provided insights into inter-subject variability. The Hyser dataset was used to generate power maps, highlighting major activation points for different movements, which were then used to develop a protocol for positioning the acquisition devices.

The acquisition system consisted of six acquisition devices developed by the eLiONS research group. These devices simultaneously acquire surface ElectroMyo-Graphy (sEMG) and Average Threshold Crossing (ATC) signals using dedicated Python software.

A total of seven different movements (Hand Close, Thumb up, One, Two, Three, Four, Five), along with the idle state, were recorded. The recording process was supported by a user-friendly GUI for real-time monitoring and control, along with a dedicated interface to guide the subject and improve recording quality.

After a pre-processing step, the features for the classification were extracted, and feature selection was performed using PCA, identifying 10 features sufficient to explain 95% of the variance in the sEMG signal. The final dataset includes 24 healthy subjects, 21 of which were used for training and 3 for testing. Two classifiers were built: one including all previously introduced movements and one excluding the two most difficult movements to classify.

The classifier, considering all the movements, yielded an average per-class accuracy of 92.88% and an F1 score of 71.84%. A separate classifier was developed

by excluding the two most challenging movements to discriminate, resulting in significant improvement across all metrics, among which an accuracy of 95.53% and F1 score of 86.86%.

A final test was performed using only one subject for both training and testing, with acquisitions on different days to assess the classifier's performance with a single subject. For the classifier considering all movements, the accuracy was 96.82% and the F1 score was 87.30%. For the classifier excluding the two most challenging movements to recognize, the accuracy increased to 98.53%, and the F1 score reached 95.60%. The performance difference between the classifier trained on all subjects and the single-subject classifier is attributed to the well-documented inter-subject variability in the literature. Consequently, the relatively small number of subjects may affect generalization.

In conclusion, the proposed method represents a robust approach for developing a hand gesture recognition classifier, without the need for a high-density acquisition device, achieving high performance across the evaluation metrics. The classifier effectively discriminates finger movements using an acquisition setup that relies on features extracted from sEMG signals.

Acknowledgements

I would like to express my gratitude to Danilo Demarchi for giving me the opportunity to work on this thesis. I am also deeply grateful to Andrea Prestia, Fabio Rossi, and Andrea Mongardi for their constant support and availability throughout the development of this thesis project.

Finally, I would like to thank my family and friends for their unwavering support and encouragement throughout my years at university. *Desidero esprimere la mia*

sincera gratitudine al Professor Danilo Demarchi per avermi offerto l'opportunità di lavorare a questa tesi. Inoltre, sono profondamente grato a Andrea Prestia, Fabio Rossi e Andrea Mongardi per il loro costante supporto e la loro disponibilità durante lo sviluppo di questo progetto di tesi.

Infine, rivolgo un sentito ringraziamento alla mia famiglia e ai miei amici per il sostegno e l'incoraggiamento dimostrati nel corso degli anni di università.

Table of Contents

List of Figures

List of Tables

Acronyms

AFE
: Analog Front End

AI
: Artificial intelligence

ANN
: Artificial Neural Network

APIs
: Application Programming Interfaces

ARV
: Absolute Rectified Values

ATC
: Average Threshold Crossing

BLE
: Bluetooth Low Energy

CNN
: Convolutional Neural Network

CPU
: Central Processing Unit

CV
: Conduction Velocity

DCN
: Deformable Convolutional Network

DIP
: Distal Interphalangeal

DL
: Deep Learning

EB
: Event Based

ECG
: ElectroCardioGraphy

EEG
: ElectroEncephaloGraphy

FD
: Frequency Domain

FES
: Functional Electrical Stimulation

GPU
: Graphics Processing Unit

GUI
: Graphical User Interface

HD
: High Density

Hyser
: High-Density Surface Electromyogram Recordings

IED
: Inter-Electrode Distance

IS

Information Synthesis

MCP

MetaCarpoPhalangeal

ML

Machine Learning

MUAP

Motor Unit Action Potential

NAN

Not A Number

NMJ

Neuromuscular Junction

OOP

Object-Oriented Programming

PR

Proprioception Recognition

PCA

Principal Component Analysis

PSD

Power Spectral Density

ReLU

Rectified Linear Unit

RMS

Root Mean Square

SCI

Spinal Cord Injury

sEMG
Surface Electromyography

SNR
Signal-to-Noise Ratio

TC
Threshold Crossing

TD
Time Domain

Chapter 1

Introduction

The anatomy of the hand plays a pivotal role in distinguishing Homo sapiens from other species and has contributed significantly to our evolutionary development. The opposition of the thumb is of particular importance, as it enables manipulating and grasping objects, thereby facilitating the development of manual dexterity. The human hand exhibits 19 degrees of freedom, comprising synchronized structures to enable precise and intricate movements [1]. Key components include the thenar muscles, which are responsible for critical functions in thumb movement and opposition and are located at the base of the thumb [2]. Additionally, the intrinsic muscles, intricately woven within the hand, play pivotal roles in fine motor control and grip strength. Furthermore, the extensor and flexor muscles of the forearm, spanning across the wrist joint, contribute significantly to wrist stability and coordinated movement. The MetaCarpoPhalangeal (MCP) joint, a pivotal hinge joint connecting the metacarpal bones to the proximal phalanges, enables crucial movements such as flexion, extension, abduction, and adduction, thus contributing significantly to hand function and mobility. Together, these anatomical elements form a sophisticated network, facilitating the remarkable range of motion and precision of human hand function [2]. Moreover, the presence of the median, ulnar, and radial nerve, and their respective branches, orchestrates sensory and motor innervation, ensuring optimal sensory feedback and motor coordination throughout the hand and wrist.

The development of classifiers for hand gesture recognition using artificial intelligence plays a pivotal role in the field of rehabilitation engineering. Such systems are essential for controlling prosthetic devices, exoskeletons, and other assistive technologies, offering individuals with motor impairments a means of regaining functionality and independence. Artificial Intelligence (AI)-based classifiers, particularly those utilizing machine learning and deep learning algorithms, allow for precise and adaptable gesture recognition, crucial for tailoring rehabilitation processes to the specific needs of each patient. By analyzing biosignals such as surface electromyography, these systems can interpret subtle muscle activations, enabling real-time feedback that is vital for effective neurorehabilitation and improving patient outcomes.

This thesis, of which the pipeline is shown in Figure 1.1, focuses on the development of a classifier for hand gesture recognition, specifically designed to classify fine motor movements such as finger counting. These movements are often associated with more complex hand functions, which are crucial for rehabilitation, particularly after neurological impairments such as stroke. The research is part of a larger project that integrates both movement recognition and neuromuscular stimulation using the Rehastim2 device. The overarching goal of this project is to create a comprehensive acquisition and feedback system that not only recognizes gestures in real-time but also provides appropriate stimulation in response.

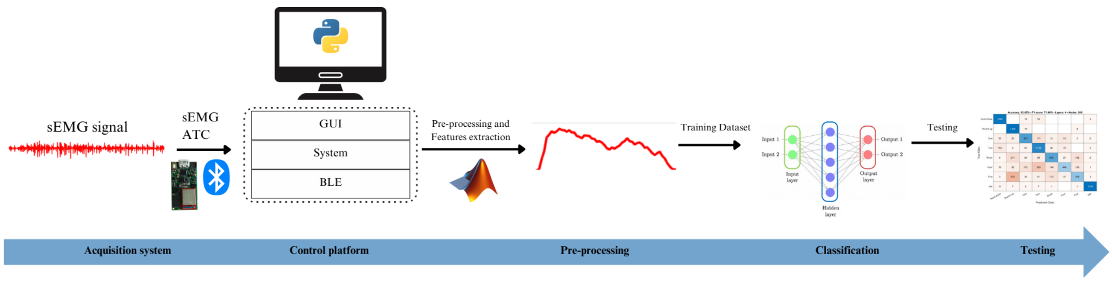

Figure 1.1: Thesis work complete pipeline.

The proposed system is built around a setup that includes sensors to capture surface ElectroMyoGraphy (sEMG) signals from a healthy therapist performing specific hand movements. These signals are processed to identify distinct patterns associated with each gesture. Once a movement is recognized, the system triggers the Rehastim2 device to deliver a stimulation profile to the patient, specifically designed to induce the corresponding movement. This stimulation profile is determined through a calibration process that adapts to the patient's neuromuscular characteristics, ensuring personalized and effective stimulation.

The real-time functionality of the classifier allows the therapist to actively guide the rehabilitation session by executing predefined movements, while the system continuously monitors and recognizes these gestures. The corresponding stimulation is then applied to the patient, reinforcing neuromuscular pathways and promoting functional recovery. By integrating gesture recognition from the therapist and neuromuscular stimulation in the patient, the system provides immediate and adaptive feedback, enhancing the rehabilitation experience.

The ultimate goal of the project is to support individuals with motor impairments, particularly stroke survivors, by offering a personalized and adaptive rehabilitation approach. The combination of real-time gesture classification and tailored stimulation aims to optimize therapy effectiveness, facilitating motor recovery by dynamically adapting to the patient's progress.

1.1 Thenar muscles

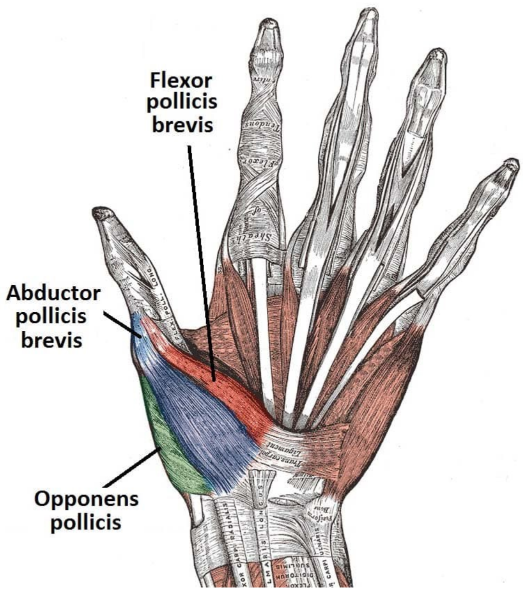

Figure 1.2: Thenar muscles [3].

The thumb's *thenar muscles* [4] are intrinsic muscles of the thumb situated at its base as it showed in Figure 1.2, lying on the palmar side along the first metacarpal bone [5]. Three thenar muscles form that so-called "thenar eminence," which is the bulge on the palmar side; those three muscles are:

- Abductor pollicis brevis;
- Flexor pollicis brevis;
- Opponens pollicis.

Abductor pollicis brevis: it extends along the radial side of the hand; it is involved in the abduction of the thumb, which is the movement of the thumb away from the other fingers.

Flexor pollicis brevis: it is primarily involved in the thumb flexion at the metacarpophalangeal joint. Additionally, it assists in opposition and adduction of the thumb, helping to bring the thumb across the palm and toward the other fingers. These movements are essential for grasping and manipulating objects.

Opponens pollicis: it is primarily responsible for opposing the thumb and moving the thumb toward the other fingers of the hand. This action is crucial for grasping objects between the thumb and fingers, a movement known as precision grip. Additionally, the opponens pollicis stabilizes the thumb during pinch and grip activities.

1.2 Hypothenar muscles

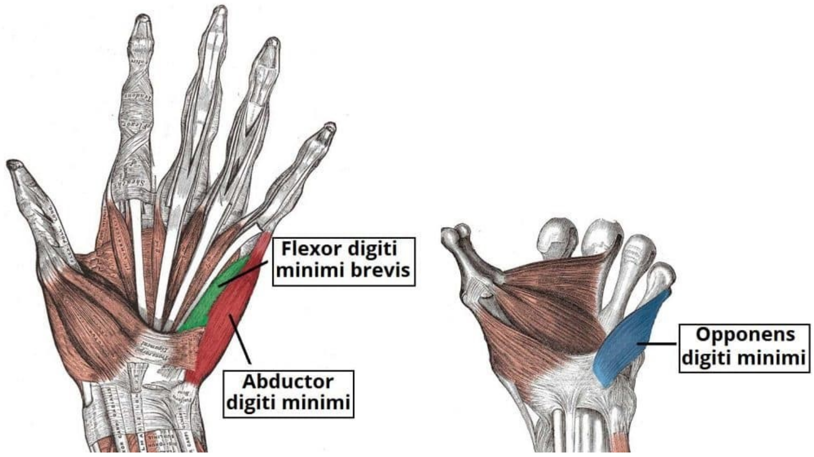

Figure 1.3: Hypothenar muscles [3].

The *hypothenar muscles* (Figure 1.3) primarily regulate little finger movements and play essential roles in diverse hand functions. Situated on the ulnar side of the hand [6], they constitute a prominence on the medial palmar surface known as the hypothenar eminence, although less conspicuous than the thenar eminence. The hypothenar muscles consist of four key muscles:

- Abductor digiti minimi;
- Flexor digiti minimi brevis;
- Opponens digiti minimi;
- Palmaris brevis.

The *abductor digiti minimi* functions similarly to the abductor pollicis brevis muscle, directing the little finger away from the midline.

The *flexor digiti minimi brevis* facilitates flexion of the little finger at the metacarpophalangeal joint.

The *opponens digiti minimi* muscle enables opposition movement of the little finger, allowing it to move towards the thumb.

The *palmaris brevis muscle* contributes to the wrinkling of the skin on the hand's palmar surface and protects the ulnar nerve.

1.3 Extrinsic muscles on the forearm

1.3.1 Muscles on the anterior side

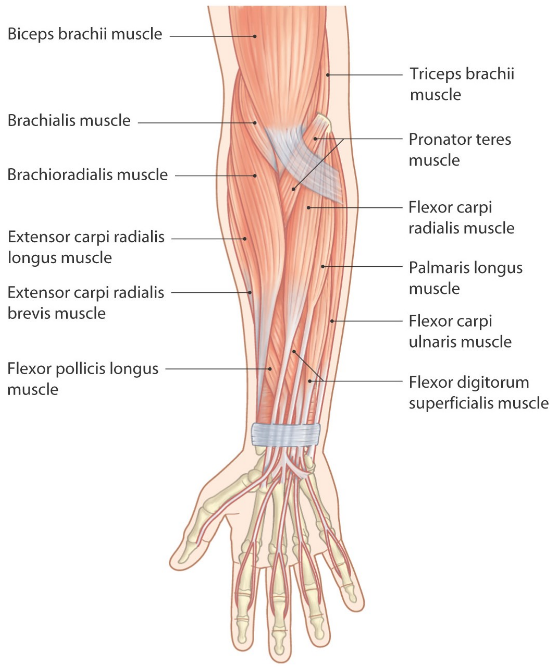

Figure 1.4: Anatomic representation of the extrinsic muscles on the anterior side of the forearm [7].

The muscles in the anterior forearm (Figure 1.4)can be divided into superficial, intermediate, and deep groups [8] [2]. The superficial group of muscles comprises:

- Flexor carpi radialis;
- Palmaris longus;
- Flexor carpi ulnaris.

The flexor carpi ulnaris is innervated by the ulnar nerve, while the palmaris longus and the flexor carpi radialis are innervated by the median nerve. *Flexor carpi radialis*: it is involved in wrist flexion and wrist abduction.

Palmaris longus: it is involved in wrist flexion; notably, this muscle is less prominent or as strong as other forearm muscles.

Flexor carpi ulnaris: it is involved in wrist flexion and ulnar deviation.

In the intermediate group, only the *flexor digitorum superficialis*, which is involved in the flexion of the wrist, metacarpophalangeal, and proximal interphalangeal joints of digits 2-5. The median nerve innervates this muscle.

The deep group of muscles includes the *flexor digitorum profundus* and the *flexor pollicis longus*. The flexor digitorum profundus plays a crucial role in flexing the fingers. Its primary function is to flex the distal interphalangeal joints (DIP), the joints closest to the fingertips. It also has a small role in wrist flexion. The *flexor pollicis longus* is responsible for thumb flexion

1.3.2 Muscles on the posterior side

The muscles on the posterior side of the forearm can be divided into superficial and deep groups [8] [5]. The muscles in the superficial group are:

- Extensor carpi radialis longus;
- Extensor carpi radialis brevis;
- Extensor digitorum;
- Extensor digiti minimi;
- Extensor carpi ulnaris.

Extensor carpi radialis longus: its primary function is wrist stabilization and is involved in wrist extension and radial deviation.

Extensor carpi radialis brevis: its primary function is wrist straightening and stabilization during power grasp, but it is also involved in wrist extension and radial deviation.

Extensor digitorum: It provides the ability to straighten the index, middle, ring, and small finger, thus involved in finger extension and wrist extension.

Extensor digiti minimi: It is used during the extension of the little finger.

Extensor carpi ulnaris: Its primary function is wrist straightening and stabilization, and it also provides the ability to move the wrist away from the thumb. Therefore, it is involved in wrist extension and adduction.

The deep group includes:

- Abductor pollicis longus;

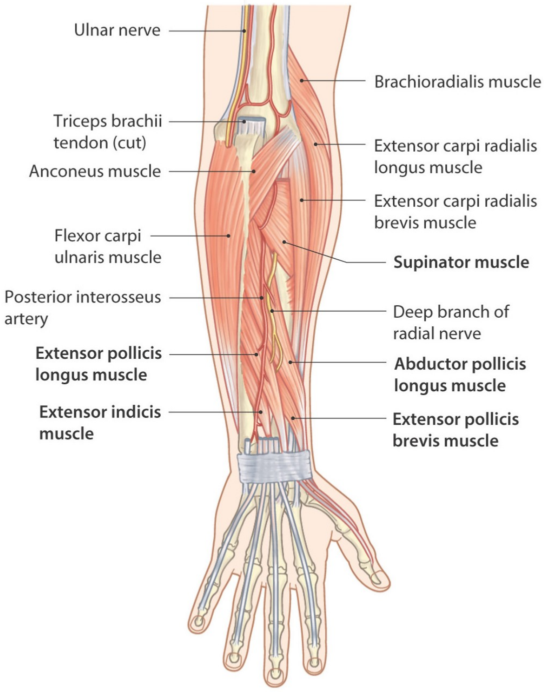

Figure 1.5: Anatomic representation of the extrinsic muscles on the posterior side of the forearm [9].

- Extensor pollicis longus;
- Extensor pollicis brevis;
- Extensor indicis.

Abductor pollicis longus: it is involved in thumb abduction.

Extensor pollicis longus: it extends the thumb at the interphalangeal joint, and the metacarpophalangeal joint is responsible for thumb straightening.

Extensor pollicis brevis works with the longus to extend the thumb.

Extensor indicis extends the index finger at the metacarpophalangeal and interphalangeal joint, providing the ability to independently straighten the index finger, as it has no junction connecting it to other extensor tendons.

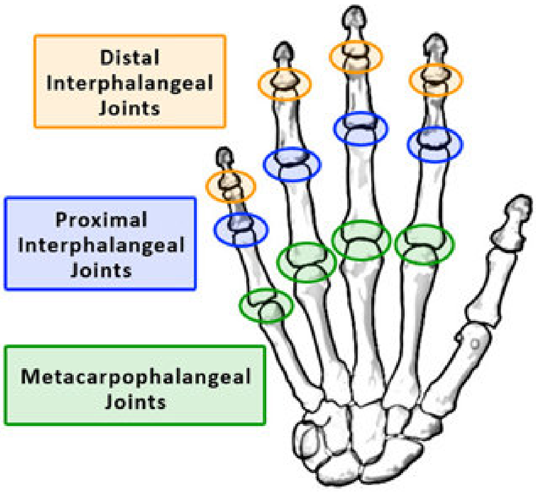

Figure 1.6: Anatomy of finger joints, including metacarpophalangeal, proximal interphalangeal, and distal interphalangeal joints [10].

1.4 Finger joints

1.4.1 The metacarpophalangeal joint

It connects the metacarpal bones to the fingers and is classified as synovial. There are five separate MCP joints, each connecting a metacarpal bone to the corresponding proximal phalanx of the finger. The primary movements supported by the MCP joint include flexion, extension, abduction, adduction, circumduction, and limited rotation. These joints contribute to the stability and flexibility of the fingers, a function facilitated by the presence of ligaments, joint capsules, and adjacent musculotendinous structures.

The metacarpophalangeal joint is surrounded by a fibrous capsule firmly anchored along the edges of the articular facets. This capsule exhibits greater thickness and reinforcement on its medial and lateral aspects through collateral ligaments, that are the major stabilizers of the MCP. Additionally, anteriorly, the joint capsule is supplemented by the palmar metacarpophalangeal ligament, while posteriorly, it receives contributions from the tendons of the forearm's long extensor muscles.

There are two collateral ligaments: The *proper collateral ligaments* originate from the posterior tubercles positioned on the dorsolateral aspect of the metacarpal head, extending towards the palmar aspect of the adjacent proximal phalanx, just distal to its base. Their primary function is constraining excessive MCP joint flexion, ensuring stability during movement.

In contrast, the *accessory collateral ligaments* originate closer to the metacarpal head and extend distally to attach onto the distal third of the palmar, or volar, plate. These ligaments exert tension during extension, effectively restricting such movement within the joint and contributing to its overall integrity and functionality.

The palmar ligament, also known as the volar plate, constitutes a dense fibrocartilaginous structure that forms a robust thickening along the palmar aspect of the MCP joint capsule. While loosely attached to the palmar aspect of the metacarpal neck, it exhibits firm adherence to the palmar surface of the base of the adjacent proximal phalanx. Its lateral margins seamlessly integrate with the collateral ligaments, enhancing joint stability and functionality.

Within the thumb, the palmar ligament houses two sesamoid bones, establishing articulations with palmar facets on the metacarpal head. The principal role of this ligamentous structure is to counteract hyperextension of the MCP joint, thereby safeguarding against excessive joint movement and ensuring optimal hand biomechanics.

The deep, transverse metacarpal ligaments are slender fibrous bands extending across the palmar aspect of the second to fifth metacarpophalangeal joints, effectively linking them. Positioned anteriorly to the interossei muscles and posteriorly to the lumbricals, these ligaments exhibit connections with the palmar surfaces of the digital slips associated with the central palmar aponeurosis. Primarily, their function revolves around bolstering the stability of the metacarpophalangeal joints during manual gripping maneuvers.

Muscle acting on the metacarpophalangeal joints

Thumb flexion primarily involves the flexor pollicis brevis, supported by the flexor pollicis longus muscle. For digits 2 to 5, flexion is orchestrated by the flexor digitorum superficialis, flexor digitorum profundus, lumbricals, and flexor digiti minimi brevis. Thumb extension, particularly from a flexed position, is chiefly executed by the extensor pollicis brevis, with supplementary assistance from the extensor pollicis longus muscle. The extension of digits 2 to 5 is managed by the extensor digitorum, extensor indicis (second digit), and extensor digiti minimi (fifth digit). The adductor pollicis facilitate adduction of the thumb, while the palmar interossei muscles accomplish adduction of the remaining four digits.Thumb abduction relies on the coordinated action of the abductor pollicis longus and abductor pollicis brevis muscles, whereas the abductor digit minimi governs the abduction of the fifth digit. Abduction of fingers 2-5 is attributed to the dorsal interossei muscles. Axial rotation is actively induced by the simultaneous contraction of the flexor pollicis brevis and abductor pollicis brevis muscles.

1.4.2 Interphalangeal joints of the hand

They are classified as synovial joints. They are subdivided into proximal Interphalangeal joints, situated between the proximal and middle phalanges, and distal interphalangeal joints, found between the middle and distal phalanges. These joints primarily facilitate fine digit movements, primarily flexion and extension. Like the MCP joints, each interphalangeal joint is encapsulated by a joint capsule, internally lined with a synovial membrane. Reinforcing these capsules are two collateral ligaments and a palmar ligament. The collateral ligaments originate from the head of the proximal phalanx and extend to the palmar aspect of its distal counterpart. Additionally, each collateral ligament gives rise to an accessory ligament anteriorly, limiting excessive adduction-abduction motions of the interphalangeal joints. The palmar ligament, also known as the palmar or volar plate, presents a robust fibrocartilaginous structure on each interphalangeal joint's palmar surface. Characterized by its inverted "U" shape, this ligament contributes significantly to joint stability and functionality.

1.4.3 The carpometacarpal joints

They are located between the carpal and the metacarpal bones, contributing significantly to the hand's dexterity and functionality. Comprising five distinct CMC joints, the trapeziometacarpal joint of the thumb stands out as the pinnacle of adaptability and precision. In contrast, the remaining four CMC joints operate as synovial joints with functional plane characteristics, connecting the inner four metacarpal bones to the distal row of carpal bones. Surrounded by a robust fibrous capsule, these joints benefit from structural integrity and protection against external stresses. The fibrous capsule's inner lining, composed of a synovial membrane, secretes a lubricating synovial fluid, ensuring smooth and frictionless joint movement. The joint surfaces of the CMC joints are covered by hyaline cartilage. Three distinct sets of ligaments come into play to fortify stability: the dorsal carpometacarpal ligaments, the palmar carpometacarpal ligaments, and the interosseous ligaments. The dorsal carpometacarpal ligaments, situated dorsally, provide robust reinforcement to the CMC joints. Consisting of seven ligamentous bands extending obliquely between the dorsal surfaces of the distal carpal bones and the medial metacarpal bases, these ligaments offer substantial support. However, the fifth metacarpal deviates from this pattern, receiving only a single ligamentous band from the hamate bone. Similarly, the palmar carpometacarpal ligaments, positioned on the palm side, mirror their dorsal counterparts in structure and function. They contribute to joint stability by linking the palmar surfaces of the distal carpal bones with the medial metacarpal bases. Lastly, the interosseous ligaments, though diminutive, play a pivotal role in stabilizing the CMC joints. Comprising two robust fibrous bands, these ligaments extend between the lower aspect of the distal margins of the capitate and hamate bones and the bases of the third and fourth metacarpals, providing additional reinforcement and structural integrity to the joint complex.

1.4.4 Wrist anatomy and movements

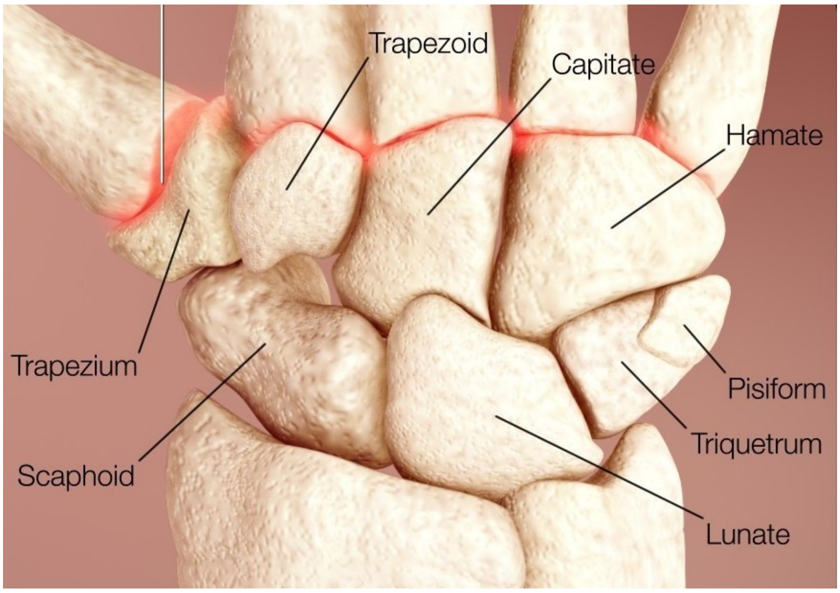

Figure 1.7: Proximal and distal rows of the bones in the wrist [11].

There are eight carpal bones as depicted in Figure 1.7 , and they are irregularly shaped; these bones connect the long bones of the forearm with the metacarpal bones of the hand. They are organized in two rows: the proximal row and the distal row. The scaphoid, lunate, triquetrum, and pisiform bones are in the proximal row. The bones in the distal row are trapezium, trapezoid, capitate and hamate. Every carpal bone is multifaceted, meaning that it articulates with several surrounding bones, and this gives flexibility.

Proximal row

- The largest bone is the scaphoid; it articulates with the trapezium, trapezoid, lunate, and capitate bones.
- The lunate, triquetrum, and pisiform are bones of the proximal row of the carpus, each with distinct features and articulations. The lunate, located between the scaphoid and triquetrum, articulates proximally with the radius and the articular disc of the distal radioulnar joint and distally with the

capitate. The triquetrum, a pyramid-shaped bone, is positioned medially in the carpus, articulating laterally with the lunate and distally with the hamate. The pisiform, a small sesamoid bone embedded in the tendon of the flexor carpi ulnaris, articulates with the triquetrum and is easily palpable due to its superficial location in the palm.

- The lunate bone is a central structure in the proximal row of the carpus, identifiable by its crescent or moon-shaped appearance, which is the origin of its name. It is strategically situated between the scaphoid and triquetrum bones. The lunate's proximal surface forms an essential part of the wrist joint by articulating with the head of the radius and the articular disc associated with the distal radioulnar joint. This articulation is crucial for the complex movements of the wrist. Distally, the lunate connects with the capitate bone, contributing to the stability and mobility of the carpal structure.

- The triquetrum bone, named for its three-cornered, pyramid-like shape, occupies a medial position in the carpus. This bone articulates laterally with the lunate and distally with the hamate, playing a pivotal role in the structure of the wrist. An exciting feature of the triquetrum is its isolated oval-shaped facet on the distal palmar surface. It is an articulation point with the pisiform bone, a unique sesamoid wrist bone.

- The pisiform bone is a small, pea-shaped structure that is distinct within the carpus due to its sesamoid nature, being entirely embedded within the tendon of the flexor carpi ulnaris muscle. This bone's primary function is to act as a fulcrum for tendon movement, enhancing the mechanical advantage of the flexor carpi ulnaris. The pisiform's dorsal surface articulates with the triquetrum, and due to its superficial position on the palmar surface, it is easily palpable, making it an accessible landmark in clinical examinations of the wrist.

Distal row

- The trapezium, trapezoid, capitate, and hamate bones are critical components of the distal row of carpal bones, each with unique anatomical features and articulations. The trapezium, positioned laterally, articulates with the scaphoid, trapezoid, and first and second metacarpals. The trapezoid, wedge-shaped and smaller from a palmar view, connects with the scaphoid, trapezium, capitate, and the second metacarpal. The capitate, the largest carpal bone, primarily articulates with the third metacarpal and surrounding carpal bones. The hamate, the most medial bone of the distal row, features the hamulus, which plays a critical role in the structure of the carpal tunnel and Guyon's canal.

- The trapezium bone is the most lateral in the distal row of the carpus and is crucial for wrist and thumb movements. Also known as the more significant multangular bone, it articulates with the scaphoid proximally, the trapezoid medially, and the first and second metacarpals distally. Its palmar surface features a tubercle and groove, which are essential for tendon and ligament attachments and aid in the functional anatomy of the hand. The dorsal surface is closely related to the radial artery, highlighting its importance in skeletal and vascular anatomy.

- The trapezoid bone, though small, plays a vital role in the distal carpal row. This wedge-shaped bone is situated medially to the trapezium. It appears small from a palmar view but is broader dorsally. The trapezoid articulates with the scaphoid proximally, the trapezium laterally, the capitate medially, and the second metacarpal distally, making it essential for wrist stability and the connection between the carpal bones and the metacarpals.

- The capitate bone is the most prominent carpal bone centrally located in the distal row. It primarily articulates distally with the third metacarpal, which is crucial for wrist movement. The capitate also connects with the trapezoid laterally, the scaphoid and lunate proximally, and the hamate medially, serving as a central axis for the carpal structure and supporting hand function.

- The hamate is the most medial bone in the distal carpal row, distinguished by its wedge shape and the prominent hamulus, a hook-like projection on its palmar surface. It articulates distally with the fourth and fifth metacarpals, laterally with the capitate, and proximally with the triquetrum. The hamulus is significant for forming the medial wall of the carpal tunnel and the lateral wall of Guyon's canal, as well as serving as an attachment point for essential muscles and ligaments, including the flexor retinaculum, making the hamate key to both the mechanical and neurovascular functions of the wrist.

Mechanical movement of the wrist

The wrist joint, while anatomically complex, can also be understood from a mechanical perspective, particularly in terms of the forces, torques, and movement patterns it generates during functional tasks. The wrist operates as a biaxial joint, allowing motion in two primary planes: the sagittal plane for flexion and extension, and the frontal plane for radial and ulnar deviation. These movements are critical for both precision tasks and load-bearing activities [1], as they contribute to the wrist's ability to adapt to varying functional demands.

Wrist flexion and extension are fundamentally hinge-like movements, where the hand moves about a horizontal axis through the radiocarpal joint. From a

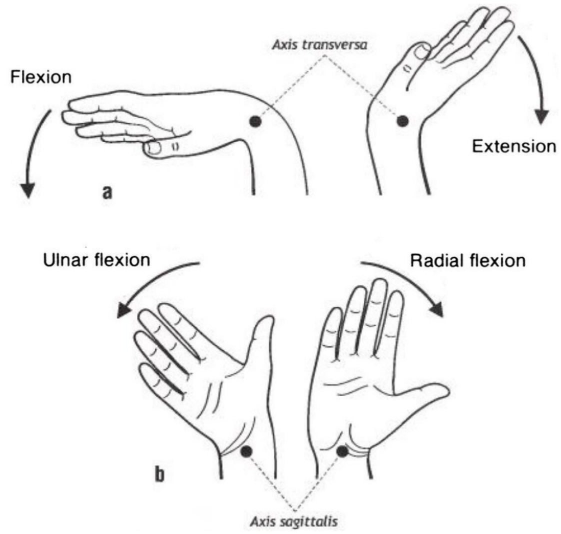

Figure 1.8: .
Schematic representation of wrist movements. The top portion (a) illustrates wrist flexion (downward movement towards the forearm) and extension (upward movement away from the forearm) around the transverse axis. The bottom portion (b) depicts ulnar flexion (movement towards the ulna) and radial flexion (movement towards the radius) around the sagittal axis [12].

mechanical standpoint, flexion is characterized by a positive torque generated by the wrist flexor muscles, which overcome external resistance to rotate the hand toward the forearm. Flexion typically allows for a range of motion up to 90° [2], depending on factors such as ligament tension and joint congruence. In tasks requiring a strong grip, wrist flexion is limited due to the necessity of stabilizing the hand in a more extended position, optimizing force transmission through the forearm and hand.

In contrast, wrist extension involves a negative torque applied by the extensor muscles. Extension generates mechanical stability in tasks like pushing or supporting loads, as the wrist locks into a more rigid configuration at the extremes of motion, typically up to 70° [2]. Extension is biomechanically favorable for tasks requiring strength and stabilization because the mechanical advantage of the extensor muscles improves the hand's ability to resist external forces.

Radial and ulnar deviation represent lateral wrist movements along the frontal plane. Mechanically, radial deviation moves the hand toward the thumb side, involving a torque generated by the radial deviator muscles. This movement is typically more limited in range, around 20° [2], due to the bony structures of the radial styloid process, which acts as a constraint. Radial deviation is advantageous in fine motor tasks where precise lateral positioning of the hand is required, such as turning a key or manipulating small objects. The limited range of motion in radial deviation, however, means that large force generation is less efficient compared to other wrist movements.

Conversely, ulnar deviation allows for a greater range of motion, typically around 30° [2]. This movement enables medial hand positioning, useful in tasks that require gripping or lifting heavy objects. Ulnar deviation involves significant torque, as the ulnar deviator muscles work against the resistance of both the load and the passive tension in the radial ligaments. The mechanical advantage in ulnar deviation arises from the broader range of motion and the capacity to generate larger forces, making it integral to load-bearing and grip-intensive activities.

From a mechanical efficiency standpoint, wrist movements rely on the interplay between active muscular forces and passive elements such as ligamentous tension and joint surfaces. The wrist's ability to distribute forces across its articulations minimizes stress concentrations, particularly in repetitive or high-load tasks. The combination of flexion / extension and radial / ulnar deviation allows a high degree of adaptability, allowing the hand to maintain stable contact with objects, adjust its orientation, and modulate grip force according to task demands.

1.5 Surface electromyography signal

Surface electromyography is a non-invasive method employed to measure and quantify the electrical activity generated by skeletal muscles during voluntary contractions [13]. It can be measured by placing electrodes on the skin surface directly above the muscles of interest; sEMG captures the summation of action potentials emitted by motor units within the muscle. These action potentials generate a voltage signal that is detected by the electrodes. The resulting sEMG signal is a complex waveform that reflects muscle activation's temporal and spatial characteristics, including the recruitment of motor units, the synchronization, and the firing rate. Depending on various factors, the sEMG signal's amplitude typically ranges from a few microvolts (µV) to several millivolts (mV). These factors include the size and type of the muscle, the level of muscle contraction, the distance between the electrodes and the active muscle fibers, and the thickness of the subcutaneous tissue. The quality of the sEMG signal is influenced by the type of electrodes used, the electrode placement, and the skin preparation to minimize impedance [14]. Proper skin preparation, which involves cleansing the skin to remove oils and dead skin cells, is crucial for reducing impedance and enhancing the accuracy of the recordings.

sEMG is widely applied across various disciplines, including clinical diagnostics,

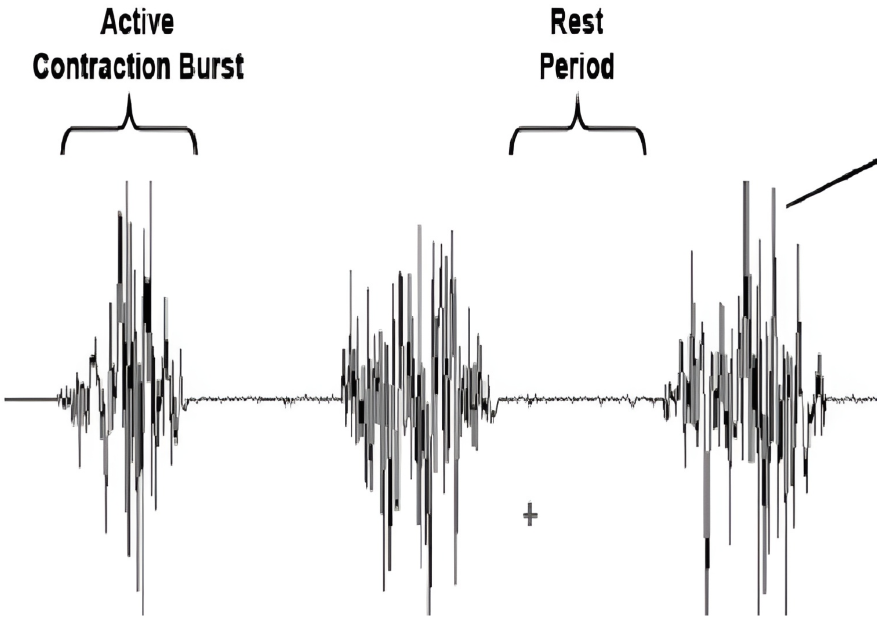

Figure 1.9: Representation of an sEMG signal with resting period and burst activations [15].

rehabilitation, ergonomics, biomechanics, and sports science [13]. In clinical settings, sEMG assesses neuromuscular disorders, monitors muscle activity during rehabilitation, and guides physical therapy and surgery interventions. It is particularly valuable for diagnosing conditions like muscle dystrophy, nerve injuries, and motor control abnormalities. In rehabilitation, sEMG can track progress, optimize therapeutic exercises, and provide biofeedback to patients, helping them improve muscle coordination and strength. In ergonomics and occupational health, sEMG is utilized to evaluate muscle load and fatigue in workers, aiming to prevent musculoskeletal disorders by designing ergonomic interventions. For instance, sEMG can assess the risk of repetitive strain injuries by monitoring muscle activity during tasks that involve prolonged or repetitive movements. In sports science, sEMG is critical in analyzing athletic performance, optimizing training regimens, and preventing injuries. It helps understand the muscle activation patterns during different sports activities, allowing coaches and athletes to tailor their training programs for maximum efficiency and safety.

The analysis of sEMG signals can be performed in both the time and frequency domains, offering a variety of metrics for interpreting muscle function. Time-domain analysis involves parameters such as the root mean square (RMS) amplitude, which measures the signal's power and is correlated with the force produced by the muscle. Other time-domain metrics include the mean and peak amplitudes, which provide insights into the intensity of muscle activation, and the onset/offset timing, which indicates when a muscle begins and ceases to contract. In this work, several features were extracted in the time domain, including the previously mentioned RMS. Conversely, frequency-domain analysis focused on metrics such as the median and mean power frequency, which provide insights into muscle fatigue and fiber type composition. A detailed description of these features is provided in section 1.8. The sEMG signal is also subject to various sources of noise and artifacts that can complicate its interpretation [14]. External electrical interference from devices such as power lines and electronic equipment can introduce noise into the signal, particularly at frequencies close to 50 Hz or 60 Hz. Motion artifacts, which occur due to the movement of the electrodes relative to the skin, can distort the signal and obscure actual muscle activity. Cross-talk from adjacent muscles is another challenge [13]; it occurs when the signal recorded is not only the target muscle's signal but also has some components from other muscles near the acquisition site, leading to inaccurate assessments.

Skin electrode interface

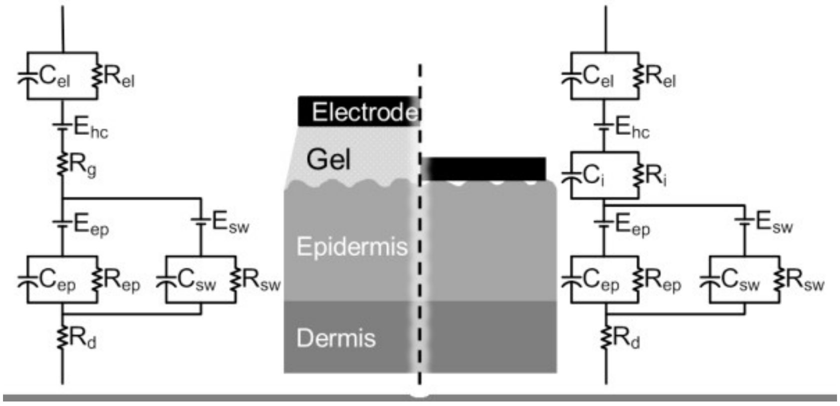

Figure 1.10: Schematic representation of the skin-electrode interface, illustrating the epidermis, dermis and the corresponding electrical model components. On the left gelled electrode, on the right dry electrode. [16].

The skin-electrode interface dramatically influences the quality of the sEMG signal acquisition, as it directly mediates the transmission of electrical potentials generated by muscle activity through the skin to the recording electrodes [17]. The effectiveness of this interface hinges on several factors, including the biophysical properties of the skin, electrode material, preparation techniques, and the precision of electrode placement. The skin presents a variable impedance barrier, as shown in Figure 1.10, influenced by factors such as epidermal thickness, hydration levels, and the presence of hair or sweat, that can introduce noise. To optimize the skin-electrode interface, skin preparation is essential. This procedure typically involves cleaning the skin with alcohol to remove oils and debris [18], followed by light abrasion to reduce the stratum corneum's impedance. These steps minimize the impedance at the interface, thereby enhancing the signal-to-noise ratio (SNR) of the recorded sEMG signals. The material of the electrodes also influences the quality of the recording, with silver/silver chloride (Ag/AgCl) electrodes being preferred due to their superior electrochemical properties and common use. These electrodes facilitate a more consistent and low-noise signal transmission, making them the gold standard in sEMG applications.

The placement of electrodes is another critical factor. An accurate positioning over the muscle belly [19], with alignment parallel to the muscle fibers, ensures maximal signal amplitude, which helps to reduce the cross-talk and enhance the specificity of the recording. The skin-electrode interface is also susceptible to dynamic changes during data recording, such as those caused by movement artifacts and skin deformation. These issues can alter the impedance at the interface, leading to potential signal distortion and artifacts and an electrode detachment, making it impossible to acquire the signal. In order to enhance the quality of the signals it is expected to utilize signal processing techniques, including adaptive filtering, artifact rejection algorithms, and impedance monitoring, are often employed to mitigate these effects and preserve the integrity of the sEMG data.

Influence of noise, movement artifacts and power line noise

Noise and artifacts significantly impact the acquisition quality and therefore the analysis of sEMG signals, often complicating the accurate interpretation of muscle activity [13]. These unwanted influences can arise from various sources and significantly degrade the quality of the recorded data. One of the primary contributors to noise in sEMG is the inherent electrical activity of the skin, known as the baseline noise, which is influenced by the skin's impedance and can fluctuate due to factors like temperature, humidity, and movement. Additionally, muscle cross-talk, where signals from adjacent muscles overlap with the target muscle's activity, can introduce artifacts that obscure the actual signal of interest.

Movement artifacts are another common issue, often resulting from electrode displacement or changes in the skin-electrode interface due to limb movements. These artifacts manifest as low-frequency disturbances that can mask the underlying sEMG signal. Proper electrode placement and secure attachment are essential to minimize these artifacts, although they cannot be eliminated, especially during dynamic activities.

Power line interference, typically at 50 Hz or 60 Hz [13], is a prevalent external noise source in sEMG recordings. This interference can be introduced into the sEMG signal through the environment, mainly when, during the acquisition, there is a significant presence of electrical devices or poor grounding. Differential amplification is often used to mitigate this, which amplifies the difference between two electrode signals while rejecting common-mode noise, including power line interference. Another method usually employed to eliminate the power line noise is the notch filters. They are specifically designed to target the power line frequency to reduce this interference's impact [20].

Managing noise and artifacts in sEMG acquisition is crucial for obtaining reliable and accurate data. Achieving this requires a combination of proper electrode setup, careful experimental design, and the application of advanced signal-processing techniques.

1.6 Motor Unit Action Potential (MUAP)

The Motor Unit Action Potential (MUAP) is a key electrical signal that underpins the function of muscles, reflecting the activity of motor units (MUs). Each motor unit is composed of a motor neuron and all the muscle fibers it innervates, forming the smallest functional unit of muscle contraction. When an action potential travels down the axon of a motor neuron, it reaches the NeuroMuscular Junction (NMJ), where acetylcholine is released, triggering an action potential in the muscle fibers associated with that motor unit. This muscle fiber action potential propagates along the fibers, and the sum of these propagating potentials forms the MUAP, which can be detected as a voltage distribution on the skin using surface electromyography. The sEMG signal represents the cumulative activity of multiple MUs, with each

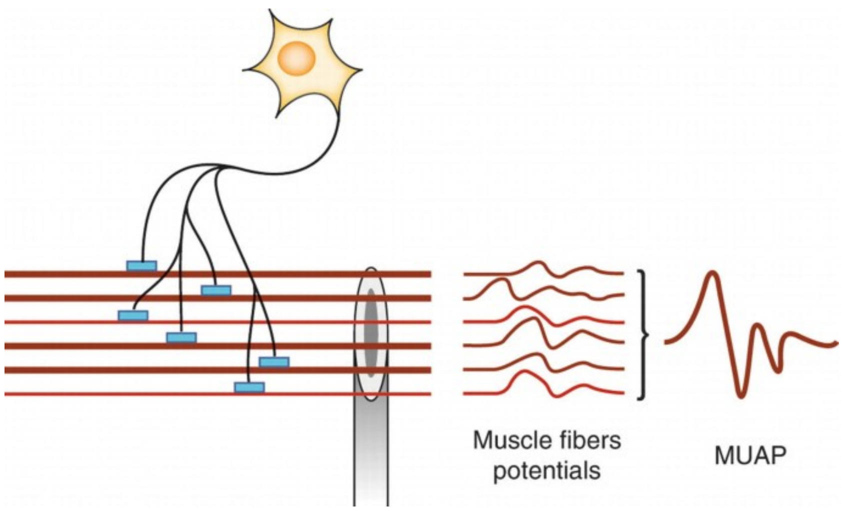

Figure 1.11: Schematic representation of a MUAP generation [21]

MUAP contributing to the overall signal. The MUAPs propagate bidirectionally from the motor unit's innervation zone toward the muscle-tendon junctions, and their characteristics are shaped by factors such as the size and histological type of the muscle fibers within each motor unit. These factors ensure that the action potentials from the fibers of a single motor unit travel at roughly the same conduction velocity (CV), allowing their contributions to sum coherently on the skin's surface. As a result, each MUAP provides a distinctive characteristic for its respective motor unit, which can be captured by electrodes placed parallel to the muscle fibers.

The recruitment of motor units and their firing rates are controlled by the central nervous system and are directly related to the force produced by the muscle. As muscle contractions intensify, more motor units are recruited, and the discharge rate of each motor unit increases. This modulation is reflected in the sEMG signal, with higher force levels producing more complex patterns due to the increased number of contributing MUAPs. However, with progressively stronger voluntary contractions, distinguishing individual MUAPs becomes more challenging, as the interference pattern generated by the overlapping action potentials from many active MUs increases.

The propagation velocity of MUAPs depends on the ionic dynamics of the muscle fiber membranes, with action potentials traveling from the NMJ to the muscle-tendon junction at a speed that varies according to the fiber type and condition. This velocity is a critical parameter in understanding muscle function, as it influences both the timing and the amplitude of the MUAPs detected on the skin. The depth and orientation of the muscle fibers also affect the strength of the detected MUAPs, with superficial fibers contributing more significantly to the sEMG signal compared to deeper fibers.

One of the fundamental distinctions between sEMG and other bio-electric signals, such as those from electrocardiography (ECG) or electroencephalography (EEG), lies in the spatial arrangement and directionality of the detected signals. In sEMG, the electrodes capture the bidirectional propagation of MUAPs along the muscle fibers, a phenomenon not observed in ECG or EEG. This unique characteristic allows sEMG to provide detailed information about muscle activity, including insights into motor unit recruitment strategies and neuromuscular control mechanisms.

The ability to interpret sEMG signals in terms of MUAP dynamics is essential for a wide range of applications [13], from clinical diagnostics to motor control research. By analyzing the summation of individual MUAPs, researchers and clinicians can gain valuable information about muscle performance, neuromuscular health, and motor function. Moreover, understanding the factors that influence MUAP propagation such as muscle fiber type, motor unit recruitment, and action potential conduction velocity can help in the development of more accurate models of muscle activity and in designing more effective interventions for rehabilitation and motor control training.

As muscles contract voluntarily or involuntarily, the MUAPs detected via sEMG provide a window into the underlying neuromuscular processes. The sum of these action potentials reflects the combined activity of the recruited motor units and offers a means to quantify muscle force output, track fatigue, and assess neuromuscular coordination. With its ability to non-invasively capture real-time information about muscle activation patterns, sEMG has become a critical tool in the study of human movement, biofeedback, and rehabilitation.

1.7 Single differential acquisition

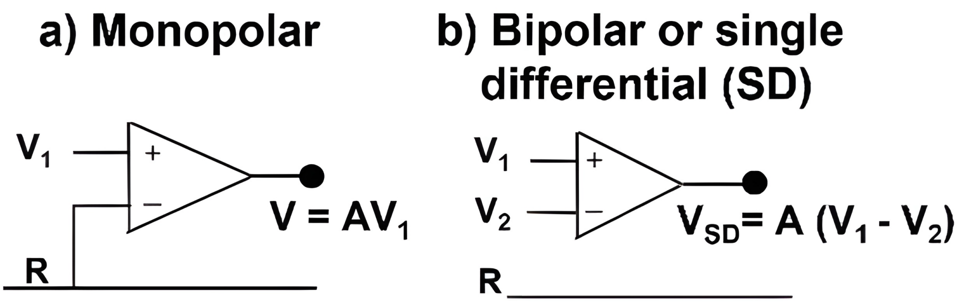

Figure 1.12: Single differential acquisition schematic representation [13].

The single differential configuration is a technique in the acquisition of sEMG signals aimed at improving signal quality by reducing noise and, therefore, enhancing the accuracy of muscle activity detection [13]. It involves using two electrodes placed on the skin over the target muscle. The potential difference between the signals detected by the two electrodes is computed in the differential acquisition. This differential measurement effectively cancels out common-mode signals, such as external electrical noise or signals from distant sources, that are present equally on both electrodes. The result is a signal that more accurately reflects the true activity of the target muscle, with significantly reduced interference from external noise sources, improving the SNR.

One of the advantages of the single differential configuration is its heightened sensitivity to localized muscle activity[13]. Because the output signal represents the difference in electrical potential between two closely spaced points on the muscle, it is more responsive to small changes in muscle activity between these points. In these cases, the single differential method is beneficial for applications requiring precise muscle dynamics monitoring, which is particularly important in this thesis work. The signal obtained from this configuration is typically bipolar and exhibits positive and negative values. This bipolar nature arises from how the muscle's electrical potentials vary spatially across the two electrodes.

However, there are some challenges associated with the single-difference approach. The signal amplitude is generally lower than the one obtained from monopolar configurations, where a single electrode's potential is referenced against a distant, relatively inactive electrode. The accuracy of the single differential signal is highly dependent on the precise placement of the electrodes. Incorrect placement can lead to contamination from signals by cross-talk.

The single differential configuration is often used in the literature as a method for sEMG recording due to its ability to isolate and accurately measure specific muscle activities while minimizing the impact of external noise.

1.8 sEMG features overview

Features in the time domain

Mean Absolute Value (MAV)

$$\mathrm{MAV} = \frac{1}{N}\sum_{i=1}^{N}|x(i)| \tag{1.1}$$

The mean absolute value, represents the average of the absolute values of the signal. It is calculated as the arithmetic mean of the absolute signal amplitudes over a given time window. The MAV serves as an indicator of the overall intensity of the signal, facilitating the distinction between periods of muscular contraction and rest. Its simplicity and effectiveness make it a widely used metric in sEMG analysis.

Root Mean Square (RMS)

$$\mathrm{RMS} = \sqrt{\frac{1}{N}\sum_{i=1}^{N}x(i)^2} \tag{1.2}$$

The root mean square, which is computed as the square root of the mean of the amplitudes of the squared signal. RMS provides a robust estimation of the muscle force, as it is directly proportional to the recruitment of motor units. This feature is particularly valuable in quantifying the strength of muscle contractions while being less sensitive to transient variations in signal amplitude.

Zero Crossing (ZC)

$$\mathrm{ZC} = \sum_{i=1}^{N-1} \mathrm{sgn}\Big(x(i) \cdot x(i+1) < 0 \land |x(i) - x(i+1)| > \Delta\Big) \tag{1.3}$$

The zero crossing metric quantifies the number of times the signal amplitude crosses zero within a specified time window. To ensure robustness, ZC incorporates a threshold (Δ) that excludes crossings caused by noise or minimal amplitude fluctuations. This feature highlights the frequency content of the signal and is particularly useful for detecting rapid transitions in muscle activation patterns

Slope Sign Changes (SSC)

$$\mathrm{SSC} = \sum_{i=2}^{N-1} \mathrm{sgn}\Big((x(i) - x(i-1))(x(i) - x(i+1)) > 0 \land |x(i) - x(i+1)| > \Delta\Big) \tag{1.4}$$

The slope sign changes evaluates the number of times the slope of the signal changes direction. This features identifies points of inflection in the signal while incorporating a threshold (Δ) to eliminate minor variations. This feature is indicative of dynamic changes in the signal, making it suitable for detecting rapid muscle contractions and transitions.

Simple Square Integral (SSI)

$$\mathrm{SSI} = \sum_{i=1}^{N} x(i)^2 \tag{1.5}$$

The simple square integral measures the energy of the signal over time by summing the squared amplitudes of all samples within a time window. This metric provides a cumulative measure of the signal's power, reflecting the total intensity of muscle activity during the analyzed period.

Integrated EMG (IEMG)

$$\mathrm{IEMG} = \sum_{i=1}^{N} |x(i)| \tag{1.6}$$

the integrated EMG calculates the sum of the absolute values of the signal amplitudes over a given window. Similar to MAV, the IEMG serves as a cumulative measure of muscle activation, often used to estimate the overall workload experienced by the muscle.

Wave Length (WL)

$$WL = \sum_{i=1}^{N-1} |x(i+1) - x(i)| \tag{1.7}$$

The WL calculates the total variation between consecutive samples of the signal. It is commonly used to assess the frequency content of a signal and the amount of fluctuations within a given window.

Variance (VAR)

$$VAR = \frac{1}{N-1} \sum_{i=1}^{N} (x(i) - \mu)^2 \tag{1.8}$$

The VAR measures the dispersion of the signal values around the mean. It provides insight into the signal's variability and is used to evaluate the consistency of the muscle activation over time.

Willison Amplitude (WAMP)

$$\text{WAMP} = \sum_{i=1}^{N-1} \text{sgn}\Big(|x(i) - x(i+1)| > \Delta\Big) \tag{1.9}$$

The Willison amplitude represents the number of times the difference in amplitudes between consecutive samples exceeds a predefined threshold (Δ). This feature emphasizes rapid changes in signal amplitude, capturing high-frequency components associated with muscle activation bursts or transient movements.

Legend

- $x(i)$: Signal value at the i-th sample
- N: Total number of samples
- Δ: Threshold value
- sgn(condition): Indicator function, equals 1 if the condition is true, otherwise 0

Feature Extraction in Frequency Domain

Mean Frequency (MNF)

The Mean Frequency represents the centroid of the power spectrum and is calculated as:

$$\mathrm{MNF} = \frac{\sum_{i=1}^{N} f(i)P(i)}{\sum_{i=1}^{N} P(i)} \tag{1.10}$$

where $f(i)$ is the frequency at the i-th bin and $P(i)$ is the power spectral density at the same bin.

Median Frequency (MDF)

The Median Frequency divides the power spectrum into two equal halves, such that:

$$\int_0^{f_{\mathrm{MDF}}} P(f)\,df = \frac{1}{2}\int_0^{f_{\max}} P(f)\,df \tag{1.11}$$

where f_{MDF} is the median frequency and $P(f)$ is the power spectral density.

Total Power (Ptot)

The Total Power represents the total energy of the signal in the frequency domain and is computed as:

$$\mathrm{Ptot} = \sum_{i=1}^{N} P(i) \tag{1.12}$$

where $P(i)$ is the power spectral density at the i-th bin.

Legend

- $f(i)$: Frequency at the i-th bin
- $P(i)$: Power spectral density at the i-th bin
- $f_{\max}$: Maximum frequency in the signal
- f_{MDF}: Median frequency
- Δ: Threshold value (not used in these features but included for consistency)
- N: Total number of frequency bins

1.9 Skeletal muscles

1.9.1 Muscle structure and sarcomere organization

Skeletal muscles differ significantly in size, shape, and fiber arrangement as represented in Figure 1.13. They are richly supplied with blood vessels and nerves directly connected to their primary function: contraction. Skeletal muscle is a dynamic and adaptable tissue capable of responding to stress and generating force. In humans, skeletal muscle accounts for approximately 50% of the total body weight and constitutes around 70% of all body proteins. Muscle mass is regulated by the balance between protein synthesis and degradation, processes that are influenced by various factors such as nutrition, hormonal status, physical activity or exercise, and conditions such as injury or disease. From a mechanical perspective, the primary function of skeletal muscle is to convert chemical energy into mechanical energy, facilitating force production, power generation, postural support, and movement. These functions are essential for performing daily activities, participating in social and occupational settings, promoting health, and maintaining functional independence. From a metabolic point of view, skeletal muscle plays a critical role in the regulation of energy metabolism. It serves as a reservoir for essential substrates such as amino acids and carbohydrates, contributes to thermo-regulation through heat production, and consumes most of oxygen and fuel during physical activity and exercise.

Skeletal muscle is a tissue of myofibers, each containing hundreds to thousands of myofibrils [23] [24]. These myofibers are grouped and wrapped in a connective tissue covering. These myofibrils are the contractile elements of the muscle, organized into repeating units called sarcomeres, which are the fundamental units of contraction. Sarcomeres are delineated by Z-discs, protein structures that anchor the thin filaments of actin at each end of the sarcomere. The central region of the sarcomere contains thick filaments of myosin, which overlap with the thin filaments. This arrangement of filaments within the sarcomere creates the striated appearance of the skeletal muscle under a microscope and is crucial for its contractile function. The sarcomere is composed of several regions: the I-band, which contains only thin actin filaments; the A-band, where actin and myosin overlap; the H-zone, containing only thick myosin filaments; and the M-line, which stabilizes the central region of the myosin filaments. These structures work together to ensure coordinated contraction of the muscle.

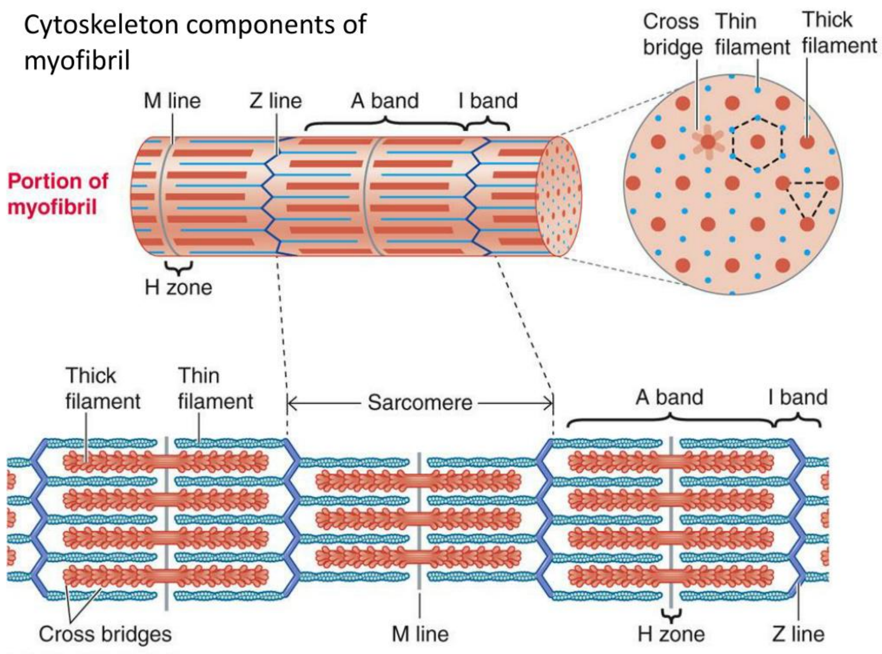

Figure 1.13: Structure of a skeletal muscle sarcomere [22].

1.9.2 The sliding filament theory and calcium ions

The sliding filament theory describes muscle contraction at the molecular level [27], detailing the interaction between actin and myosin filaments within each sarcomere. The Figure 1.13 show how these filaments are partially overlapped in a resting muscle, with tropomyosin blocking myosin-binding sites on actin. Upon stimulation by a nerve impulse, calcium ions (Ca^{2+}) are released from the sarcoplasmic reticulum into the cytoplasm of the muscle fiber. These Ca^{2+} ions bind to troponin C, a subunit of the troponin complex on actin filaments, causing a conformational change that shifts tropomyosin away from the myosin-binding sites. This exposure allows the myosin heads, energized by ATP hydrolysis to bind to actin, forming cross-bridges. The myosin heads then execute a power stroke, pulling the actin filaments toward the center of the sarcomere, resulting in the shortening of the sarcomere. As multiple sarcomeres contract in unison, the entire muscle fiber shortens, generating force and movement.

The regulation of muscle contraction is intricately linked to the concentration of Ca^{2+} in the muscle fiber as it is represented in Figure 1.15. In the absence of Ca^{2+}, tropomyosin remains in a position that blocks myosin-binding sites on actin, preventing cross-bridge formation and thus keeping the muscle in a relaxed state. Upon an action potential, Ca^{2+} is rapidly released from the sarcoplasmic reticulum, binds to troponin C, and induces the necessary conformational change

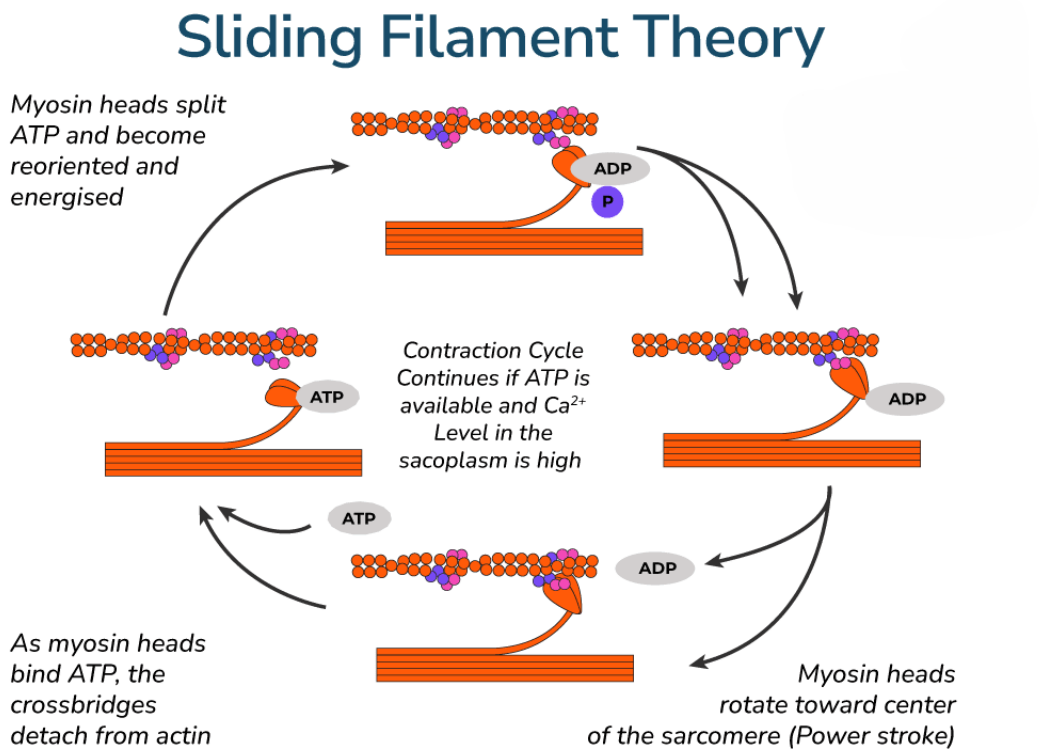

Figure 1.14: The Sliding Filament Theory of muscle contraction. This diagram illustrates how myosin heads bind to actin filaments, undergo a power stroke, and release, driven by the hydrolysis of ATP and the presence of Ca^{2+} ions, leading to the shortening of the sarcomere [25].

in the troponin-tropomyosin complex, enabling myosin heads to attach to actin and initiate contraction. The precise timing and regulation of Ca^{2+} release and re-uptake are critical for proper muscle function. After contraction, Ca^{2+}-ATPase pumps in the sarcoplasmic reticulum actively transport Ca^{2+} back into storage, decreasing cytoplasmic Ca^{2+} concentration and allowing the muscle to relax. Disruptions in this Ca^{2+} cycling can impair muscle function, potentially leading to muscle stiffness or weakness.

Role of the ATP in the cross-bridge formation

ATP plays a central role in muscle contraction by providing the energy necessary for the cross-bridge cycle illustated in Figure 1.16. The cycle begins when ATP binds to the myosin head, causing it to detach from the actin filament. The myosin head then hydrolyzes ATP into ADP and inorganic phosphate (Pi) [29], which

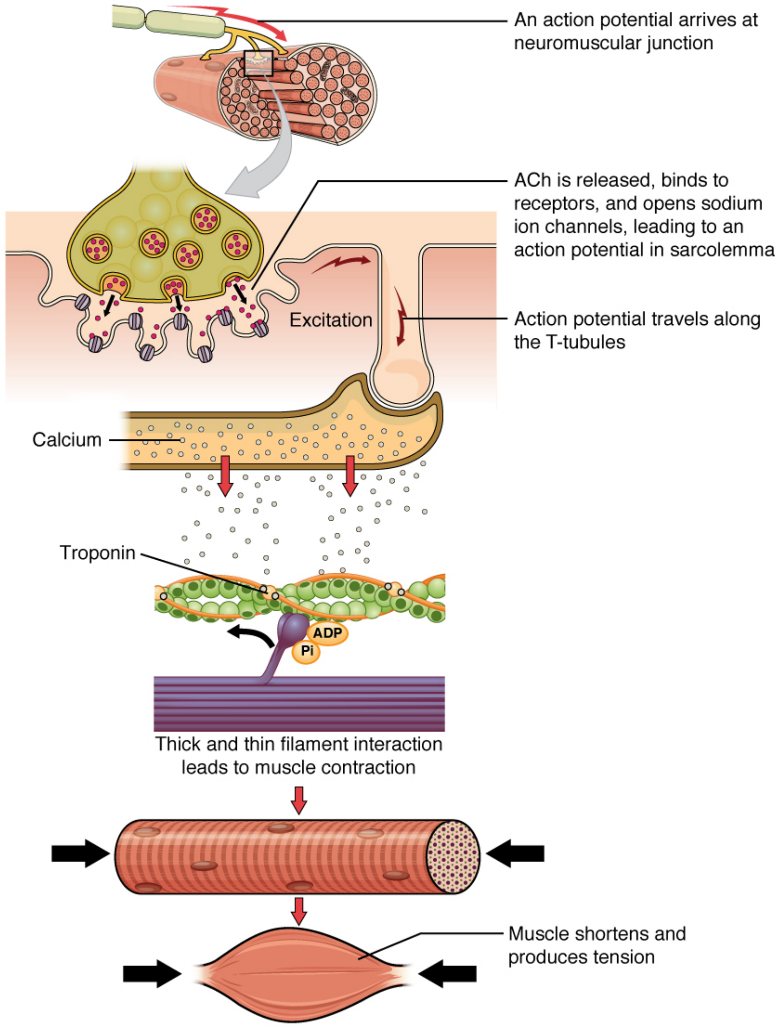

Figure 1.15: Sliding filament theory process illustrating the chemical component[26].

remains attached to the myosin head. This hydrolysis reaction energizes the myosin head, allowing it to return to its high-energy. In this state, the myosin head is ready to bind to a new site on the actin filament.

Pi is released when the myosin head binds to actin, triggering the power stroke. During the power stroke, the myosin head pivots, pulling the actin filament towards the M-line of the sarcomere, resulting in muscle contraction. Following the power stroke, ADP is released, and a new molecule of ATP binds to the myosin head, causing it to detach from actin and allowing the cycle to repeat. This cross-bridge formation and release cycle is repeated many times during a single muscle contraction, and the availability of ATP is crucial for sustaining this process.

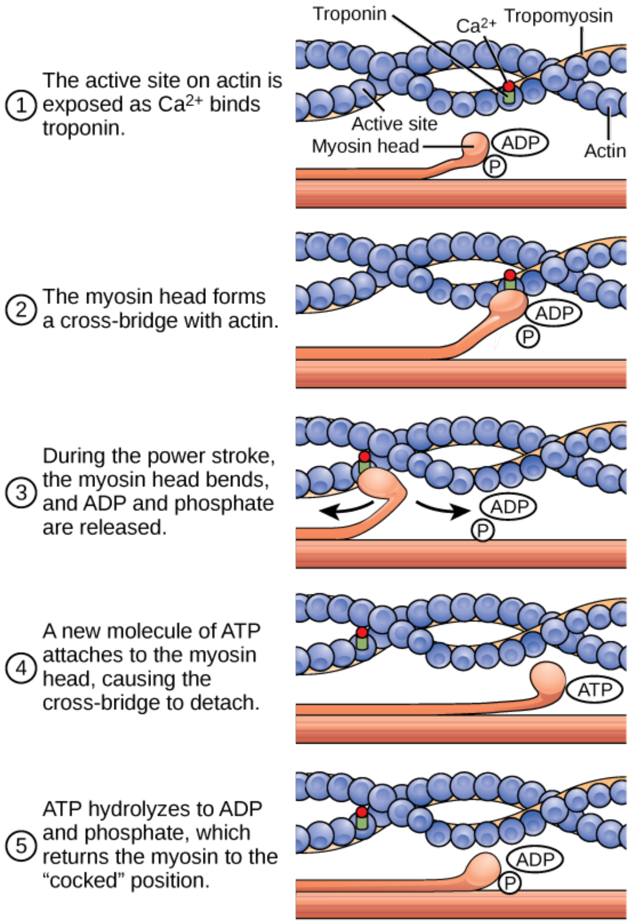

Figure 1.16: Cross bridge cycle representation [28].

Relaxation and replenishment of calcium stores

Muscle relaxation is as carefully regulated as contraction. Once the nerve impulse ceases, Ca^{2+} channels close, and Ca^{2+} is actively pumped back into the sarcoplasmic reticulum by Ca^{2+}-ATPase pumps, a process requiring ATP. As the concentration of Ca^{2+} in the cytoplasm decreases, Ca^{2+} dissociates from troponin, leading to tropomyosin re-blocking of the myosin-binding sites on actin. Without Ca^{2+}, cross-bridge formation is inhibited, and the muscle returns to its resting state. Restoring Ca^{2+} levels in the sarcoplasmic reticulum is essential for muscle readiness and preventing muscle fatigue. During prolonged or intense activity, the muscle's ability to quickly re-sequester Ca^{2+} can be compromised, leading to decreased force production and endurance. The regulation of intracellular Ca^{2+} is a critical factor in muscle physiology, influencing both the strength and duration of contractions.

1.9.3 Regulation of muscle force

The coordinated contraction of sarcomeres within a muscle fiber results in the generation of force and movement. The ability of a muscle to generate varying degrees of force is influenced by several factors, for instance, the frequency of neural stimulation, the number of motor units recruited, and the initial length of the muscle fibers. Muscles can perform both quick, powerful contractions for rapid movements and sustained contractions for posture maintenance, depending on the pattern of neural activation and the metabolic pathways engaged. Efficient ATP utilization and rapid Ca^{2+} cycling are essential for muscle-sustained activity, whether during short bursts of high-intensity activity or prolonged low-intensity exercise.

1.10 Functional Electrical Stimulation (FES)

Functional Electrical Stimulation (FES) is an electric stimulation technique that utilizes electrical currents to activate muscles in order to restore or improve function in individuals with neurological or musculoskeletal impairments [30]. The principle behind FES is to bypass damaged or malfunctioning neural pathways by directly stimulating the target muscles, thereby eliciting controlled contractions or responses.

One of the primary applications of FES is in rehabilitation, where it is used to assist individuals with paralysis or weakness due to conditions such as spinal cord injury, stroke, or multiple sclerosis. By providing electrical stimulation to specific muscles, FES can help restore movement, improve muscle strength, prevent muscle atrophy, and enhance circulation. This can lead to increased independence in activities of daily living and improved quality of life for individuals with mobility impairments. FES is also utilized in various other fields, including sports medicine, where it can be used for muscle conditioning and performance enhancement, and in research settings, where it is employed to study neuromuscular function and motor control. Additionally, FES has shown promise in treating conditions such as urinary incontinence [31], chronic pain, and cardiovascular disorders. It can be utilized in two main ways:

The first application aims to recover muscle mass and volume. In this scenario, the stimulator is used on a patient lying on a treatment table, where electrical stimulation increases muscle mass. This application is typically used for bedridden patients to prevent muscle atrophy or for the rehabilitation of elderly patients with low muscle mass.

The second application uses electrical stimulation to induce muscle contractions in paralyzed or weakened muscles. The primary goal is to assist the patient in performing a function that has been compromised due to trauma or medical conditions. While maintaining muscle volume can be a secondary objective, the primary focus of FES is always to enable the performance of a specific function.

FES is traditionally categorized into three types based on their specific objectives:

FES Neuroprosthesis: This type of FES involves neuroprosthetic devices that allow individuals to perform functions they otherwise could not. Without FES, the person would be unable to carry out that specific action.

FES Training: The goal of FES training is to induce neuromuscular and cardiovascular conditioning through muscle activation and movement. This form of FES aims to improve the general physical condition of the subject. While the devices used may be the same as those for neuroprosthesis, the objective differs. In FES training, the emphasis is on enhancing neuromuscular and cardiovascular conditioning rather than solely performing a specific function.

FES Therapy: This approach focuses on stimulating motor learning to improve the performance of a function that the patient can already perform, albeit with difficulty. For example, if a patient can grasp an object but struggles due to significant muscle weakness or neuromuscular impairment, FES therapy aims to facilitate the grasping action while also promoting neuroplasticity in the central nervous system. The therapeutic goal is to enhance central plasticity by stimulating the muscle and its afferent pathways.

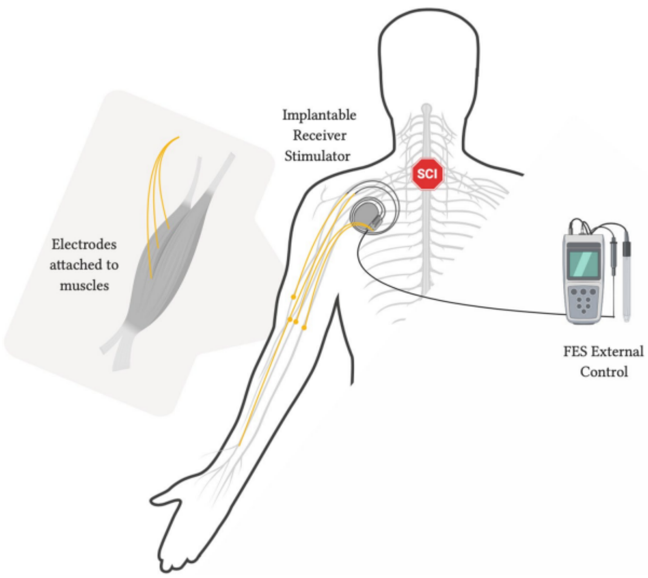

Figure 1.17: Example of a FES stimulation for hand movements [32].

FES stimulation may lead to a tingling sensation on the skin, commonly referred to as a 'pins and needles' feeling [30]. Although this sensation is usually not bothersome for most people, those with multiple sclerosis might be more sensitive to sensory changes and could find it uncomfortable. Typically, a brief session of low-intensity stimulation can help alleviate this discomfort. However, there are times when, despite thorough evaluation, the treatment might not be effective, or individuals may have difficulty using the device properly. Additionally, in some cases, the stimulation or electrodes might cause skin irritation.

The versatility and effectiveness of FES make it an important tool in the realm of rehabilitation and healthcare. Its non-invasive nature, combined with its ability to target specific muscle groups or nerves, offers personalized treatment options for individuals with diverse conditions and needs. Moreover, advancements in FES technology continue to expand its applications and improve its efficacy, paving the way for further advancements in rehabilitative medicine and functional restoration.

1.11 Muscle fatigue in stimulation

Muscle fatigue represents one of the major challenges in the application of Functional Electrical Stimulation (FES). Fatigue can occur at multiple levels of the neuromuscular system, ranging from the motor cortex and spinal levels to the mechanical excitation-contraction coupling in muscle fibers. However, in the context of FES, the focus is primarily on peripheral fatigue, as electrically induced contractions directly stimulate muscles or nerves. Neuromuscular fibers can be broadly classified into two categories: type I fibers, which are fatigue-resistant and recruited first, and type II fibers, which generate greater tension but are more prone to fatigue. Type I fibers are typically involved in endurance activities, such as long-distance running, while type II fibers are essential for high-intensity, short-duration tasks.

During voluntary contractions, the neuromuscular system follows Henneman's size principle, activating type I fibers before recruiting type II fibers as the need for force increases. When fatigue occurs during voluntary contractions, the neuromuscular system implements several strategies to maintain motor performance and force generation. These include increasing the firing rate of motor units, recruiting additional MUs, and occasionally alternating active MUs to allow fatigued ones to recover. These mechanisms allow the system to compensate for reduced muscle fiber capacity and delay the onset of fatigue.

In contrast, none of these compensatory mechanisms are available during electrically stimulated contractions. In FES, the recruitment of motor units is fixed and determined by the stimulation parameters, such as the frequency and amplitude of the electrical stimulus. The spatial distribution of active motor units is also dependent on electrode placement, and no rotation of MUs can occur. Additionally, the order of recruitment does not follow the physiological pattern described by Henneman's principle. Instead, recruitment may be random or reversed, both of which are suboptimal for efficient force generation.

Furthermore, electrically stimulated contractions typically require higher stimulation frequencies than voluntary contractions to achieve sustained force output. Unlike the asynchronous activation of MUs seen in voluntary contractions, FES-induced contractions result in synchronous MU activation. This synchronous pattern produces greater force variability and rhythmic fluctuations, necessitating higher frequencies to maintain a steady force output. As a result, FES-induced contractions often lead to faster fatigue compared to voluntary contractions, emphasizing the need for optimized stimulation strategies to minimize fatigue and prolong functional performance.

1.12 Average Threshold Crossing (ATC) technique

This method generated threshold crossing events from the amplified and filtered sEMG signal to monitor muscle activation, minimizing processing and data transmission loads, optimizing power consumption, and extending operating time [33].

$$\mathrm{ATC} = \frac{\#T_{\mathrm{Cevents}}}{T_{\mathrm{window}}} \tag{1.13}$$

$\#T_{\mathrm{Cevents}}$ represent the number of Threshold Crossing (TC), that is, the number of times the sEMG is above a selected threshold. The ATC value, represented in Figure 1.18, is the number of TC events divided by the length of the observation window (T_{window}). The value of the window in this thesis work is 130ms. Based on the number of ATC values, it is possible to determine different force levels; a higher value of ATC means a higher value of the sEMG signal above the threshold during the window.

The ATC approach significantly reduces data transmission volume, decreasing from approximately 2 kB/s for sEMG to just 8 bytes/s [34]. These properties allow for efficient bandwidth management, making communication more effective. By implementing ATC directly in the hardware, threshold events can be counted without the need for complex analog-to-digital conversions or subsequent computational processing. This reduces the load on the microcontroller's resources and enhances the system's responsiveness. The system is designed for energy efficiency, operating at a voltage of 1.8 V and using Bluetooth Low Energy (BLE) for communication [34]. This combination further reduces power consumption, with ATC optimizations enabling extended operation, reaching up to 230 hours in specific configurations.

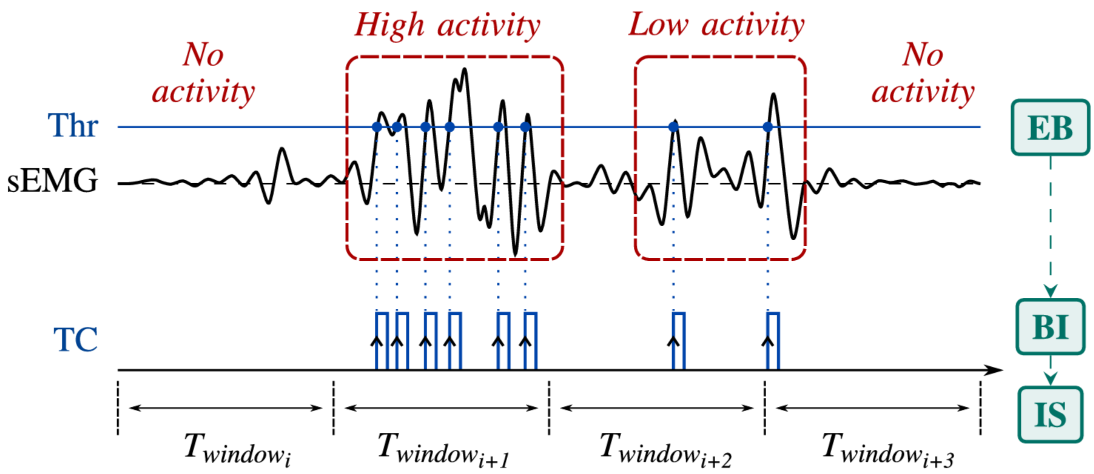

Figure 1.18: ATC calculus framework representing the Event-Based (EB) paradigm. The TC points are identified as the events above the selected threshold represented in the image as a continuous blue line. On the bottom there is the TC signal representation where every TC event is a time-distribution of electrical spikes. In this framework, the Information Synthesis (IS) is carried out by applying the time window T_{window} to the TC distribution. This enables the calculation of the ATC parameter, which encapsulates the state of muscle contraction [34].

The ATC method can also dynamically adapt to variable muscle activity, ensuring effective monitoring even under frequent signal changes.

Threshold calibration

The threshold calibration determines the appropriate voltage value based on the environment and the subject's condition to obtain a TC signal that reflects only muscle activations. This ensures the signal is not affected by physiological fluctuations and adapts to the subject's current state during acquisition [34]. In addition, a hysteresis of 30 mV was applied to minimize the occurrence of false spikes caused by signal fluctuations near the threshold. Ideally, the threshold should be 16 mV above the signal baseline, considering only the lower half of the hysteresis. However, due to noise in real-world situations, the baseline might fluctuate, necessitating threshold calibration when the system powers on.

The calibration process involves a firmware routine that operates as a finite-state machine. The steps of the calibration behavior are represented in Figure 1.19 and described as follows:

- The threshold is decreased by 150 mV every second until an event is detected. When an event occurs, the state advances without altering the threshold.

- Another event is awaited to confirm the detection. If confirmed, the threshold increases by 200 mV and the process moves to the next state; otherwise, it returns to state 1.
- The refinement phase begins by decreasing the threshold by 10 mV each time, following a similar behavior to state 1.
- Each time, a new event is awaited to confirm detection. If positive, the process advances to state 5; if negative, it returns to state 3.
- In the final state, the baseline detection is definitively verified. If no event is detected, the process returns to state 3; if confirmed, the threshold is increased by 40 mV, and the routine concludes.

This process is designed to accurately detect muscle activation, isolating genuine signals from spurious noise spikes.

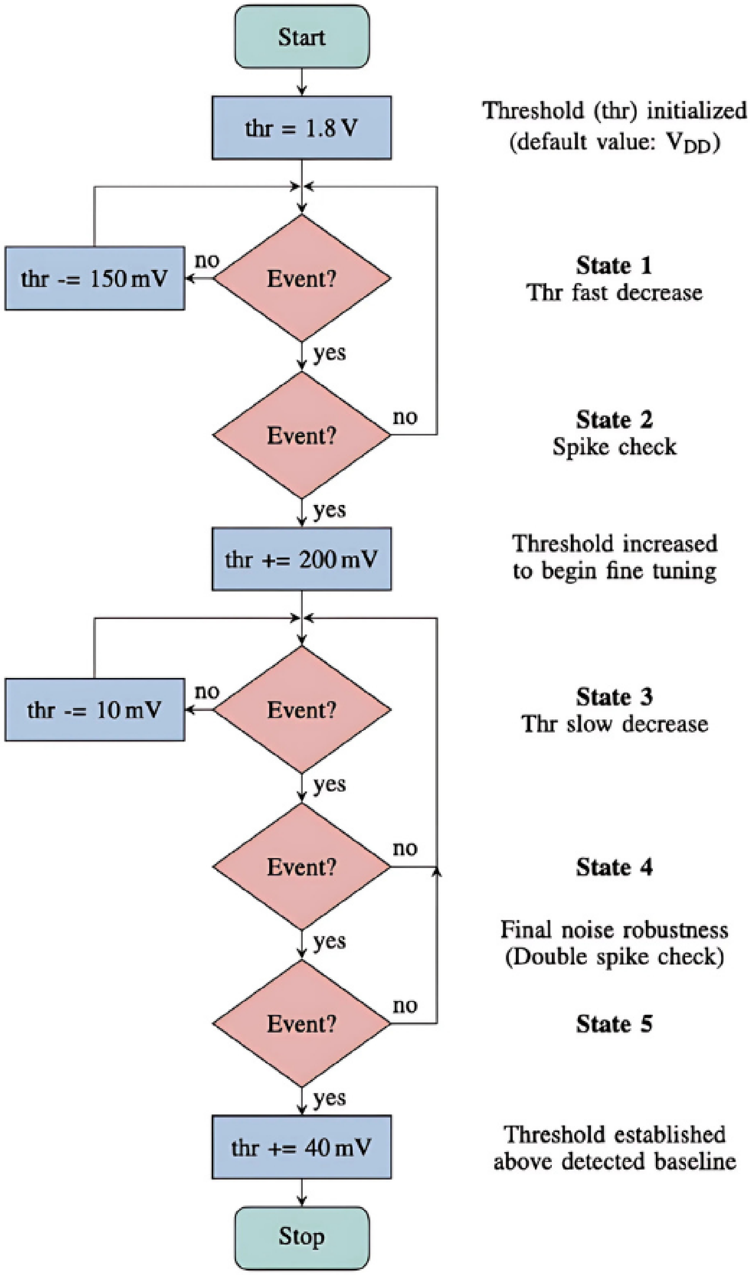

Figure 1.19: Firmware routine for threshold auto calibration. The threshold is initialized to a value much higher than the expected signal baseline, and lowered step by step until one or more events arise. The calibration is divided in a first course phase, together with a check for spurious spikes, and a second fine tuning, which includes a double spike check, to ensure the final result is correct [34].

1.13 Machine learning and deep learning in the clinical field

1.13.1 Machine learning

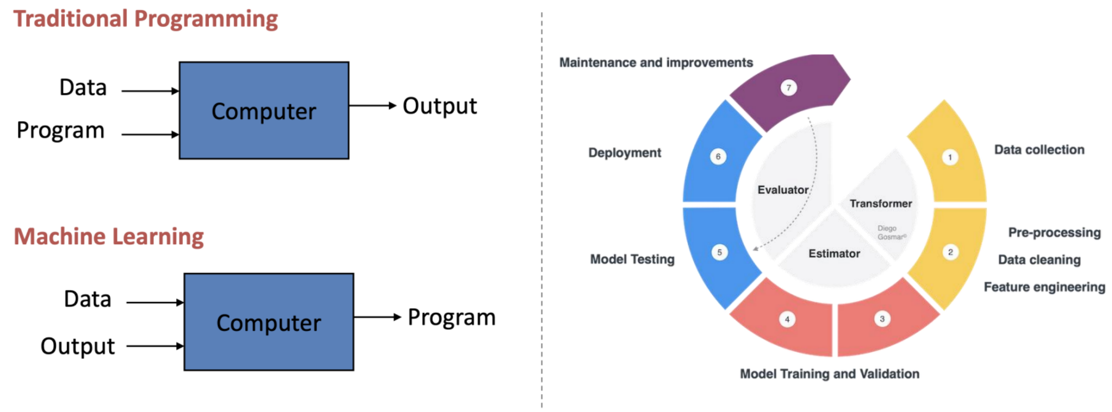

Figure 1.20: Comparison between traditional programming and machine learning workflows. Traditional programming involves feeding data and a program into a computer to produce an output, whereas, in machine learning, data and the desired output are used to train the computer to generate the program. The right side illustrates the machine learning lifecycle, including data collection, pre-processing, model training, testing, deployment, and ongoing maintenance. [35]

In traditional programming, data and the program are provided as inputs to produce a desired output. In contrast, machine learning (ML) reverses this process: we input the data and the desired output, and the computer identifies the underlying patterns or correlations to "learn" the program. ML techniques are thus employed to discover the function that maps the data to the output, effectively extracting knowledge from the data. The process begins with data collection, followed by feature selection and, if necessary, feature normalization. After identifying the relevant features, a model is selected and trained. Subsequently, various metrics are computed to evaluate whether the model has successfully achieved the desired performance in predicting the expected output. This approach requires a substantial amount of data, including clinical data, images, and more, and a critical step is determining which features should be used as inputs for the algorithm. The development of ML is not a linear process. It typically involves several key stages: data collection, preprocessing, model training, and validation, and finally, testing the model on an unseen set of patients. If the model does not achieve the expected performance on the first attempt, the training and validation phase can be revised to adjust and retrain the model. Additionally, it may be necessary to revisit the preprocessing stage, make further adjustments, and re-evaluate the model's performance. This iterative process continues until the desired performance level is achieved. We can identify three main groups of ML algorithms. The first group is **supervised machine learning**, where both input data and the corresponding output are provided. The classification model and regression model are supervised methods. The second is **unsupervised machine learning**, where only the input data is provided without the corresponding output. The k-means and hierarchical clustering are unsupervised methods. The third group is **reinforcement learning**. Additionally, there are semi-supervised approaches, which fall between the first two groups, using a combination of labeled and unlabeled data.

1.13.2 Deep learning

Deep learning (DL) operates differently from traditional machine learning because it combines feature extraction and the learning process into a single phase. This allows DL to work directly with raw data, eliminating the need for preprocessing. Manual feature extraction is necessary when performing a classification task with ML. However, with DL, feature extraction is automated due to the design of the neural network. DL has become popular only in recent years. The primary reason is that DL models are computationally intensive and require Graphics Processing Unit (GPUs), unlike ML models, which can be trained on Central Processing Unit (CPUs). As GPUs became more widespread, DL gained popularity. We can distinguish two main approaches in DL: deep network supervised learning and deep network unsupervised learning. In supervised learning, we work with both data and labels that are the desired output. In contrast, in unsupervised learning, the class or category of the data is unknown.

As illustrated in Figure 1.21, when working with a small amount of data, machine learning tends to deliver better performance. However, as the amount of data increases, deep learning outperforms significantly, providing much higher performance. Deep learning models can handle complex solutions, making them more effective with large datasets.

1.13.3 Artificial Neural Network

Artificial Neural Networks (ANNs) are a machine learning method inspired by the structure and function of the human brain [37]. They are designed to recognize patterns, make predictions, and solve complex problems through a network of interconnected nodes, or "neurons," that process information in layers. Each neuron receives input, processes it using a mathematical function, and then passes the output to other neurons in subsequent layers. The network is organized into

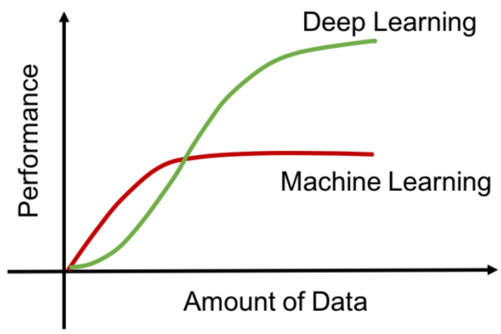

Figure 1.21: Performance comparison between Machine Learning and Deep Learning as a function of data quantity. Deep Learning models typically outperform traditional Machine Learning models as the amount of data increases, illustrating their ability to scale with large datasets [36]

layers: an input layer where features are fed into the network, one or more hidden layers where processing occurs, and an output layer where the final prediction or classification is made as depicted in Figure 1.22. ANNs are particularly effective for tasks involving categorization and time-series analysis.

Unlike traditional statistical methods, such as multiple regression and discriminant analysis, which require specific assumptions about the data (e.g., normally distributed errors or multivariate normality of predictor variables), ANNs do not rely on these assumptions. This flexibility is due to the nonparametric nature of ANNs [37], allowing models to be developed without prior knowledge of the data distribution or potential interactions between variables. ANNs can handle both linear and nonlinear relationships, making them applicable to a broader range of problems than traditional methods constrained by their specific assumptions. Essentially, ANNs provide a more versatile and adaptable solution for various types of problems.

Features selection

Feature selection is a crucial step in the development of predictive models, particularly in machine learning and pattern recognition tasks. It involves the identification and selection of a subset of relevant features from the original set, aiming to retain the most informative variables while discarding redundant or irrelevant ones [39]. This process enhances model performance and efficiency, particularly in machine learning tasks where the number of input features must be manageable. Although there are various feature selection methodologies, no single approach can

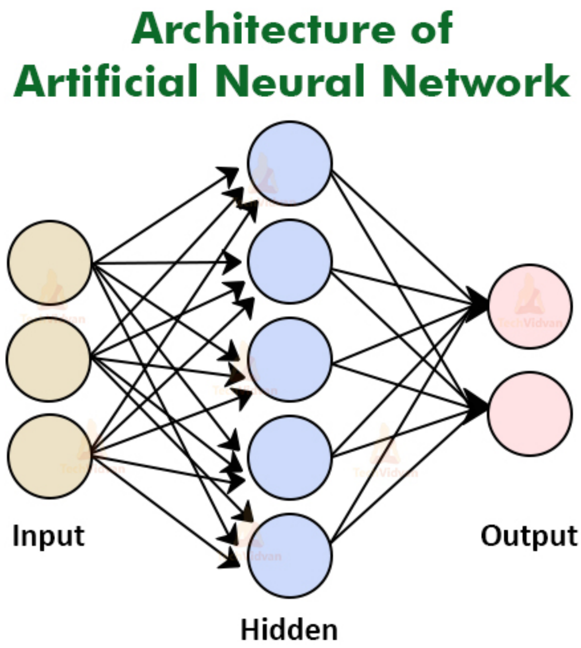

Figure 1.22: Schematic representation of the architecture of an artificial neural network (ANN), illustrating three layers: input layer, hidden layer, and output layer. Each node (neuron) in one layer is connected to all nodes in the subsequent layer, forming a fully connected network [38].

be universally deemed superior to the others [40].

Feature selection techniques can be categorized into four main types: filters, wrappers, embedded methods, and hybrid methods [41].

Filters select individual features or groups of features based on their statistical properties or relevance, without considering the underlying data distribution or the algorithm used. These methods typically rely on measures such as correlation, mutual information, or statistical tests to rank features, ensuring a fast and computationally efficient selection process.

Wrappers evaluate feature subsets based on their performance within a specific model, treating the model as a black box. In classification tasks, wrappers employ classifiers such as Support Vector Machines (SVM) to identify features that maximize model performance [42].

Embedded methods perform feature selection during the model training process, integrating it directly into the algorithm's operation. These methods assess feature relevance throughout the learning process, considering both individual feature importance and interactions with other features within the model [41].

Hybrid methods combine the strengths of filter and wrapper approaches. These methods typically start with a filter to reduce the feature space by eliminating irrelevant or redundant features, often generating multiple candidate subsets [41]. These subsets are then refined using a wrapper method, which evaluates and selects the optimal subset based on model performance, thus achieving a balance between computational efficiency and accuracy.

Principal Component Analysis

Principal Component Analysis (PCA) is a statistical technique used to reduce the dimensionality of large datasets, making them easier to analyze while retaining as much variability as possible. The primary goal of PCA is to transform the original variables into a new set of uncorrelated variables called principal components [43], which are linear combinations of the original features. These components are ordered by the amount of variance they capture from the data, with the first principal component accounting for the largest variance. This transformation simplifies the analysis by reducing the number of variables while maintaining essential information. PCA is widely used in fields such as machine learning, data visualization, and pattern recognition for feature reduction and noise filtering [43]. By focusing on the most significant components, PCA allows for more efficient analysis and interpretation of complex data.

Chapter 2

State Of The Art

2.1 sEMG acquisition device

The sEMG acquisition devices are employed in many applications such as muscle activity monitoring and rehabilitation. Focusing on the latter, the EMG signals can reveal the subjects' health and fitness conditions, which can be achieved with a real-time system. These systems generally acquire and process the signal with the sensor device and transmit it to monitoring equipment. Typically, the main issues in these systems are slow data acquisition and transmission and limited versatility. The latest sEMG acquisition device technologies are primarily wireless, allowing freedom of movement for the patient and preventing potential signal alterations caused by cable connections. These devices rely on a battery to function, but the batteries do not support highly long recordings to monitor the patient throughout the day.

The single-channel sensors are advantageous when targeting a specific portion of the muscle for recording. They are typically used with other single-channel sensors to establish a multi-channel acquisition system [44].

The high-density (HD) sEMG sensors can capture spatial and temporal data from the recording area. These electrode arrays comprise over a dozen electrodes [44]. A notable example of such a device is the Myo armband, which is extensively applied in hand gesture recognition based on sEMG tasks. The medical applications of sEMG devices are diverse.

The Cometa srl [45] has designed sEMG sensors for various purposes. The Pico EMG is a compact sEMG acquisition device that enables selective recording targeting a specific muscle or muscle region. This device is compatible with both gelled electrodes and plated-gold electrodes. The Mini Wave Infinity retains the same features as the Pico sEMG while offering cables to modify the inter-electrode distance. The Mini Wave Waterproof is designed for data acquisition in aquatic environments, and they have been utilized in research related to swimming.

(a) Pico EMG device. **(b)** Mini Wave EMG device. **(c)** Mini Wave Waterproof device.

Figure 2.1: Acquisition sEMG devices developed by Cometa srl.

Another commercial sEMG device is the DataLITE sEMG sensor [46] developed by Biometrics Ltd company. As with Cometa's devices there are two variants: one featuring a fixed inter-electrode distance and the other incorporating cables that enable the user to adjust the inter-electrode spacing; both devices operate wirelessly with a transmission range of up to 30m from their interface. With an input impedance exceeding 100 MΩ these sensors do not necessitate skin preparation and offer a battery lifespan of 8 hours. All components are enclosed within a compact casing measuring 42x24x14 mm and weighing 17 g.

(a) DataLITE device with cables. **(b)** DataLITE device with electrodes on the bottom.

Figure 2.2: Acquisition sEMG devices developed by Biometrics Ltd company.

2.2 ATC technique

Crepaldi et al. [47] introduced the use of ATC as a feature strongly correlated with contraction force as illustrated in Figure 2.3. To validate the ATC method, Crepaldi et al. compared the number of TC events generated within a specific time window to the force level. The results reported a correlation of 0.95 ± 2, demonstrating that ATC can be reliably used as a parameter for muscle force assessment. Rossi et al. utilized the ATC technique to control an FES system. The

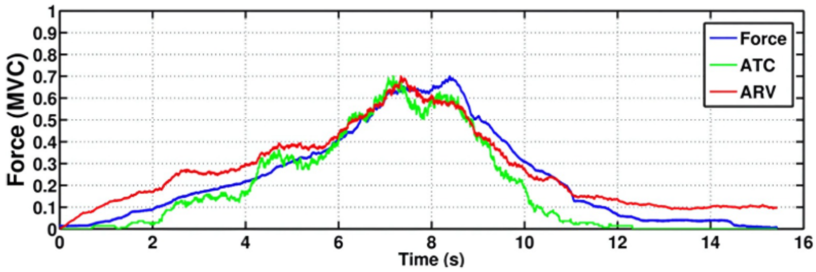

Figure 2.3: Plot of ATC, Absolute Rectified Values (ARV), and applied force during a grip movement [47].

hardware system comprised four analog front-end channels and a microcontroller unit. Additionally, the system featured a Bluetooth communication module to transmit data to the control workstation.

The power consumption of the acquisition board, which included the four analog front-end channels and the microcontroller unit, amounted to 5.125,6 mW in low-power mode. Considering wireless transmission, the consumption increased to 20.23 mW for TC transmission and 23.47 mW for sEMG transmission.

An ATC-controlled FES system was developed with two operating modalities. The first is *self-administered stimulation*, while the second is *two-subject stimulation*, where two individuals are involved; in a medical context, this typically refers to the therapist and the patient.

The system consists of three main components:

- The acquisition unit, which extracts features to generate the ATC signal.
- The actuation unit, which serves as the FES stimulator.
- The control unit, which manages and integrates the other two components while running the graphical user interface.

The experimental results were evaluated using the median value of the correlation coefficient between the voluntary movement and the stimulated one. This value was found to be above 0.9 across four different movements.

In another study Rossi et al. [48], the previously described system was implemented as an embedded solution using a Raspberry Pi. The system was developed in Python, adopting an object-oriented and multi-threaded approach.

The experimental results, evaluated on five healthy subjects specifically three males and two females, reported a correlation coefficient of 0.86 ± 0.07.

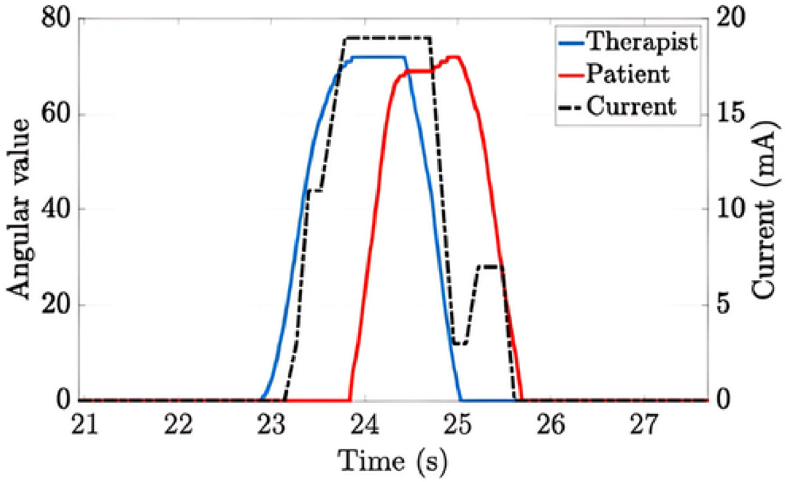

Figure 2.4: Similarity analysis of the cross-correlation coefficient between the limb motion angular signals of the therapist and the subject [48].

Mongardi et al. [49] developed a low-power bio-inspired armband designed for hand gesture recognition. The armband, illustrated in Figure 2.6 consisted of seven channels and could be applied in various fields, such as serious gaming control, rehabilitation, and sign language recognition.

This system generated the ATC signal using a 130 ms window. By exploiting the event-based nature of the ATC, the armband achieved onboard prediction with low power consumption.

The experimental results, obtained from 26 subjects performing 8 different hand gestures illustrated in Figure 2.5, reported an average accuracy of 91.9%.

Prestia et al. [50] evaluated an event-driven approach for FES control based on the ATC technique. The system extracts ATC events from sEMG signals and modulates the stimulation intensity accordingly, eliminating the need for complex feature extraction. The proposed system was developed for a two-subject stimulation framework, where the therapist performs a movement, and the patient is stimulated accordingly to replicate the same movement.

Experimental validation on 17 healthy subjects performing six different movements demonstrated a high replication accuracy of therapist-induced movements. The system achieved a median cross-correlation coefficient of 0.910 and a median

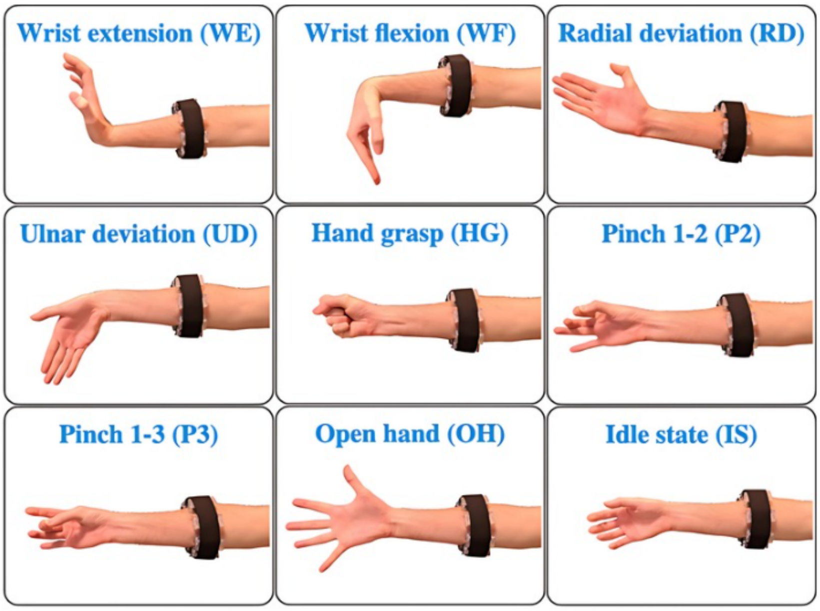

Figure 2.5: Movements performed in the study [49], wrist extension, wrist flexion, radial deviation, ulnar deviation, hand grasp, pinch using thumb and index finger, pinch using thumb and middle finger, hand open, resting state.

response delay of 800 ms, with a movement replication success rate of 97.39%.

2.3 State of the art in hand gesture recognition

The pattern recognition can be performed both with machine learning (ML) and deep learning (DL) algorithm [51]. The ML algorithms usually need processed data because they struggles with inconsistent or noisy data. They can also manage a limited number of data compared to the DL algorithms. The DL is characterized by its hierarchical model architecture, which automatically learns features from data. Usually the DL algorithms have several layers and the features are extract at different depth. For a task of complex hand gesture recognition the use of DL is more indicated [52]. Parajuli et al. [53] found that most data used in ML algorithms are steady-state signals. However, in real-world scenarios, signals are often non-stationary. Analyzing transient-state signals presents significant challenges but is well-suited for DL processing.

In literature usually there are two types of acquisitions [52], the multi channel sEMG and the high density sEMG. Both approaches come with their pros and cons. Sparse multi channel sEMG generates less data, reducing the need for data transfer and minimizing hardware costs. However, it is highly sensitive to variations

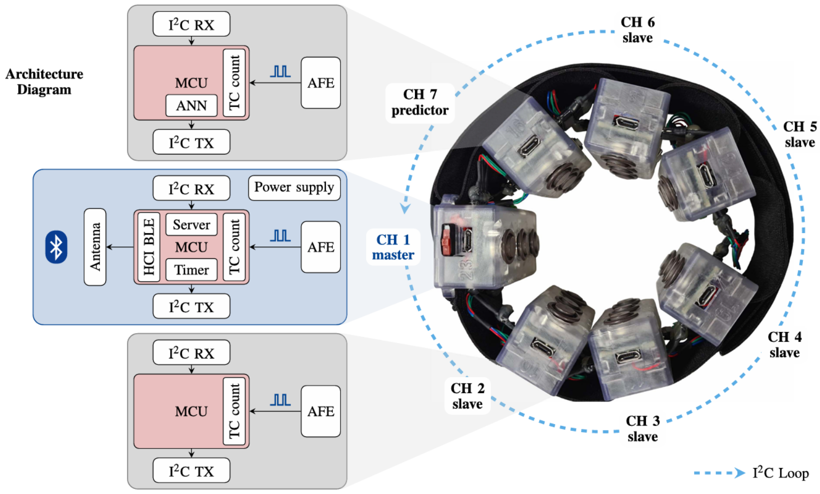

Figure 2.6: On the left, the architectural diagram illustrates the system structure: the master, represented in blue, handles the major workload, while the slave, depicted in gray, is responsible for counting the TC events. Additionally, CH-7 is designated for ANN predictions. On the right, the physical prototype is shown, consisting of an elastic band that holds together the power and case components while electrically connecting the boards [49].

in sEMG signals, which are a natural characteristic of these signals. In contrast, high-density sEMG employs a two-dimensional grid of electrodes to capture the spatial and temporal distribution of motor unit action potentials within the muscles. Although this method results in a larger volume of data, it offers higher recognition accuracy and better control quality.

Feature selection is an important step in constructing a DL or ML classifier. Feature extraction aims to enhance the information content within sEMG signals, thereby improving the distinction between different gestures. If the differences between gestures are more pronounced and there are fewer common features, the classifier's performance will improve, leading to fewer uncertain cases. As Li et al. [52] reported there are four different types of features that can be extracted from the sEMG signal.

Time domain (TD) features are derived directly from the raw sEMG signals, which vary over time. These TD features are simpler to compute compared to other sEMG features and are commonly used. However, incorporating a large number of time-domain features may not improve performance. In fact, it can sometimes degrade it due to the redundancy of these features.

Frequency domain (FD) features are obtained by applying the Fourier transform to the autocorrelation function of the sEMG signal. These features are then estimated using methods such as the periodogram or parameter estimation

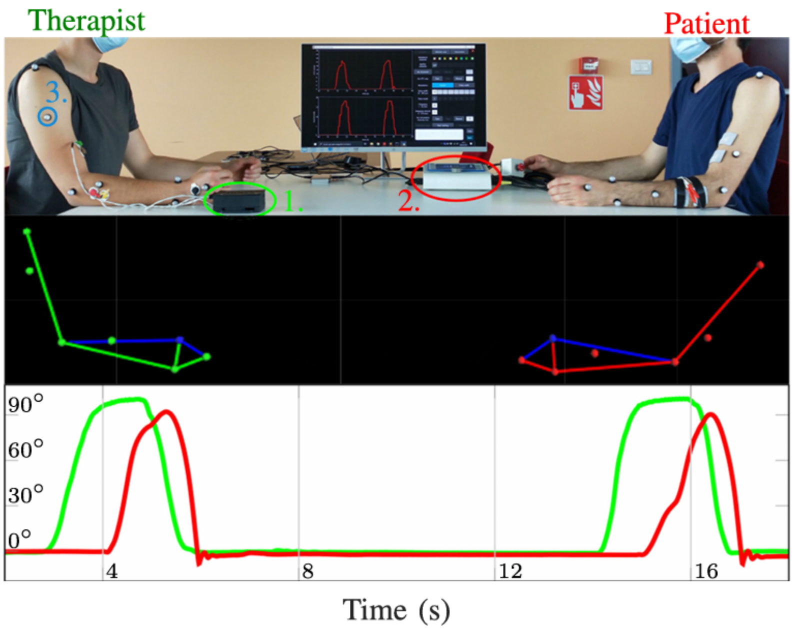

Figure 2.7: The therapist (on the left) is connected to the acquisition device, while the patient (on the right) is connected to the electrical stimulator. At the bottom, the elbow flexion trajectories are plotted using the Vicon system [50].

techniques.

Time-frequency domain features capture how the energy of the sEMG signal is distributed across both time and frequency. This approach is interesting for effective feature extraction. A common method for time-frequency analysis is the wavelet transform.

The parameter model consider the raw sEMG signal as a time series, focusing on its sequential information. The coefficients of the fourth-order autoregressive model can be used as important features for short periods of the signal.

The study conducted by Yu et al. [54] presents a method for recognizing six hand gestures, illustrated in Figure 4.7, using only two sEMG channels. Their aim was to enhance rehabilitation and human-machine interaction while reducing the number of sensors required. The authors developed a comprehensive system for data acquisition and processing, which includes filtering, endpoint detection, feature extraction, and classification employing a neural network. The experimental results demonstrated a recognition accuracy ranging from 96.41% to 99.70%.

Ding et al. [55] proposed a multi-scale Convolutional Neural Network (CNN) architecture for hand gesture recognition using sEMG signals. They used the

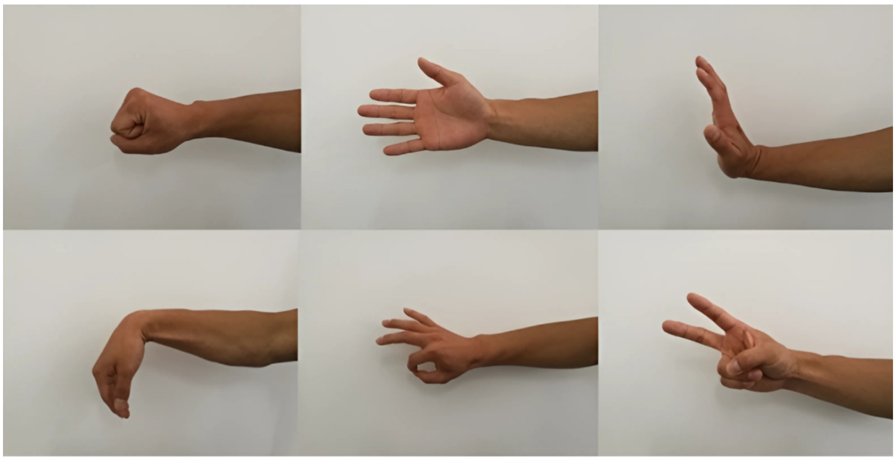

Figure 2.8: Movements executed in the study conducted by Yu et al. [54].

second database from the Ninapro project [56], 17 hand and wrist movements were analyzed. The proposed method accounts for muscle independence and employs filters of varying sizes to enhance classification accuracy, achieving a recognition accuracy of 78.86

Wang et al. [57] developed a Deformable Convolutional Network (DCN) to enhance gesture recognition using sEMG signals. The signals were recorded from ten electrodes on 27 subjects. These signals were transformed into feature maps for effective information extraction. The DCN combines traditional and deformable convolutional layers, resulting in a significant accuracy improvement over standard CNNs. The final accuracy was 81.8% for the first group, which includes 12 finger movements; 78.94% for the second group, which includes 20 gestures comprising both finger movements and hand postures; and 79.54% for the third group, consisting of a total of 29 gestures.

It is observed that in studies with a larger number of gestures, performance tends to decrease because some gestures share similar components, and inter-subject variability also plays a significant role.

Tam et al. [58] developed a real-time embedded system leveraging HD-sEMG to design a classifier for hand gesture recognition focused on finger counting. The gestures used for the classification corresponded to those illustrated in Figure 2.9a.

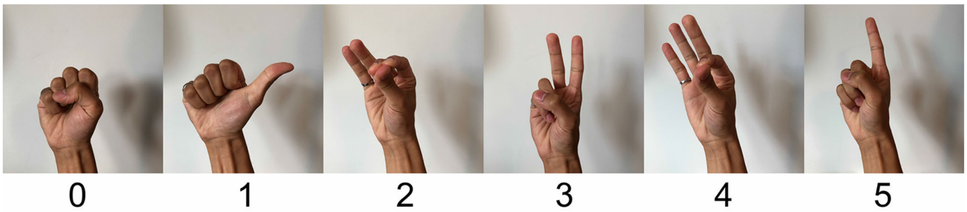

(a) A collection of six hand gestures, modeled after the movements commonly found in commercial hand prostheses, was employed for gesture recognition. Each gesture was designated a unique label and used as input for training the convolutional neural network [58].

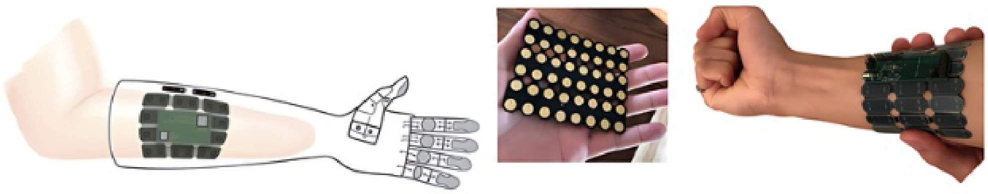

(b) Acquisition devices utilized in the study by Tam et al.

Figure 2.9: Hand gestures used for gesture recognition and the acquisition devices utilized in the study [58].

Inter subject variability, post-processing, and feature extraction

It is established in the literature that one of the main challenges is inter-subject variability, which represents an important limiting factor in the performance of classifiers [59]. An interesting study conducted by Zhan et al. investigated inter-subject and intra-subject variability using muscle synergies of the upper limb. The study found that inter-subject variability was greater than intra-subject variability, and both significantly exceeded the random level [60].

Post-processing techniques are often performed when working with sEMG signals, and particularly with sEMG during fine finger movements. Post-processing helps prevent the prosthesis controller from being overwhelmed by excessive information and can improve classifier performance by filtering out errors caused by unintended movements. [52]. Another technique that helps reduce inter-subject variability is the normalization. To address this challenge, Lin et al. developed a subject-specific normalization method, illustrated in Figure 2.10, aimed at improving classification performance [61]. The proposed approach involved a min-max scaling normalization, tailored individually for each subject. Specifically, for every new participant, a calibration trial was conducted to determine the minimum and maximum values of the recorded signals. These values were then used to normalize the data for that specific individual.

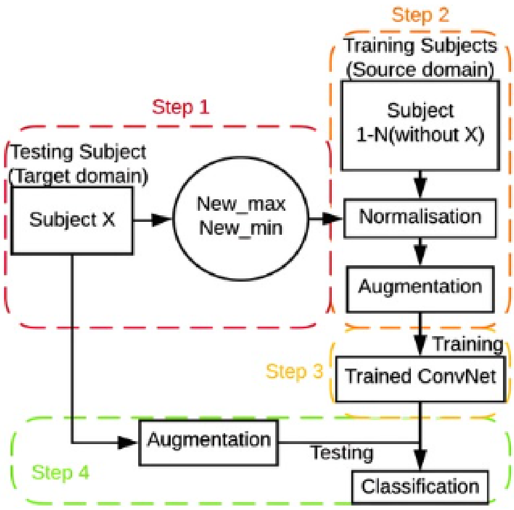

Figure 2.10: Pipeline of the project by Lin et al., highlighting and dividing the process into four distinct steps [61].

2.4 State of the art FES stimulation

The FES has been developing in the last years in neurorehabilitation with the goal to restore motor functions in individuals with neurological impairments. Peroneal nerve stimulation is one of the most common uses of FES in rehabilitation; it is particularly helpful to address foot drop in post-stroke patients. It uses electrical impulses to activate the tibialis anterior muscle, facilitating dorsiflexion during gait and improving walking patterns.

Although peroneal stimulation remains a benchmark for FES applications, research has also extended its scope to other areas, such as upper-limb rehabilitation. These advancements aim to leverage FES for functional hand recovery, addressing the complexities of fine motor control and muscle coordination required for activities of daily living.

Kottink et al. [62] conducted a randomized controlled trial investigated the effects of an implantable 2-channel peroneal nerve stimulator on footdrop in 29 chronic stroke patients. Over six months, participants using FES were compared to those using conventional walking aids, with assessments at multiple intervals. While no functional improvements in walking speed were observed, FES significantly increased the voluntary muscle output of the tibialis anterior and gastrocnemius muscles, suggesting neuromuscular plasticity. This study highlights the potential of peroneal nerve stimulation to enhance muscle activation in chronic stroke rehabilitation, even in the absence of functional gait improvements.

2.4.1 FES in upper-limb rehabilitation

In the study conducted by Kapadia et al. [63], FES was applied using a four-channel surface stimulation device to retrain upper-limb function in individuals with Spinal Cord Injury (SCI) and stroke. The FES system used by Kapadia et al. consisted of a four-channel surface stimulation device managed by software, allowing for a portable and user-friendly stimulator. The stimulator housed a programmed chip card and managed the delivery of electrical impulses to the target muscles, self-adhesive stimulation electrodes that were thin and flexible, designed for direct application to the skin to deliver electrical stimuli to the targeted muscles, and various man-machine interfaces.

Participants performed the following movements:

- *Grasp:* Practice gripping various objects of different sizes and weights to improve fine motor skills essential for daily tasks.
- *Reach:* Extend their arms to reach for objects placed at various distances. The main goal was to improve the range of motion and the coordination of the patient.
- *Lift:* Raise an object from a flat surface to help develop upper limb strength and control.
- *Hold:* Maintain a grip on objects for extended periods of time with the aim to improve endurance and stability.
- *Release:* Performed exercises focused on letting go of objects after grasping them, critical for completing everyday activities.

The results of the randomized trial indicated significant improvements in both grasp and reach functions in the FES group compared to the control group. Specifically, participants receiving FES demonstrated enhanced dexterity and control over their movements, which contributed to increased independence in daily activities.

The implemented FES system aimed to enhance hand movements in hemiplegic patients by using sEMG signals from contralateral hand muscles to control continuous power grasp and hand opening in the right hand via two stimulation channels. The system comprised a finite state machine, movement classifier, proportional mapping, and biofeedback control. Offline assessments with a healthy volunteer yielded an average classification accuracy of 81.72% for the movement classifier.

Successful online trials involved participants executing a six-step functional task, integrating power grasp and hand opening movements, with an average delay of 2.3 ± 0.35 seconds between the control signal onset and stimulation activation. The electrical stimulation device employed was the RehaStim 2 depicted in Figure 2.11 (HASOMED GmbH, Magdeburg, Germany). This sEMG-FES system demonstrated promise as an effective alternative for mirror therapy rehabilitation, aimed at improving motor function and independence among stroke patients by providing enhanced control over daily activities.

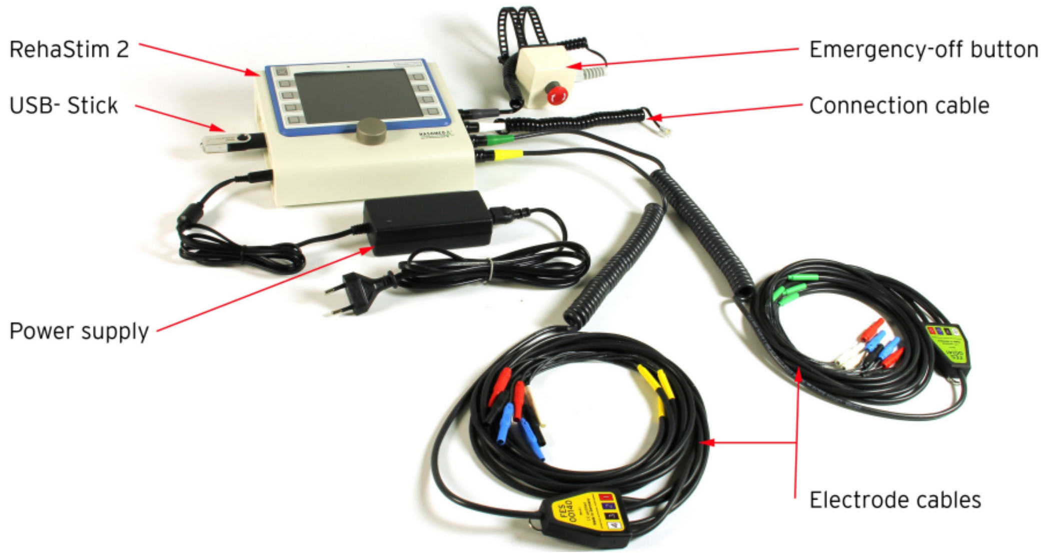

Figure 2.11: Rehastim 2 device produced by HASOMED [64].

FES using electrodes array

For FES stimulation, electrode arrays of multiple small electrodes arranged in specific configurations allow for more precise and selective muscle stimulation. However, this introduces an additional challenge in identifying the optimal electrode configuration for effective stimulation [65] [66].

Several studies have employed varying methodologies to explore the use of electrode arrays in FES for hand rehabilitation. One study utilized the Fesia Grasp system [67], a commercial FES device integrated with a garment containing a multi-field electrode that comprised 32 cathodes and 8 anodes. This system delivered biphasic pulse trains to stimulate wrist and finger movements. Five patients post-stroke participated in the study, where movements were analyzed based on activated cathodes, revealing the ability to generate multiple wrist and finger movements, with significant findings regarding extension and flexion rates [68].

Figure 2.12: Fesia Grasp system [67].

Another study investigated an array of 24 electrodes configured in two blocks for neuromuscular electrical stimulation. The study assessed the kinematic responses of eight healthy subjects to identify optimal stimulation patterns. The researchers used a combination of single-pulse scanning and telemetry recording. This combination reveals that specific activation patterns can be identified and applied to generate wrist and finger movements, demonstrating variations in responsiveness between stimulation patterns [69].

In a distinct study [70] investigating stroke patients, researchers developed a method using a 24-pad surface electrode array to create EMG maps of the paretic and non-paretic arms. This technique allowed for the selective targeting of muscles that displayed significant differences in EMG activity, enabling asynchronous stimulation that varied in intensity based on the degree of muscle involvement. This approach showcased the potential for improved functional grasp through targeted electrical stimulation [70].

Across these studies, implementing electrode arrays in FES demonstrated positive outcomes. The Fesia Grasp device confirmed the capability to generate diverse movements with high repeatability in both inter-subject and intra-subject terms. It achieved wrist extension more frequently than flexion, and the inter- and intra-subject variability was minimal, indicating that multi-field configurations could effectively adapt to individual anatomical differences [68].

The second study revealed that optimal stimulation patterns could be established, allowing for significant finger and wrist motion enhancement in healthy subjects. These selectivity measures were emphasized, with a direct comparison of behavioral outcomes indicating that targeted patterns resulted in superior movement execution [69].

In the third study, using EMG mapping provided insights into muscle activity variations, establishing stimulation zones determined by EMG differences between the healthy and affected extremities. This approach also yielded substantial functional improvements in grasping ability assessed through joint angles and force measurement [70].

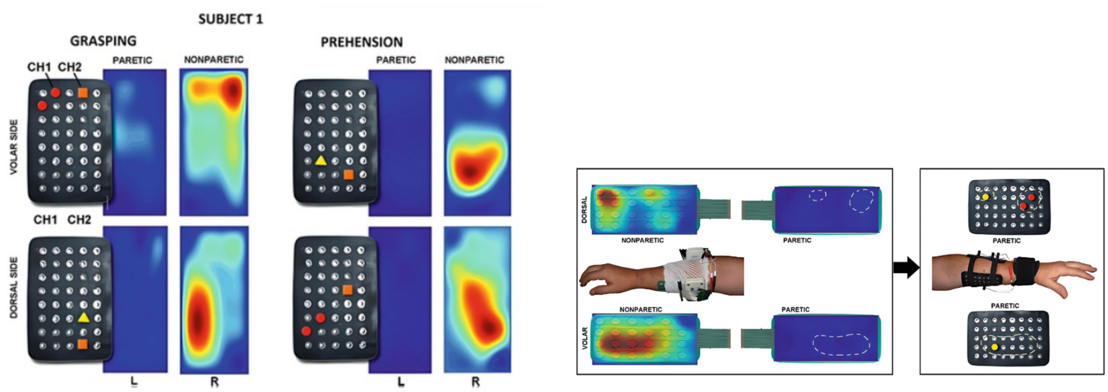

(a) Mapping of the EMG activity for non-paretic and paretic forearm muscles during hand opening [70].

(b) Identification of the regions where significant differences can be observed. Those areas indicate where the outputs from the stimulator should be applied [70].

Figure 2.13

The integration of electrode array technologies in functional electrical stimulation has emerged as a promising strategy for individuals with neurological impairments. The advancements in multi-field electrode systems provide improved selectivity and facilitate individualized rehabilitation approaches, supporting the execution of complex hand movements.

Innovative FES implementations

Novel and innovative approaches are present in the literature, exploring new applications to enhance the effectiveness of FES or to combine this type of stimulation with other tools. For instance, the study by Lypunova et al. [71] proposed a hybrid robotic rehabilitation system that integrated FES, triggered by sEMG, to improve early rehabilitation for stroke patients. The system included a rehabilitation robot named ROBERT, which facilitated leg press and dorsiflexion exercises, enabling the activation of partially or fully paralyzed muscles through FES. The results showed a high completion rate for the exercises, with 97% for the leg press and 100% for dorsiflexion. The FES current levels required to activate the muscles ranged from 20 to 53 mA for the leg press and 10 to 30 mA for dorsiflexion, generating forces between 43.0–141.2 N and 5.4–17.6 N, respectively.

Chapter 3

Preliminary Datasets Study

3.1 Hyser dataset

The High-Density Surface Electromyogram Recordings (Hyser) dataset was utilized to obtain This dataset comprises recordings from 20 healthy subjects. Before placing the electrodes, the skin was first prepped with an abrasive gel followed by cleaning with an alcohol pad. The instrumentation involved four electrode arrays, each consisting of 64 gelled elliptical electrodes arranged in an 8x8 layout. The inter-electrode distance was 10 mm, and the dimensions of each electrode were 5.8 mm along the major axis and 2.8 mm along the minor axis. The array were numbered as shown in Figure 3.1. For every subject they obtained 5 different datasets.

3.1.1 PR dataset

It is one of the 5 datasets and it includes 34 distinct movements. Each subject completed two repetitions of each gesture before progressing to the next. During each repetition, participants performed three dynamic tasks, each lasting 1 second, transitioning from a relaxed state to the specified gesture. Additionally, they completed a maintenance task, which required transitioning from a relaxed state to the target gesture and holding it for 4 seconds. To reduce the impact of muscle fatigue on sEMG signals, subjects were provided with a 2-second rest period between tasks and a 5-second rest period between repetitions. For each subject, a maximum of 204 dynamic tasks were recorded, with any erroneously performed movements being excluded from the dataset. On average, 2.30 ± 2.71 tasks were excluded per subject.

The movements showed in Figure 3.2 are: (1) thumb extension, (2) index finger extension, (3) middle finger extension, (4) ring finger extension, (5) little finger extension, (6) wrist flexion, (7) wrist extension, (8) wrist radial, (9) wrist ulnar, (10)

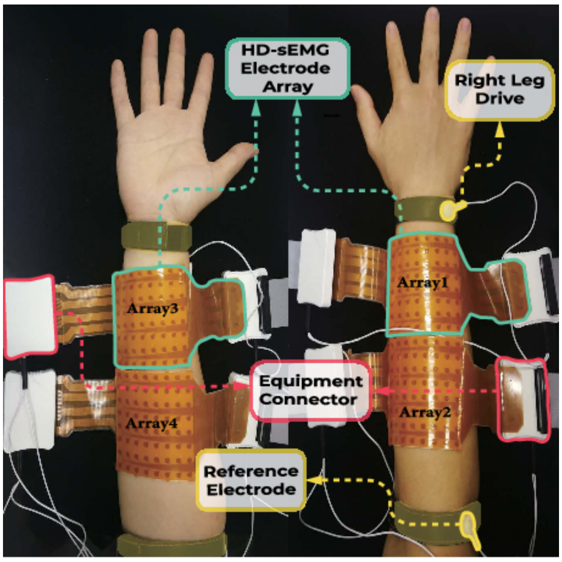

Figure 3.1: Setup used in the creation of the Hyser dataset, consisting of four electrode arrays, each containing 64 electrodes. Arrays 1 and 2 are positioned on the posterior side of the forearm, with array 1 placed distally and array 2 proximally. Arrays 3 and 4 are placed on the anterior side, with array 3 positioned distally and array 4 proximally.[72].

Figure 3.2: Representation of all the 34 movements performed in one trial [72].

wrist pronation, (11) wrist supination, (12) extension of thumb and index fingers, (13) extension of index and middle fingers, (14) wrist flexion combined with hand close, (15) wrist extension combined with hand close, (16) wrist radial combined with hand close, (17) wrist ulnar combined with hand close, (18) wrist pronation combined with hand close, (19) wrist supination combined with hand close, (20) wrist flexion combined with hand open, (21) wrist extension combined with hand open, (22) wrist radial combined with hand open, (23) wrist ulnar combined with hand open, (24) wrist pronation combined with hand open, (25) wrist supination combined with hand open, (26) extension of thumb, index and middle fingers, (27) extension of index, middle and ring fingers, (28) extension of middle, ring and little fingers, (29) extension of index, middle, ring and little fingers, (30) hand close, (31) hand open, (32) thumb and index fingers pinch, (33) thumb, index and middle fingers pinch, (34) thumb and middle fingers pinch.

3.1.2 Power maps

The script processes sEMG signals to identify active portions while ensuring the data quality necessary for accurate power calculation. Initially, a threshold based on the standard deviation of the signal is used to detect activation regions. For each identified point above the threshold, a moving window of 30 samples before and after the point is examined to confirm consistent activation. If any sample within this window exceeds the threshold, the corresponding segment is retained as part of the active signal.

To ensure data quality, only signals with a sufficient number of valid samples are considered. A larger moving window of 70 samples is applied to the signal to ensure consistent activity within the window. Only samples meeting this criterion are marked as valid. Signals with fewer than 50 valid samples are excluded from further analysis. Additionally, signals with a maximum amplitude exceeding 1.5V are discarded, as this indicates channel saturation or insufficient data quality.

The resulting signal is processed to remove its mean value, and its power spectral density (PSD) is then calculated using the Welch method. The calculated power values are stored in a structured format, with a dedicated field for each patient. These power values are used to generate color maps, which help determine the optimal placement of the Apollux devices. After calculating the power for each signal and patient, the average power across repetitions for each movement is computed.

These averages were then summed across patients to obtain a single value for each movement. This process resulted in a structure containing 34 fields, corresponding to each movement. Each field comprises four matrices, one for each electrode array. Each matrix is 64x8, representing the single differential electrodes by the columns of electrodes.

Sum of the color maps to obtain the recording sites

The graphical representation of the color maps was achieved by visualizing all four arrays, with each array depicted as an 8x8 grid to represent the individual electrodes.

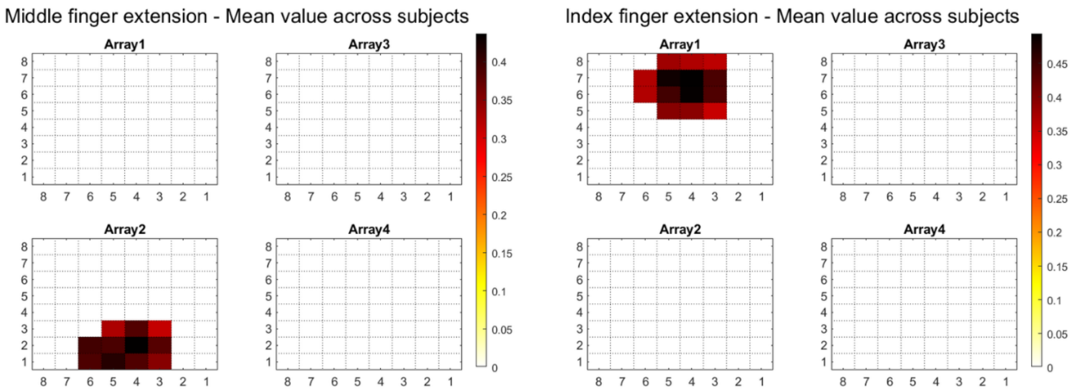

Figure 3.3: Power maps obtained as described: on the left, the map corresponds to middle finger extension, while on the right, it corresponds to index finger extension.

The processing pipeline begins by organizing the power values for each participant, gesture, and electrode array into a structured format. This step ensures that the data is consistently stored and accessible for subsequent analyses.

To provide a comprehensive view of the data, the average power across all participants for each gesture and electrode array were computed. In this step only the non-zero values very considered, ensuring that missing or invalid data does not skew the results. The average power values are then reshaped into 8x8 grids to reflect the physical layout of the electrodes, allowing for intuitive spatial interpretation.

Subsequently the maximum power value for each gesture across all arrays was used in a thresholding step, setting all values below 70% this maximum to zero. The purpose of this approach was to highlight the most significant activations while suppressing noise or less relevant activity.

To further contextualize the data, the script determines the overall maximum and minimum power values for each gesture. These extrema are used to normalize the visual representation of the power distributions.

Finally, the processed data is visualized using color maps. Each array is displayed as a heatmap, with gridlines overlaid to delineate individual electrode positions. The maps are annotated with color scales representing the range of power values.

3.2 GRABMyo Dataset

The dataset was created by Pradhan et al. [73]; 43 patients were enrolled, 23 females and 20 males. The study took place across three separate days: the first, eighth, and twenty-ninth days. The participants consisted of students and staff members from the University of Waterloo. The average participant was 26.35 years old. Additionally, the average forearm length, measured from the styloid process of the wrist to the olecranon of the elbow, was 25.15 cm, with a standard deviation of 1.74 cm.

The sEMG signals were captured using the EMGUSB2+ amplifier (OT Bioelettronica, Italy), with a gain of 500 and a sampling rate of 2048 Hz. Monopolar sEMG electrodes (AM-N00S/E, Ambu, Denmark) were pre-gelled and adhered to the skin. Prior to the experiment, the length of the participants' forearm was measured from the olecranon process to the ulnar styloid process. The forearm circumference was taken one-third of the way down from the olecranon, while wrist circumference was measured 2 cm from the ulnar styloid. The skin was prepared

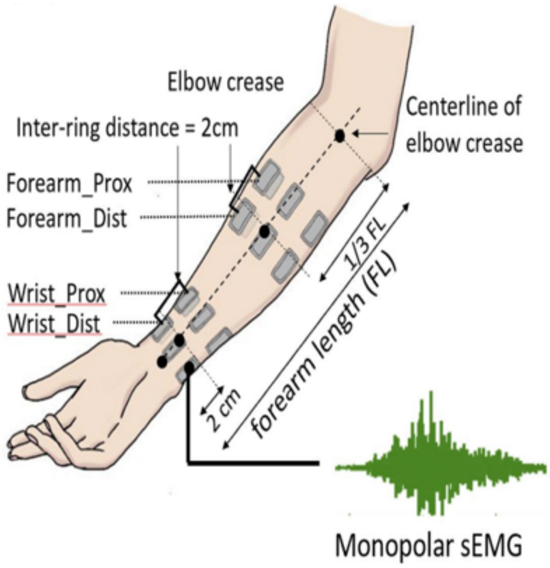

Figure 3.4: The setup used to record the GRABMyo dataset includes two rings placed on the wrist and, proximally, on the forearm, considering the centerline of the elbow crease as the anatomical landmark [73].

by shaving, cleaning with alcohol, and lightly abrading the surface. Sixteen sEMG electrodes were placed around the forearm in two rings, as represented in Figure 3.4, each with eight electrodes forming eight bipolar pairs, spaced 2 cm apart. Similarly, twelve electrodes were arranged in two rings around the wrist, each with six electrodes forming six bipolar pairs, also spaced 2 cm apart. Altogether, 28 electrodes were used per session, creating four electrode rings for both the forearm and wrist. 16 gestures, illustrated in Figure 3.5, were performed in a randomized order for every recording, those movements were: Lateral prehension (LP), thumb adduction (TA), thumb and little fnger opposition (TLFO), thumb and index fnger opposition (TIFO), thumb and little fnger extension (TLFE), thumb and index fnger extension (TIFE), index and middle fnger extension (IMFE), little fnger extension (LFE), index fnger extension (IFE), thumb extension (TE), wrist fexion (WF), wrist extension (WE), forearm supination (FS), forearm pronation (FP), hand open (HO), and hand close (HC). Each participant completed seven runs,

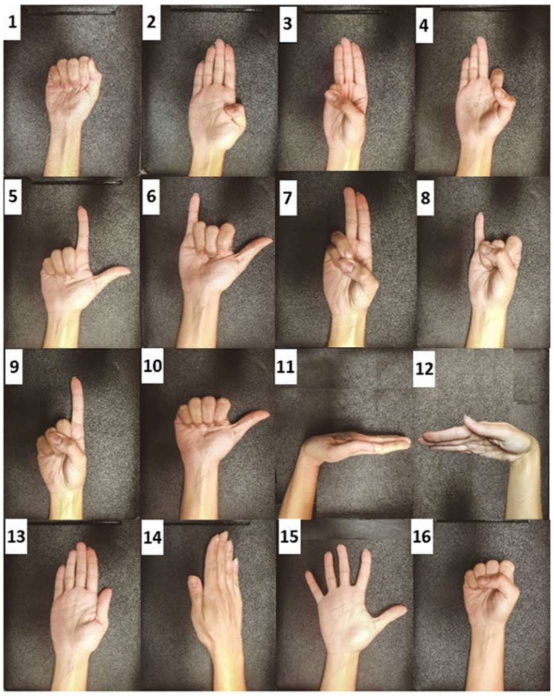

Figure 3.5: Representation of the 16 movements performed by the subjects in the GRABMyo dataset [73].

totaling 119 contractions (17 per run). If any accidental gestures occurred or there were instances of no activity or delayed responses, replacement contractions were performed after each run to ensure accuracy. Participants were also allowed to take additional breaks whenever needed. The entire process was repeated on day 8 and day 29. The participants were instructed to perform the gestures at a normal force level, or similar to how they would normally do it during daily activities, and all the sEMG recordings are 5s in duration.

The sEMG signals were processed using a fourth-order Butterworth filter with a bandpass range of 10Hz to 500Hz. Additionally, a 60Hz notch filter was applied to eliminate any power line interference.

3.2.1 Signals of the GRABMyo dataset

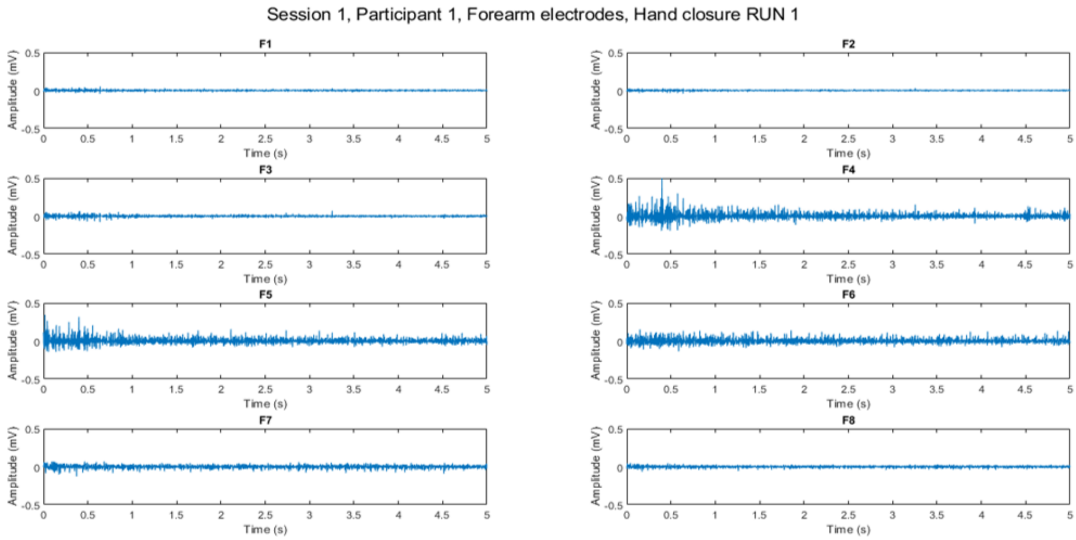

Figure 3.6: sEMG signals recorded from forearm electrodes (F1–F8) during hand closure movement for Subject 1, Session 1, Run 1. Each subplot represents the amplitude of the signal over time for individual electrodes, highlighting the varying signal intensities across different channels. Notably, electrodes F4 and F6 show stronger muscle activations compared to others, suggesting varying muscle contributions during the movement.

As shown in Figure 3.6, the signals do not exhibit clearly defined activation moments. This is due to the higher baseline values observed in the electrodes with greater activation, such as channels F4, F5, and F6, making it challenging to distinctly identify the onset and termination of muscle effort. I then developed a MATLAB script to replicate the threshold calculation and consequently obtain the ATC signal, enabling a comparison with the original sEMG signals. As shown in Figure 3.7, it is evident that, as expected, the onset and termination of the contraction are not clearly discernible in the ATC signal, similar to what was observed with the sEMG signal.

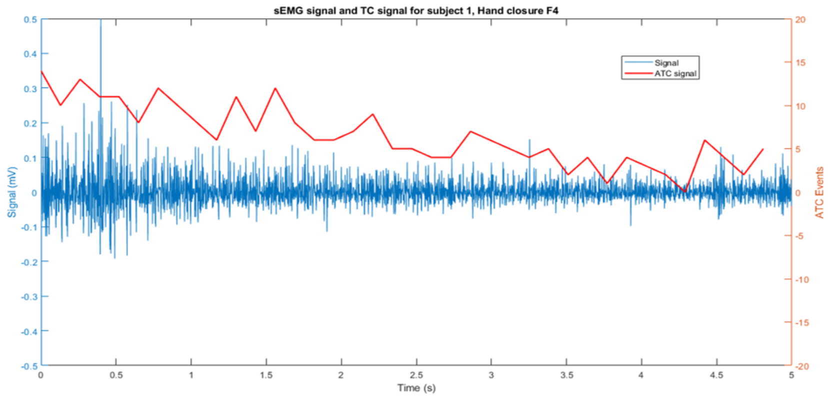

Figure 3.7: Superimposed plot of the sEMG signal (blue) and the calculated ATC signal (red) for Participant 1 during hand closure, recorded from electrode F4. The sEMG signal represents the electrical activity of the muscles over time (left y-axis), while the ATC signal, derived from the sEMG, shows the estimated torque exerted by the muscles (right y-axis). The use of separate y-axes allows for a clear comparison between the muscle activation and the resulting torque across the same time interval.

3.2.2 Radar Plots

To analyze the dataset, radar plots and similarity matrices were generated. The radar plots represent the movement of individual subjects across different runs, providing a visualization of intra-subject variability. Specifically, each radar plot captures the variability of muscle activation for a given movement by illustrating the 40th percentile, median, and 60th percentile of ATC values for each channel (F1–F8) across the runs of the same subject. This analysis was performed using MATLAB to assess how consistent the muscle activation patterns are between repeated trials of the same gesture within each subject.

These radar plots provide insight into which channels are most activated and also indicate the intensity of activation. As mentioned, a higher ATC value corresponds to a greater intensity of muscle activation.

Radar plots were used to assess the activation intensities using the ATC signal, as well as to identify the muscle regions most engaged during a given movement. Figure 3.8 clearly illustrates how the activation level differs between wrist flexion and extension, and how the regions of greatest activation are located on channels positioned opposite to each other. This is consistent with expectations, as wrist flexion predominantly engages the flexor muscles, while wrist extension recruits the extensor muscles.

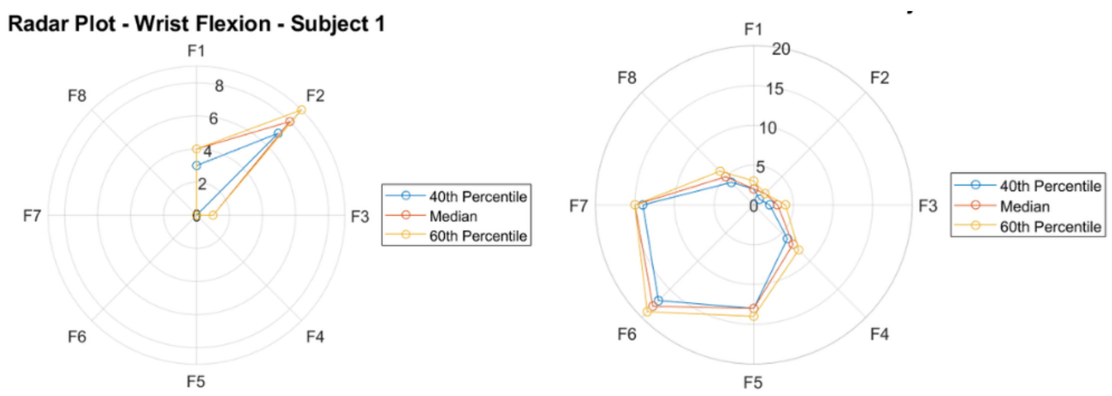

Figure 3.8: Comparison of muscle activation during wrist flexion (left) and wrist extension (right) for Subject 1. The radial plots display the 40th percentile, median, and 60th percentile activation levels across the eight channels on the forearm. The plots highlight distinct activation patterns between flexion and extension, with opposite regions showing higher activation, corresponding to the engagement of flexor and extensor muscles.

3.2.3 Similarity matrices

Similarity matrices are employed to analyze two key aspects of muscle activation: intra-subject similarity, which assesses consistency across different runs of the same subject, and inter-subject similarity, which evaluates the coherence of muscle activation patterns between different participants. In this context, the analysis aims to measure how consistently subjects perform specific gestures across multiple runs and how comparable these performances are between individuals.

For intra-subject analysis, the goal is to determine the stability and repeatability of muscle activation during repeated executions of the same movement by a single subject. Low variability between runs indicates that the subject is able to perform the gesture consistently, suggesting good motor control. Conversely, higher variability could signal difficulties in motor coordination or the onset of muscle fatigue, as the pattern of muscle activation changes across runs.

In the inter-subject comparison, the similarity matrices allow for the assessment of muscle activation patterns across different subjects performing the same gesture. This comparison highlights commonalities or differences in the motor strategies employed by individuals, which can be particularly informative when comparing groups with different characteristics, such as healthy subjects versus patients with motor impairments.

Thus, similarity matrices provide a comprehensive view of both intra- and inter-subject variability, offering insights into the consistency and variability of muscle activation during task performance. This information is crucial for evaluating motor control strategies, identifying potential issues with gesture reproducibility, and distinguishing between typical and atypical patterns of muscle activation.

Calculation of Similarity Matrices

To evaluate the similarity between subjects and their movement patterns, similarity matrices were computed using muscle activation data recorded via ATC signals from the forearm. For each participant and gesture, movement matrices were constructed by aggregating data from multiple repetitions of hand gestures across different runs. A correlation-based approach was employed to compare the muscle activation profiles between subjects and epochs.

The norm values of the recorded signals were computed for each trial to quantify the magnitude of muscle activity using the following equation:

$$\text{NormValue} = \sqrt{\sum_{i=1}^{N_{\text{channels}}} \left(X_{\text{Subj}_{n_{\text{run}},\text{participant}_{\text{idx}},i}}\right)^2} \tag{3.1}$$

In this equation, $X_{\text{Subj}_{n_{\text{run}},\text{participant}_{\text{idx}},i}}$ represents the ATC values recorded from the i-th channel during a specific trial (n_{run}) for a particular participant ($\text{participant}_{\text{idx}}$). The summation is performed over all channels, where N_{channels} denotes the total number of channels utilized in the acquisition system.

Trials with norm values falling below a predefined threshold were relabeled as 'rest' to distinguish them from active gestures. Specifically, if the calculated NormValue was less than the defined threshold (e.g., 5), the label of the trial was changed to indicate 'rest.' This approach was essential for eliminating false activations, ensuring that only trials exhibiting significant muscle activity were considered in subsequent analyses.

The similarity between pairs of subjects was evaluated by extracting movement matrices corresponding to specific gestures (e.g., wrist flexion). For each pair, a channel correlation matrix CCxy_{tot} was calculated to assess the degree of similarity between the muscle activations from each forearm channel. This was done by computing the cross-correlation between corresponding channels in the movement matrices of two subjects. Specifically, for each channel c, the cross-correlation between the signals x_c and y_c of the two subjects was calculated using:

$$\text{CCxy}_c = \frac{\text{xcorr}(x_c, y_c)}{\max\left(\|x_c\|^2, \|y_c\|^2\right)} \tag{3.2}$$

where $\text{xcorr}(x_c, y_c)$ is the cross-correlation of the signals, and $\|\cdot\|$ denotes the Euclidean norm.

Next, a weight vector Wxy_{tot} was computed to quantify the relative contribution of each forearm channel to the overall movement similarity. For each channel c, the weight Wxy_c was determined based on the sum of the signal amplitudes from both subjects:

$$Wxy_c = \frac{\sum x_c + \sum y_c}{\sum \mathrm{matrix}_x + \sum \mathrm{matrix}_y} \tag{3.3}$$

where $\sum x_c$ and $\sum y_c$ represent the sum of the signal amplitudes for the given channel, and $\sum \mathrm{matrix}_x$ and $\sum \mathrm{matrix}_y$ are the total sums of all channels' signals for both subjects.

Finally, the similarity index $\mathrm{SIxy}_{\mathrm{value}}$ for each subject pair was calculated by multiplying the transposed correlation matrix $\mathrm{CCxy}_{\mathrm{tot}}^{\top}$ by the weight vector $\mathrm{Wxy}_{\mathrm{tot}}$, and selecting the maximum value:

$$\mathrm{SIxy} = \max\left(\mathrm{CCxy}_{\mathrm{tot}}^{\top} \cdot \mathrm{Wxy}_{\mathrm{tot}}\right) \tag{3.4}$$

These similarity indices were then used to populate a similarity matrix, where rows and columns represent different subjects and runs, with diagonal elements set to zero to focus on inter-subject comparisons. Visual representations of the similarity matrices were generated using heatmaps, with color intensity indicating the degree of similarity between subjects.

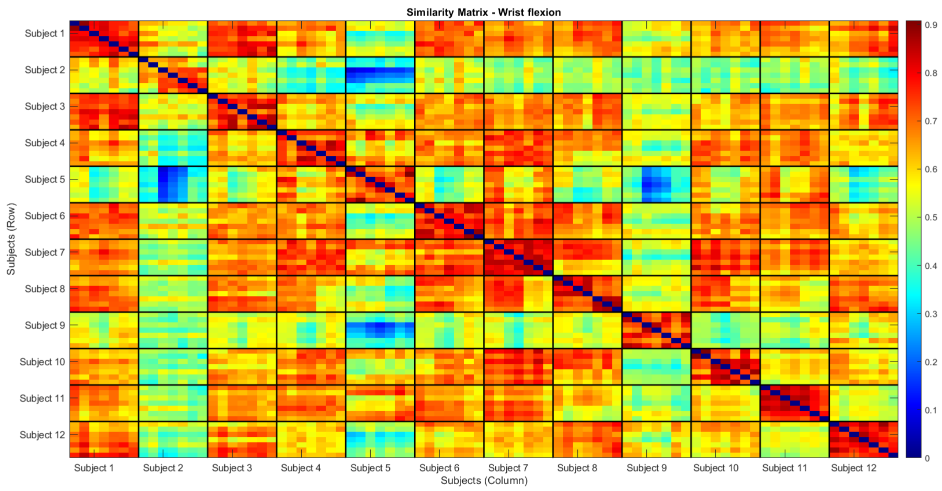

Figure 3.9: Similarity matrix for wrist flexion movement across 12 subjects. The matrix represents the correlation of muscle activation patterns recorded from the forearm during wrist flexion, with each cell indicating the similarity between two subjects. High similarity is shown by warmer colors (yellow/red), while lower similarity is represented by cooler colors (blue).

In Figure 3.9 and Figure 3.10, a significant difference in variability is evident between different subjects compared to within the same subject across different

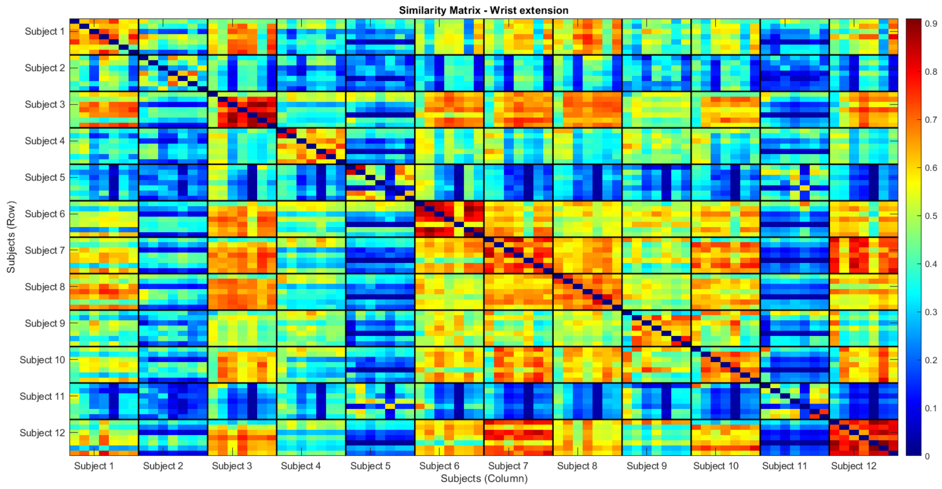

Figure 3.10: Similarity matrix for wrist extension movement across 12 subjects. The matrix represents the correlation of muscle activation patterns recorded from the forearm during wrist flexion, with each cell indicating the similarity between two subjects. High similarity is shown by warmer colors (yellow/red), while lower similarity is represented by cooler colors (blue).

runs for distinct movements. This suggests that certain movements are easier and more repeatable. The underlying causes may be a lower number of muscles involved or the contribution of stronger muscles, which makes their activation more evident, thereby facilitating the discrimination of the movement. In general, as shown in Figure 3.10, intra-subject variability is generally low, whereas inter-subject variability is notably high. This makes accurate classification challenging, as subjects produce different muscle signals despite performing the same movement.

3.3 Dataset study consideration

Subsequently, the power maps obtained using the Hyser dataset were used to determine the correct placement of the acquisition devices during the recording session. The high-density array-electrode approach used in this dataset allows for power maps with high spatial resolution, enabling precise identification of the region with the greatest activation.

The GRABMyo dataset was useful for assessing the high inter-subject variability, a well-known issue in this kind of research. This finding reaffirms what has already been reported in the literature and in section 2.3, where, although subjects may exhibit clear activations, differences between individuals are evident.

Chapter 4

Acquisition System

4.1 Hardware components

Six Apollux devices were used for the data acquisition, every device was equipped with a battery and gold-plated electrodes. These devices recorded signals and transmitted data to the computer via Bluetooth Low Energy using USB BLE dongles, specifically the Nordic Semiconductor nRF52840 [74] that is illustrated in Figure 4.1. The nRF52840 dongle, is designed for efficient wireless communication. The proposed setup enabled seamless communication between the Apollux devices and the computer, ensuring efficient data transfer that will be used for subsequent analysis.

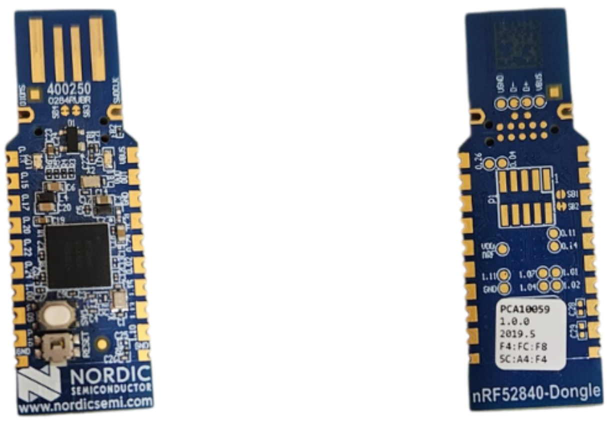

Figure 4.1: Front and rear view of the Nordic Semiconductor nRF52840 device.

The Apollux devices, including batteries and electrodes, are shown in Figure 4.3. The electrodes had an Inter-Electrode Distance (IED) of 1.5 cm and a diameter of

0.8 cm. The Apollux device consists of two components: the Analog Front End (AFE) and the digital processing unit [33].

- The AFE, illustrated in Figure 4.2, is responsible of the detection of the raw sEMG signals and the generation of the TC events from it. The AFE is designed for differential signal acquisition using two sensing electrodes and a reference electrode. It is offers a transfer function between 70 Hz and 400 Hz with a default gain of 500 V/V, adjustable through multiplication factors such as ×2, ×3, ×5, or ×6. The final stage of the AFE includes a voltage comparator that applies a calibrated threshold to the analog sEMG signal to generate a quasi-digital TC signal.
- The digital processing unit is based on the Apollo3 Blue microcontroller; because one of its strength is the ultra-low power consumption, making it suitable for portable and battery-powered devices [33]. This unit is responsible for the computation of ATC values and also facilitates efficient data transmission. Together, the AFE and the digital processing unit enable accurate signal acquisition and real-time processing.

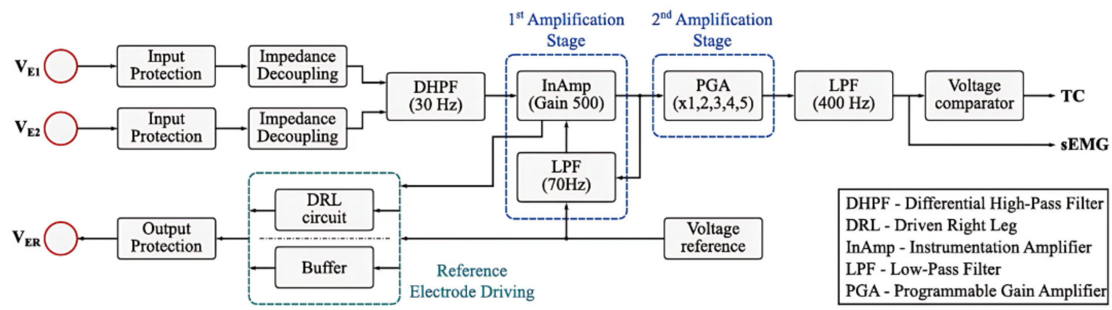

Figure 4.2: Schematic representation of the proposed Analog Front End, which amplifies the sEMG signal by a variable gain (×500–×2500) within the 30 Hz–400 Hz bandwidth. The final stage extracts the Threshold Crossing signal [34].

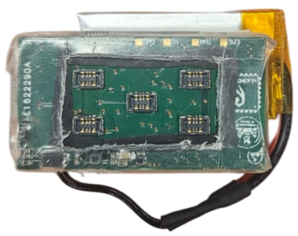

(a) Apollux bottom view.

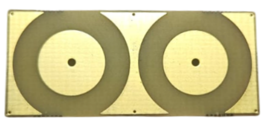

(b) Gold-plated electrode.

(c) Frontal view recording device.

Figure 4.3: Apollux device used for recording: on the left, the bottom side of the Apollux where the electrode should be placed; in the middle, the gold-plated electrode with IED of 1.5 mm. On the right, the frontal view of the device showing the electrode and the battery.

4.2 Acquisition software

The signal acquisition software, developed by the research group, is built using the Python programming language and incorporates several key features that aim to improve its functionality and usability. One of the most important components of the system is the Blatann library, which facilitates the connection between Apollux devices and USB BLE dongles, specifically the Nordic Semiconductor nRF52840.

The software's standout characteristic lies in its modular framework, which is achieved through an architectural strategy centered around autonomous components that interact seamlessly via Application Programming Interfaces (APIs). This modularity is a direct result of employing the Object-Oriented Programming (OOP) paradigm.

The software is designed with the following key characteristics to ensure its robustness and adaptability:

- *scalability:* The software is capable of supporting both single-device and multi-channel acquisition while maintaining real-time functionality.
- *modularity:* This characteristic is achieved thank the system structure based on independent modules that interact through APIs, a result of using OOP principles.
- *extensibility:* The software is built to be maintainable and it has structured that easily allows to implements updates or expansions. This includes the ability to replace system components (e.g., BLE dongles) without disrupting the overall system, by simply modifying the corresponding module to accommodate new APIs.
- *reliability:* Ensuring data integrity is very crucial. In order to achieve this the software incorporates checks on both received and transmitted data to minimize errors and notify the user of any issues, thus guaranteeing reliable data acquisition.

4.2.1 Acquisition software structural layer

The control software is structured in an OOP paradigm, consisting of three main components that interact with each other, as illustrated in Figure 4.4: the BLE module, the Apollux object, and the GUI.

At the lowest level there is the BLE module, which serves as the direct interface to the antenna. When a BLE dongle is used on a laptop, communication is managed through the Pyserial module [75]. This implementation maintains a consistent set of properties and functions to enable BLE operations. The most important features of this modules are: detecting broadcasting devices, establishing wireless links, and facilitating data transmission through client-server interactions or real-time notifications.

The second, intermediate layer is the Apollux object, which serves as a custom module replicating the functionalities of the corresponding device. It acts as an intermediary between the BLE module and the GUI, handling bidirectional packet management between these two layers. Each connected acquisition board is paired with a unique Apollux object, enabling parallel processing across multiple devices.

The topmost layer is the Graphical User Interface (GUI). The GUI was developed using the Kivy framework, which is compatible with Python. The GUI was designed to guide the user during the recordings and simplify the interaction between the user and the acquisition system. The GUI includes specialized widgets like buttons, graphs, pop-ups, and spinners.

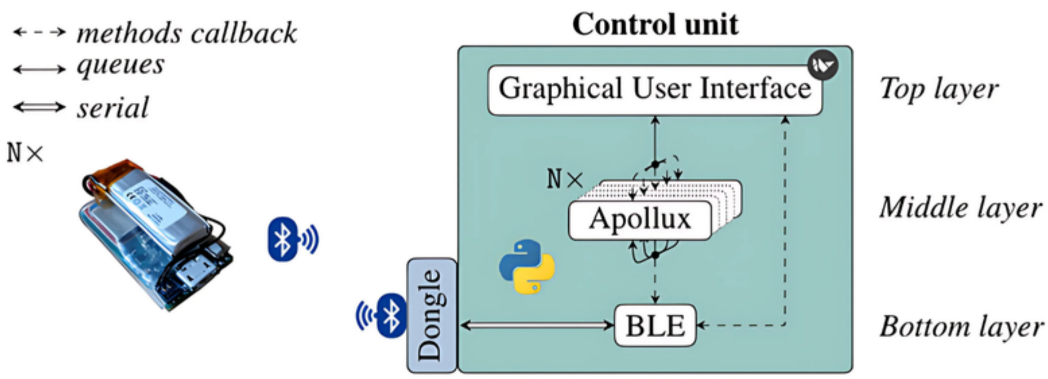

Figure 4.4: The diagram illustrates the three-layered structure of the control unit. The bottom layer consists of the BLE module, which manages wireless communication with Apollux boards. The middle layer is represented by the Apollux object. The top layer is the GUI. Different types of data transmission are depicted in the figure.

The data flow is managed using queues. The top-down functions of the software are activated through method callbacks, while data communication is handled via internal queues that manage data transmission between the three previously described layers.

Specifically, the BLE module forwards incoming packets from the Apollux boards to the appropriate queue, tagging them based on message type. The Apollux object retrieves these packets, processes the data, and either passes them to internal methods or directly to the GUI for display such as ATC or sEMG values. Once the data is processed, the GUI either displays or saves it accordingly.

4.3 Graphical user interface and acquisition software modifications

The GUI used to guide the user during the recording phase, shown in Figure 4.5, was developed using the Kivy Python-compatible framework, like the one used in the initial software. The '*Initialize*' button starts the connection process for the

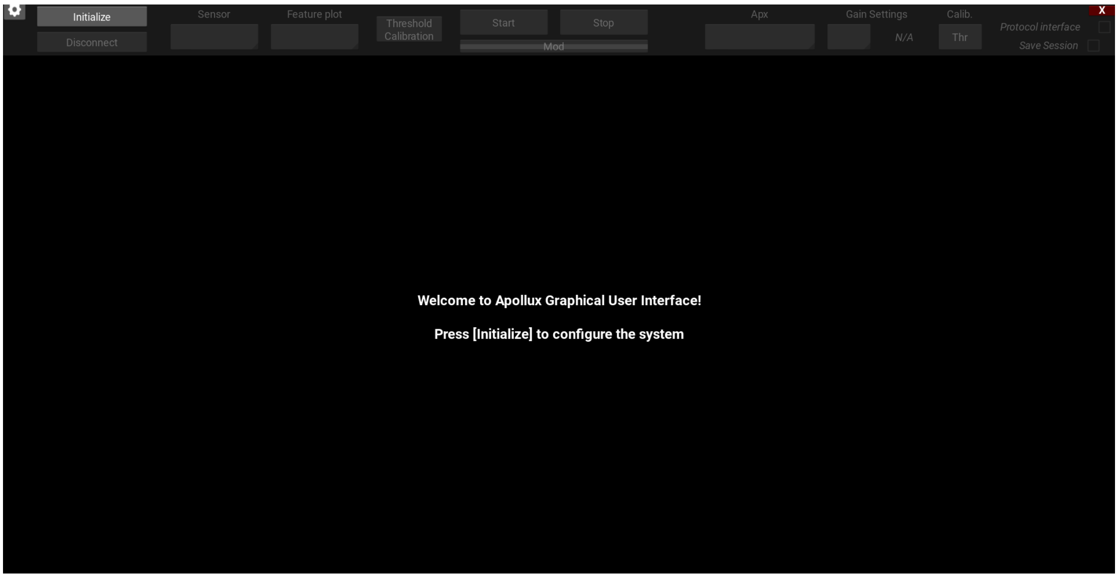

Figure 4.5: The initial screen of the GUI upon launching the software for data recording, where all buttons are disabled except the one for connecting the Apollux devices.

dongles and scans for available Apollux devices. A popup window is then displayed, allowing the user to select the devices to connect.

After the devices are connected, the user can select the preferred recording modality. By pressing the '*Mod*' button, a popup window opens, allowing the user to choose the modality to be recorded. As represented in Figure 4.6, multiple modalities can be recorded simultaneously. The system uses a queue structure (queue.Queue in Python) to ensure asynchronous and efficient management of the acquired data, avoiding the risk of packet loss. Real-time data is received and inserted into dedicated queues for each device, enabling parallel processing of the information.

When recording two or more signals, the queue management follows the same approach as when recording a single modality. However, in this case, a dedicated queue is assigned to each signal, allowing simultaneous management of multiple queues without relying on a single queue, which could lead to congestion and potential data loss. This approach ensures the effectiveness of using separate queues, as the initial synchronization process aligns all data queues across signals and devices. The acquisition also relies on a threading mechanism, where each BLE device is associated with a separate thread responsible for the continuous reading of incoming packets and their storage in structured text files. Each packet contains information such as the timestamp, signal value, and the corresponding movement class. The system allows the simultaneous management of multiple devices, synchronizing the acquired data and ensuring continuous recording until manual process termination.

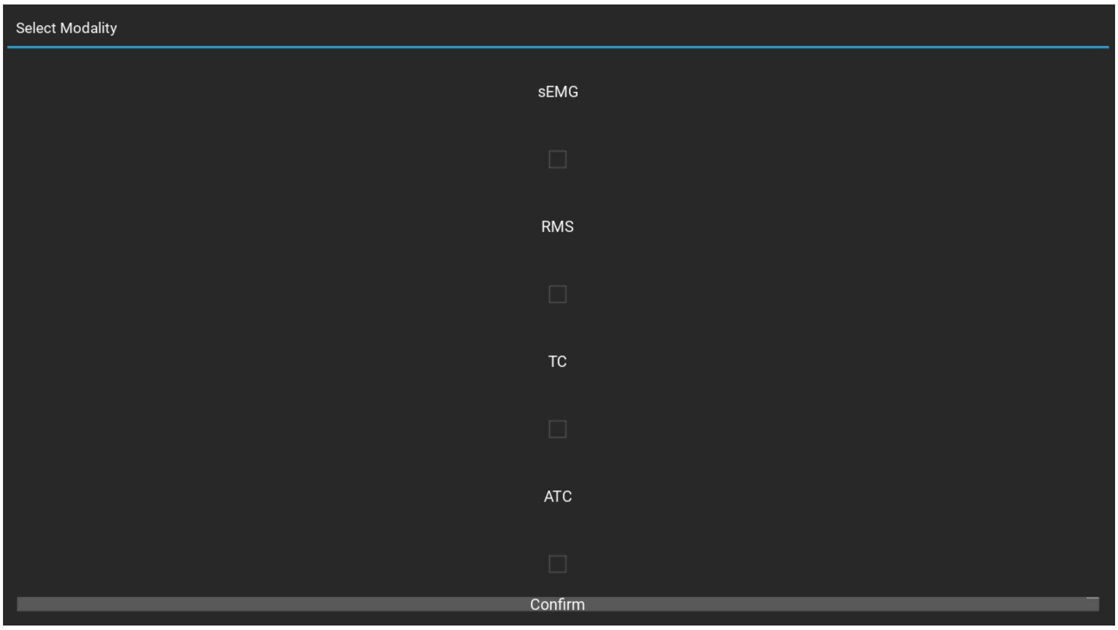

Figure 4.6: Checkbox to selected the modalities to save during the recording.

The '*Threshold Calibration*' button is used to start the threshold calibration process for each connected device. This threshold calibration is described in section 1.12. During this calibration, it is important that the subject must remain still and avoid any movement to ensure an accurate threshold calculation, which is a crucial step, as the ATC signals were used in the subsequent classification phase. In the GUI, there are buttons identifying each Apollux device, which are used to manage individual properties, such as the gain, labeled as '*Gain Settings*'. The gain can be configured differently for each device. The Start and Stop buttons are used to begin and end the recording, respectively. When the *Start* button is pressed, the system initializes the acquisition mode (which can include sEMG, RMS, TC, and ATC) and performs device synchronization, including threshold calibration for TC or ATC signals if required. During initialization, any inactive or disconnected

Figure 4.7: GUI after selecting the recording modalities during the session.

devices are removed from the list, and dedicated files for each active acquisition mode are created when the 'Save Mode' is activated via the checkbox in the top right corner. In 'Save Mode', the recorded signals are saved in .txt files, with each file corresponding to a different modality and each device maintaining its own file to prevent data congestion.

Pressing the *Stop* button halts the acquisition process by stopping the data management thread, stopping the data recording on each device, while handling any potential failures in stopping a device, and closing any open data files. The system then clears all data queues and removes any disconnected devices, ensuring a clean termination of the recording session.

The *Feature plot* button allows the user to choose which modality to display among the recorded options. In this way, the user can decide whether to plot an ATC signal to evaluate the accuracy of the threshold calculation, or, for example, view the sEMG signal.

4.4 Protocol Interface

The protocol interface was designed to help and guide the subject throughout the recording process. A secondary screen displays the protocol interface, illustrated in Figure 4.8. This interface shows the current gesture that the subject must perform, also a visual representation of the name of the movement is displayed on the bottom. To help to perform the movement with the right timing, the "next

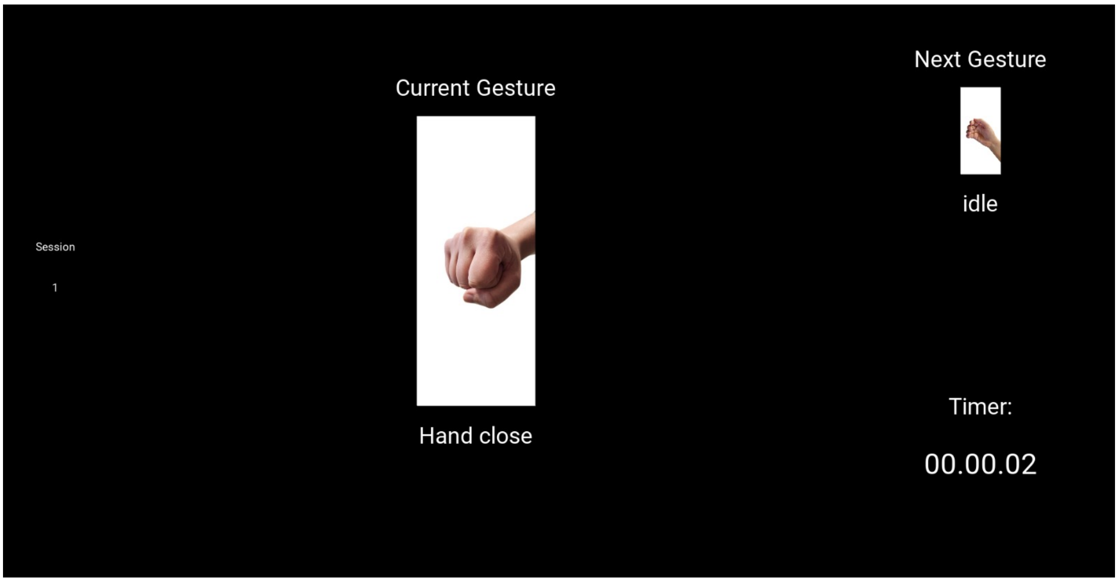

Figure 4.8: GUI guiding the subject during acquisition, displaying the current gesture to perform, the next gesture, and a timer for the duration of the current movement.

gesture" is displayed on the right side of the screen, ensuring a correct transition between gestures. Additionally, a timer is provided to indicate the duration for which the subject needs to perform the current gesture. Additionally, on the left, the recording session in progress is displayed, with numbers ranging from 1 to 3.

At the end of the protocol, an image is displayed on the screen to indicate the successful completion of the procedure. The final message on the screen is shown in Figure 4.9.

The protocol was interrupted and repeated if, during the recording, the Apollux devices started to lose data packets, resulting in the loss of signal values and the generation of NaN (Not A Number) values. This was done to ensure the creation of a more robust dataset.

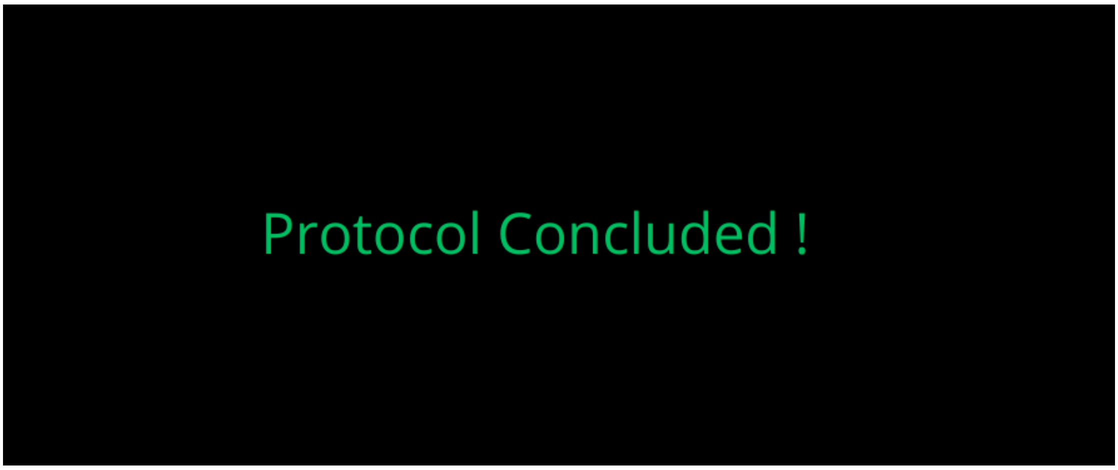

Figure 4.9: Message of successful protocol completion.

Chapter 5

Protocol and Device Positioning

The adoption of this protocol ensures a standardized and systematic approach, using anatomical proportions such as the subject's forearm length and the wrist circumference. The protocol was designed to target in a selective manner muscles or muscle regions associated with specific hand gestures, enhancing the precision and selectivity of the measurements.

The information used to design the device placement protocol was based on the anatomical considerations outlined in chapter 1. Specifically, attention was given to the selectivity in muscle activation of certain muscles as well as the mechanical coupling characteristics inherent to human anatomy. These anatomical insights were combined with the information obtained from the data from the Hyser dataset discussed in section 3.1, as illustrated in Figure 5.1 , utilizing Power Maps to identify points of maximum activation within the presented setup. This approach allowed for the integration of new information or the validation of anatomical considerations, thereby ensuring a more precise and informed protocol design.

5.1 Apollux positioning

Six Apollux devices were employed to simultaneously record sEMG and ATC signals. The device were numbered from 79 to 84 in order to have a different label for each device. The positioning of the devices was guided by anatomical landmarks and informed by the dataset characteristics previously outlined in chapter 3. The devices were placed on the dominant upper limb of each participant following a standardized placement protocol designed to ensure consistency and accuracy across subjects.

The anatomical reference measurements to be used are the wrist width, taken

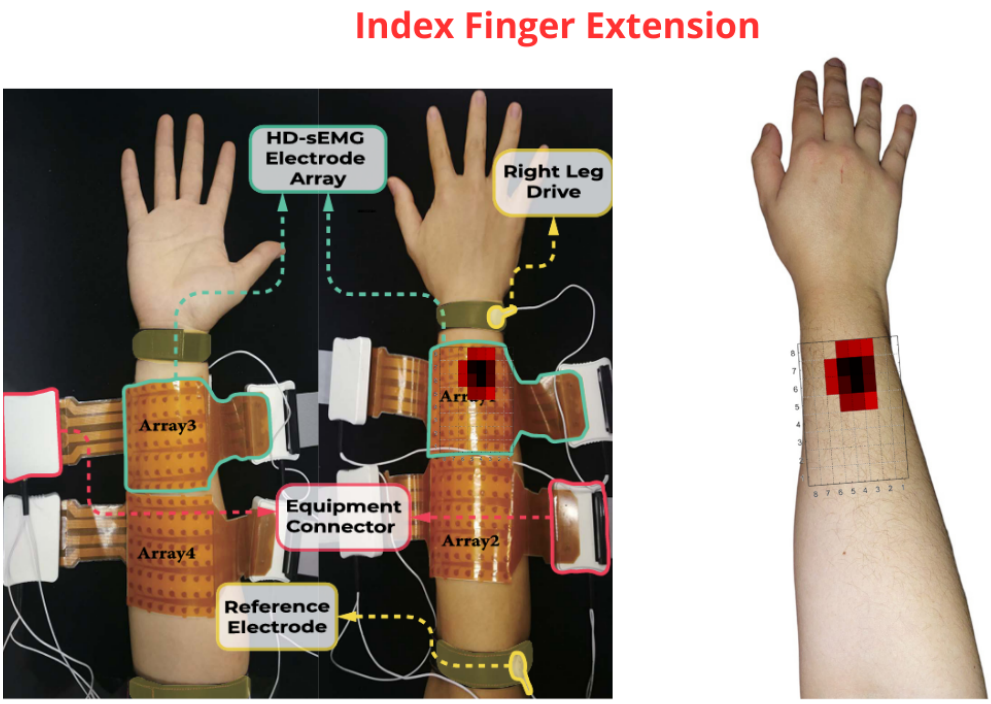

Figure 5.1: Power maps of index finger extension overlaid on the forearm on the left using the figure from [72], and in on the right the arm of the subject used to develop the placement protocol.

using the ulnar styloid process as the anatomical landmark, and the forearm length, which was calculated from the center of the wrist. This approach ensured that each sensor was optimally positioned to capture the most relevant muscle activity, while minimizing variability introduced by anatomical differences among participants. These measurements are taken on the posterior side of the forearm, and the same procedure is repeated on the anterior side.

The first Apollux device, labeled as "Apollux 83", was positioned at 85% of the forearm length, and at this location, the circumference of the arm was measured. The 7.1% of this circumference was then calculated. The device was placed to the right for right-handed subjects or to the left for left-handed subjects, based on this measurement.

This placement, illustrated in Figure 5.2, aimed to selectively measure the activation of the middle, little, and ring fingers, as it was positioned over the most proximal and lateral portion of the extensor digitorum muscle.

Figure 5.2: Apollux 83 placed to target selectively the activation of middle finger, ring finger, and little finger.

The second Apollux device, labeled as "Apollux 82", was placed at 55% of the length of the forearm, centrally aligned. This placement, illustrated in Figure 5.3 aimed to selectively measure the activation of all fingers except the thumb, as it was positioned directly over the extensor digitorum muscle.

This Apollux device is designed to record activity from the same muscle as Apollux 83 but targets a different portion of it. Specifically, it aims to capture the movements associated with the index and middle fingers. While it can still detect the sEMG signals generated by the contraction responsible for the extension of the ring and little fingers, these signals are expected to have lower amplitude.

Figure 5.3: Apollux 82 placed to target selectively the activation of indez finer, middle finger, ring finger, and little finger.

The third and fourth Apollux devices, represented in Figure 5.4, labeled respectively as "Apollux 80" and "Apollux 81", were positioned to record the sEMG signals from the extensor pollicis brevis and extensor indicis, respectively. Both devices were placed at 28.6% of the forearm length. The device targeting the thumb extension was located 1 cm to the left of the midline of the arm, while the device for index finger extension was positioned 1 cm to the right.

Due to their close proximity, these two Apollux devices may not always reliably distinguish between the activation of the thumb and index finger in all subjects.

Figure 5.4: Apollux 80 and 81 placed to target selectively the activation of pollicis brevis and extensor indicis.

The fifth Apollux device, labeled as "Apollux 79", was positioned on the anterior side of the forearm at 35% of its length to record the sEMG signal from the flexor digitorum muscle. It was then shifted by 6% of the arm circumference at that point, toward the left for right-handed subjects and toward the right for left-handed subjects. The positioning is illustrated in Figure 5.5.

This Apollux device was positioned in this location to capture the muscular activation associated with the hand close movement, as it specifically targets the flexor digitorum muscle, which is highly engaged during this action. In some subjects, this channel also exhibited activation during movements where, in addition to finger extension, finger flexion was also present. This response was less frequent, as the signals generated by finger flexion were generally of lower amplitude.

Figure 5.5: Apollux 79 placed to target selectively the activation of the flexor digitorum.

The sixth Apollux device, labeled as "Apollux 84", was placed over the first dorsal interosseous muscle on the hand as illustrated in Figure 5.6.

This Apollux recorded a high-amplitude signal during the hand closure movement, as the first dorsal interosseous muscle exhibits significant activation when contributing to wrist stabilization. This stabilization is particularly crucial during the final phase of hand closure, when the fingers make contact with the palm.

Figure 5.6: Apollux 84 placed to target selectively the activation of the first dorsal interosseous muscle on the hand.

The complete acquisition set-up with the six Apollux devices, each representing a single acquisition channel, is illustrated in Figure 5.7. The Apollux devices are secured to the subject's skin using extensible TNT adhesive patches. Employing a biocompatible adhesive patch enhances both adhesion and durability, which is critical during recording since electrode detachment can compromise the quality of the acquired signals.

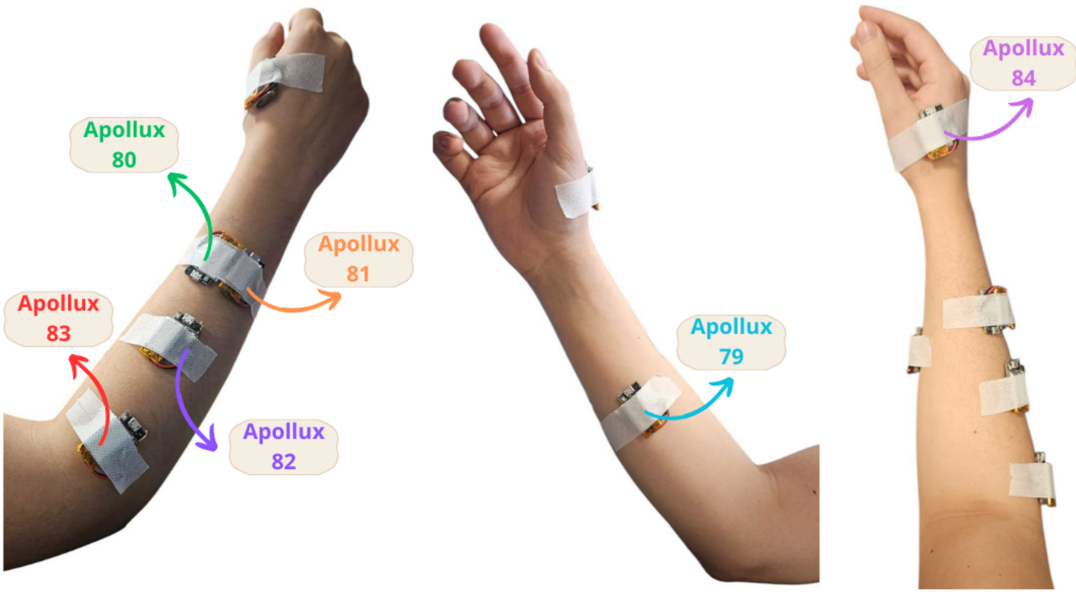

Figure 5.7: View of the complete acquisition set-up. On the left, the rear view; in the middle, the frontal view; and on the right, the lateral view. The identification codes for each Apollux device are also labeled.

5.2 Protocol

The protocol consisted of seven distinct movements and a rest position. The movements included are illustrated in Figure 5.8 :

- Zero
- One thumb
- One index
- Two
- Three
- Four
- Five

Each movement was executed three consecutive times, with a rest interval between repetitions to minimize fatigue. The active phase of each movement was standardized to last 3 seconds, immediately followed by a resting phase of 4 seconds. During the recording process, movements were systematically labeled using numerical values from 0 to 6 corresponding to the predefined gestures, while the resting phase was assigned a value of 7 to distinguish it from active movements.

The participants were told to perform each gesture with the same level of intensity making sure to use consistent force for every repetition. They were also reminded to keep their force steady throughout the gesture to ensure the data recorded was reliable and could be reproduced.

All participants were provided with an explanation of the objectives of the study and the procedure to be carried out. Informed consent was obtained from each participant in written form, in accordance with established ethical guidelines. The confidentiality and anonymity of their personal and recorded data were guaranteed, with all data processed and stored in strict compliance with ethical standards and applicable data protection regulations.

During the positioning of the devices, the Python-based script described in section 4.3 was utilized to evaluate the quality of the acquired sEMG signals, ensuring proper placement and adhesion of the sensors. The positioning phase also served to help the participants as they were able to familiarize themselves with the system and the required movements. During the positioning phase the participants were encouraged to perform the gestures multiple times to self-calibrate their level

Figure 5.8: Movements performed by the subjects during recordings.

of force, thereby enhancing the consistency and repeatability of their movements throughout the experiment.

Once all the Apollux devices were positioned, the recording session began, lasting for a total of 152 seconds. The protocol included an initial 5-second rest phase, followed by 3 seconds dedicated to each gesture, repeated three times per gesture. The resting phase was allocated between consecutive hand gestures to ensure proper separation and recovery, the duration of this phase was 4 seconds.

During the acquisition, participants were instructed to perform each gesture with consistent intensity across the three repetitions. They were also asked to return to the resting position slowly to minimize unintended muscle activations.

The data acquired during these acquisitions adhere to the ethical guidelines established by the Bioethics Committee of the University of Turin [76].

The protocol was performed three times for each subject, ensuring three recordings per subject. Subsequently, recordings were discarded if they were affected by electrode detachment, if they included resting phases with constant activation, or if the subjects performed the wrong movement instead of the intended one.

The sEMG and ATC signals recorded during the protocol were saved in .txt format for each device; then they were transferred to a dedicated directory containing all participants' data, anonymized to ensure confidentiality. The .txt files were then converted into .mat format, making them compatible with MATLAB, the primary environment used for further signal processing, analysis, and classifier development.

Table 5.1: Device and Muscle Targeting

Apollux Device	**Muscle Targeted**
84	First dorsal interosseous of the hand
83	Extensor digitorum (middle finger, ring finger, and little finger)
82	Extensor digitorum
81	Extensor indicis
80	Extensor pollicis brevis
79	Flexor digitorum

Chapter 6

Signals Pre-Processing and Classifier

6.1 Signal processing and features extraction

After the ATC and sEMG signals were acquired a subsequent pre-processing were applied in order to extract the features from the sEMG, these features are described in section 1.8. The raw sEMG signal recorded during a protocol session is illustrated in Figure 6.1.

The signal is first processed using a band-pass filter to isolate the frequency components of interest. Specifically, a high-pass filter with a cut-off frequency of 20 Hz and a low-pass filter with a cutoff frequency of 400 Hz are applied sequentially. Both filters are designed using a 5th-order Butterworth filter, ensuring a smooth frequency response. The effect of the filter is represented in Figure 6.2

The handling of NaN segments within the signal is performed through a combination of linear interpolation and noise augmentation. Initially, the positions of NaN values are identified, and for each segment of consecutive NaN values, the following approaches are adopted:

- For NaN segments at the beginning or end of the signal, the missing values are replaced by the nearest valid value. Specifically, if the NaN segment starts at the first index, it is extended from the first valid value occurring afterward. Conversely, if the NaN segment occurs at the end of the signal, it is filled with the last valid value preceding it.

- For NaN segments located in the middle of the signal, linear interpolation is employed to estimate the missing values. The interpolation is performed using the values surrounding the NaN segment, which are located 130 samples before and after the NaN region. Noise is subsequently added to the interpolated

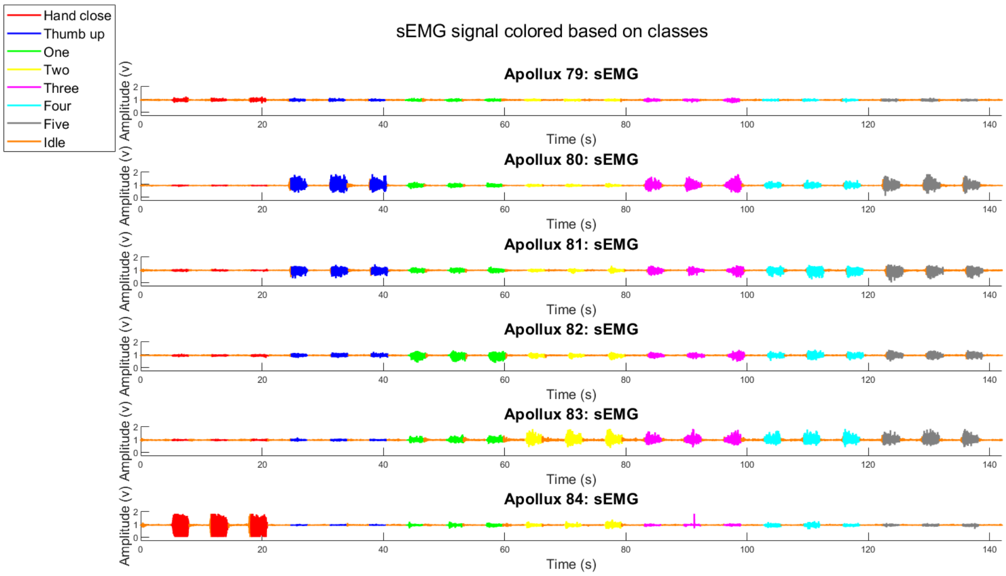

Figure 6.1: Plot of sEMG signals from multiple Apollux devices, with each signal color-coded based on its respective class. The x-axis is synchronized across all subplots, showing the signals up to the shortest signal length, while the y-axis represents the amplitude in volts.

values to make the signal more realistic. The added noise is proportional to the average amplitude of the values in the intervals before and after the NaN segment.

The addition of noise simulates the natural fluctuations of the sEMG, making the interpolation more realistic and avoiding overly smooth or artificial-looking transitions in the signal. An example of interpolation that preserves the natural sEMG behavior is shown in Figure 6.3b.

Subsequently, the features presented in section 1.8 were extracted. A 150 ms observation window was employed for feature extraction, with an overlap of 100 ms between consecutive windows. This parameter was selected based on a preliminary evaluation, as it yielded the highest signal quality and classification performance.

After feature extraction, subject-wise normalization was performed. This type of normalization is performed because subjects have specific physiological characteristics that influence the sEMG signal. Normalization for each subject allows the characteristics not to be distorted and the subject-specific information to be preserved. This step was crucial due to inter-subject variability which is an important factor in physiological signals such as sEMG [77].

This method avoids potential issues due to the global normalization, where

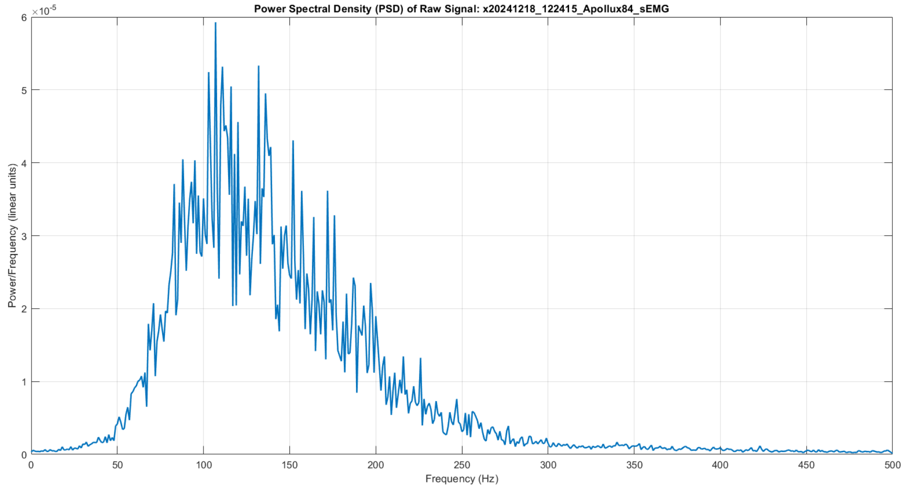

(a) PSD raw sEMG signal.

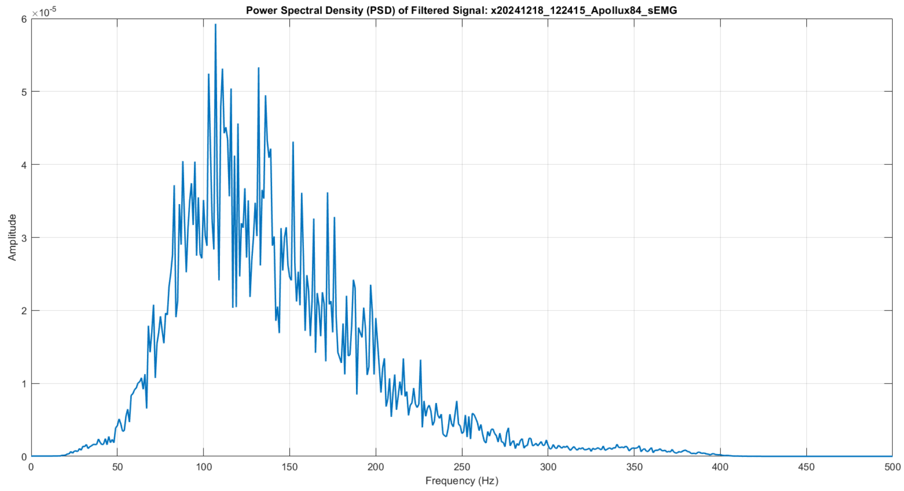

(b) PSD filtered sEMG signal.

Figure 6.2: Comparison between the PSD of the raw signal in (a) and the PSD of the filtered signal shown in (b).

extreme values from certain subjects could dominate the feature distribution. Normalizing the features per subject ensures that the relevant subject-specific information was taken into account, so that the model can generalize more easily and consider the subject specific characteristics.

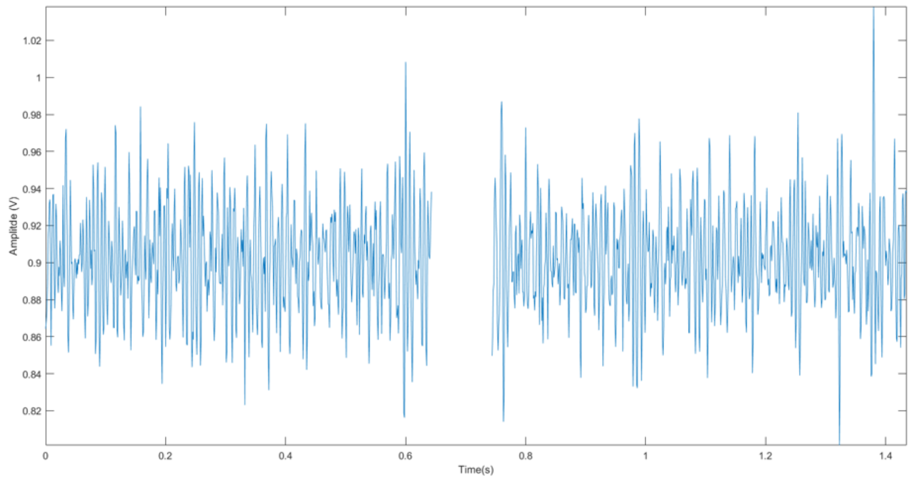

(a) Example of a sEMG signal with NaN values.

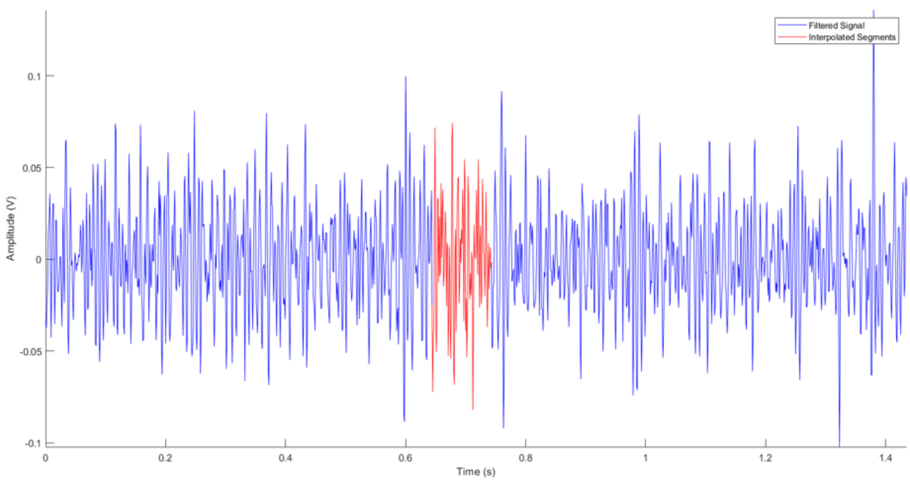

(b) sEMG signal after filtering and interpolation.

Figure 6.3: Comparison of the sEMG befor and after the signal interpolation

6.2 Active threshold and Idle threshold

After the normalization process, the label correction was performed, particularly in instances where the assigned label does not align with the signal activation. This issue is often present in cases where the subject's timing for the start and end of a movement is not accurate, resulting in activation segments being mislabeled as rest or vice versa.

To correct the first scenario, where activation is mislabeled as rest, a threshold-based approach is employed, leveraging a parameter referred to as the *Active Threshold*. Using the slope sign change, identified as the most significant feature during feature extraction, the algorithm examines 25 samples to the left and right of the interval labeled as activation. For each sample in this range, the norm is calculated. If the computed norm exceeds the Active Threshold, the sample is reassigned the label corresponding to the activation interval.

The second scenario involves correcting segments labeled as activation that correspond to rest. For this case, the process is similar but applied across all samples. Specifically, the norm is calculated for each sample, and if the norm falls below a predefined *Idle Threshold*, the sample is reassigned the label of rest.

$$\begin{cases} \text{NormValue} = \sqrt{\sum_{i=1}^{N_{\text{channels}}} Ch_i^2} \\ \text{if NormValue} < \text{IdleThreshold} \quad \text{Class} = 7 \end{cases} \tag{6.1}$$

The example of the threshold correction effect is shown in Figure 6.4.

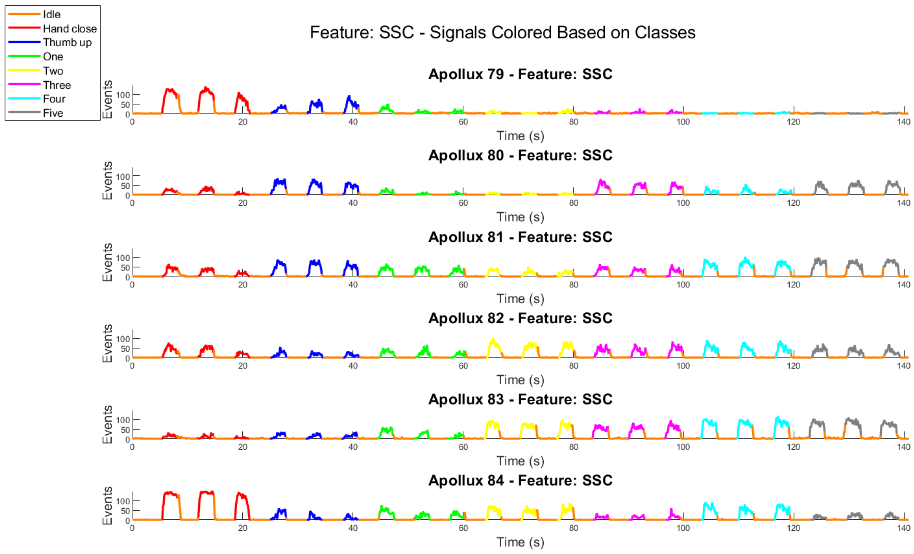

(a) Example of an SSC signal with color-coded labels to distinguish different movements.

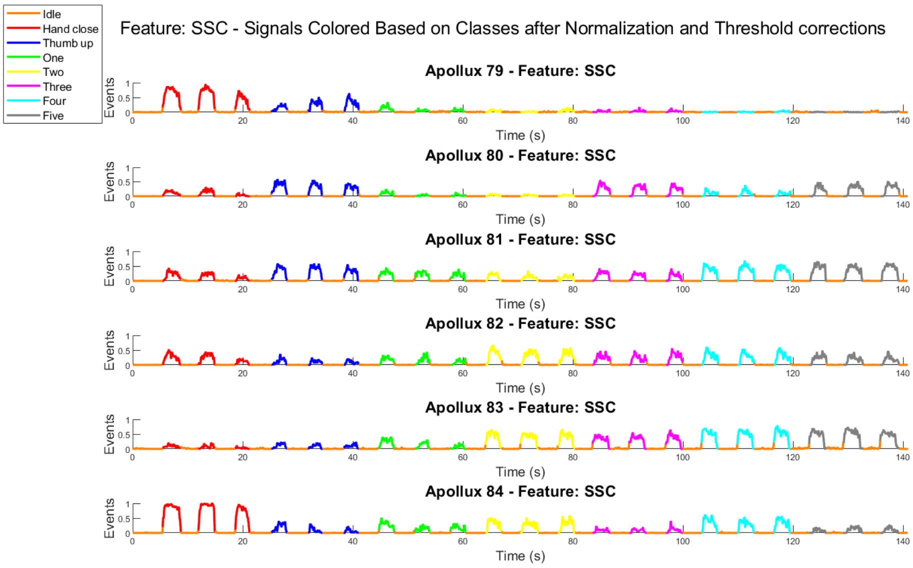

(b) Example of an SSC signal, after normalization and threshold corrections, with color-coded labels to distinguish different movements.

Figure 6.4: (a) Example of an SSC signal with color-coded labels to distinguish different movements. (b) Example of an SSC signal after normalization and threshold corrections, with color-coded labels to distinguish different movements.

6.3 Data concatenation and class balancing

After the data were processed and saved for each patient as described in section 6.1, the features for each subject were concatenated along the columns, with the class column placed last, resulting in a single matrix per subject. These matrices were then concatenated along the rows to create a unified matrix containing all the features and subjects, which was subsequently used to train the classifier.

After obtaining the consolidated matrix, the class distribution was balanced. Balancing the classes is crucial during training to prevent the model from being biased in favor of the majority class. The number of samples from the feature with the fewest samples was taken, and this number was used for all classes by randomly excluding the excess samples.

6.4 Artificial Neural Network Architecture and Training Strategy

The ANN employed in this study is a *fully connected feed-forward network*, trained using the *Adam optimization algorithm*. The input layer consists of N neurons, corresponding to the number of features in the dataset. The network configuration allows for a variable number of hidden layers (L), ranging from two to four, with each layer containing a fixed number of neurons (H) between 10 and 200, as specified in the model parameters. Every hidden layer utilizes a *Rectified Linear Unit (ReLU)* activation function to introduce non-linearity, enhancing the network's ability to capture complex feature relationships.

The final classification stage consists of a *fully connected output layer* with C neurons, where C represents the number of target classes. This is followed by a softmax activation function, which transforms the network's outputs into class probabilities. The classification layer then assigns each input sample to the class with the highest probability.

Training Strategy

To enhance generalization and prevent overfitting, the network is trained using a *k-fold stratified cross-validation* approach, with $k = 5$, ensuring that class distributions are preserved across folds. The training process is repeated twice ($R = 2$) to reduce performance variance.

The optimization process of the neural network employ the *Adam optimizer* and a learning rate of $\alpha = 0.03$. The training of the neural network is then performed using the *mini-batch gradient descent*, where the batch size is calculated as the total number of training samples divided by 100, ensuring adaptability to different dataset sizes while maintaining stability.

To further improve training efficiency, a *piecewise learning rate schedule* is implemented, adjusting the learning rate dynamically based on performance. Additionally, *early stopping* is applied, where training halts if no improvement in validation loss is observed for five consecutive epochs. The model was trained for a maximum of 1000 epochs.

During training, the target labels are converted into categorical format, ensuring compatibility with the classification framework. Inference is performed on test data using the same mini-batch size as in training, maintaining consistency across evaluation phases. Once trained, the final ANN model is stored for subsequent analysis and deployment.

6.5 Summary of Model Hyperparameters

In this section is provided a structured summary of the neural network hyperparameters, which were previously discussed in detail. These parameters define the network architecture and training process, influencing its learning dynamics and performance.

- **Hidden layers (L)**: 2 to 4
- **Neurons per layer (H)**: 10 to 200
- **Activation functions**:
  - Hidden layers: **ReLU**
  - Output layer: **Softmax**
- **Cross-validation**: k-fold stratified, with $k = 5$
- **Training repetitions**: $R = 2$
- **Optimizer**: Adam
- **Learning rate (α)**: 0.03
- **Mini-batch size**: total training samples / 100
- **Early stopping**: Yes, patience = 5 epochs
- **Maximum epochs**: 1000

Chapter 7

Results and Discussions

7.1 Metrics

In machine learning and classification tasks, model performance is typically assessed using standard metrics such as Accuracy, Precision, Recall, and F1-score.

Accuracy measures the proportion of correctly classified instances relative to the total number of samples, providing a general indication of model performance. The formula is given by:

$$Accuracy = \frac{TP + TN}{TP + TN + FP + FN} \tag{7.1}$$

- TP = Number of true positives (correctly predicted positive instances)
- TN = Number of true negatives (correctly predicted negative instances)
- FP = Number of false positives (incorrectly predicted positive instances)
- FN = Number of false negatives (incorrectly predicted negative instances)

However, when dealing with imbalanced datasets, Accuracy alone may not be sufficiently informative.

Precision quantifies the proportion of instances predicted as positive that are indeed positive, reflecting the reliability of the model's positive predictions. Its mathematical representation is:

$$Precision = \frac{TP}{TP + FP} \tag{7.2}$$

The *Recall* measures the model's ability to correctly identify all actual positive instances, making it particularly critical in contexts where minimizing false negatives is essential:

$$Recall = \frac{TP}{TP + FN} \tag{7.3}$$

Finally, the F1-score represents the harmonic mean of Precision and Recall, offering a balanced measure that considers both metrics simultaneously:

$$F1\text{-}score = 2 \times \frac{Precision \times Recall}{Precision + Recall} \tag{7.4}$$

This metric is especially useful when a balance between Precision and Recall is required to evaluate overall classification performance effectively.

In addition, *per-class accuracy* provides further insight by evaluating the accuracy for each class individually. For each class, the per-class accuracy is computed by considering that class as positive and all others as negative, using the same formula as for the Accuracy:

$$\text{Per-class Accuracy} = \frac{TP + TN}{TP + TN + FP + FN} \tag{7.5}$$

- TP = Number of true positives (instances correctly classified as belonging to the class).
- TN = Number of true negatives (instances correctly classified as not belonging to the class).
- FP = Number of false positives (instances incorrectly classified as belonging to the class).
- FN = Number of false negatives (instances of the class incorrectly classified as not belonging to it).

7.2 Features selection

After compiling the dataset of all subjects, feature selection was performed. To determine the number of features to select, PCA was conducted based on explained variance, which represents the proportion of the dataset's total variance captured by each principal component. The number of principal components was determined by selecting those that contributed to a cumulative explained variance above the set threshold of 95%. The contribution of each feature to the selected principal components was then quantified by summing the absolute values of its corresponding PCA loadings. As reported in Figure 7.1 the number of principal component needed to exceed the threshold was 10, the subsequent training phases were conducted considering these features.

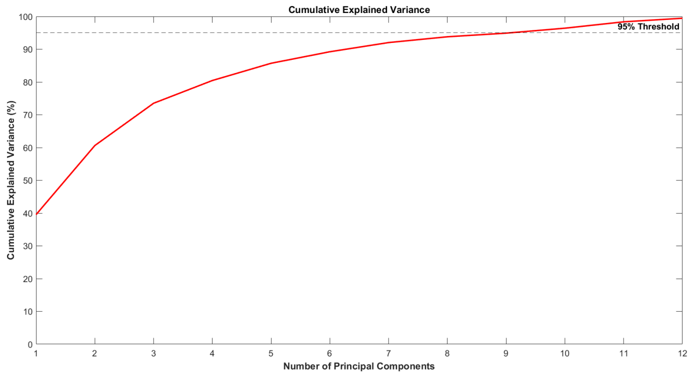

Figure 7.1: Explained variance analysis of the dataset's features using PCA. It represents the cumulative explained variance, showing the total variance retained as more components are included. The black dashed line indicates the 95% variance threshold, which determines the minimum number of principal components required to retain most of the dataset's information.

To evaluate the relevance of each selected feature, the sum of the absolute contributions of each feature across the first selected principal components was computed. The most relevant feature, based on its overall contribution to the principal components, was the SSC as illustrated in Figure 7.2:

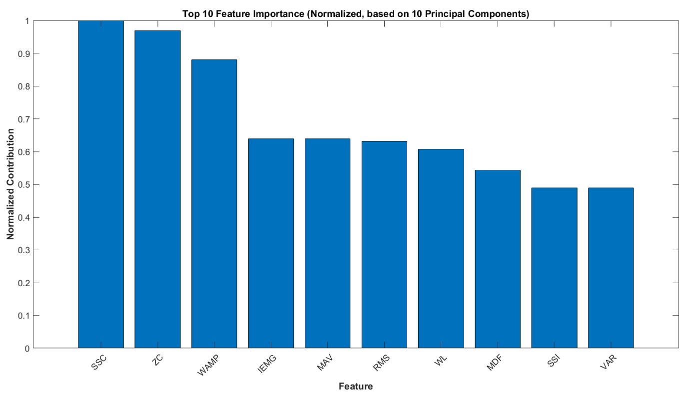

Figure 7.2: Bar plot representing the importance of the top 10 features based on their contribution to the selected principal components. The ranking is determined by summing the absolute values of the PCA loadings for the principal components that cumulatively explain at least 95% of the variance. Features with higher importance values have a stronger influence on the transformed feature space.

7.3 Classification results

The results presented in this section were obtained from 3 subjects, using a training dataset consisting of 23 subjects. The results showed high accuracy for the movements *Hand close*, *Thumb up*, *Two*, and *Idle*. Lower accuracy was observed for the movements *Three*, *Four*, and *Five*. This discrepancy can be attributed to the similarity in muscle activation patterns between these specific movements. The protocol was designed with the assumption that, although the same muscles are involved in both movements, the *Five* gesture would elicit a higher activation of the extensor digitorum, leading to increased signal intensity in channels 83 and 82. However, this pattern was not consistently observed across all subjects. In individuals with stronger and more distinct muscle activation, the signals corresponding to *Three* and *Five* were nearly identical as it is represented in Figure 7.3.

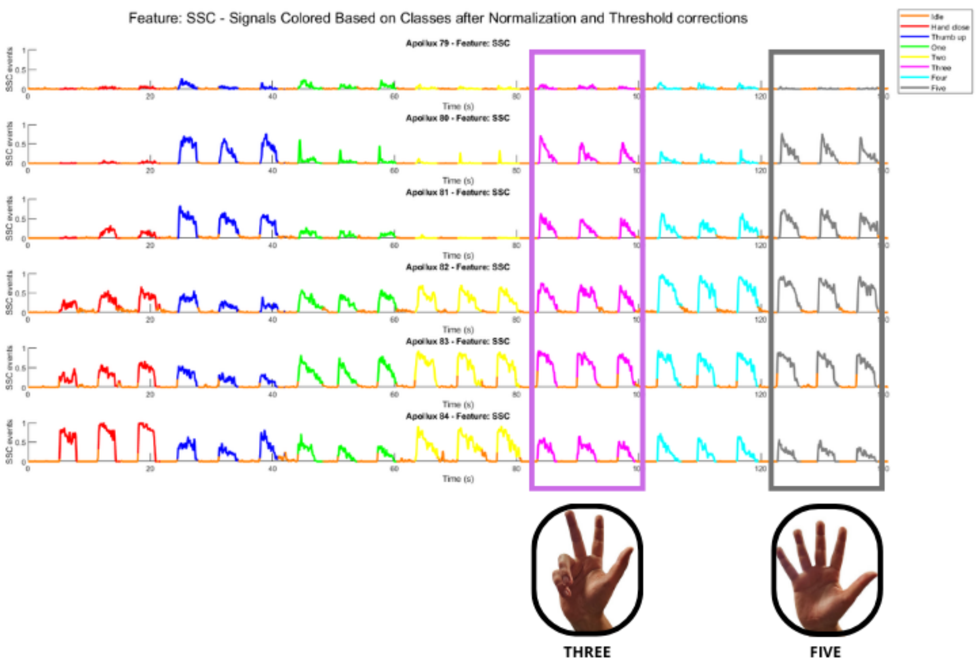

Figure 7.3: SSC normalized signal showing a clear similarity in activations between the *Three* and *Five* movements across all six channels.

This behavior was predominantly observed in subjects with smaller forearm circumferences, where the signal was detected accurately, but the smaller forearm size led to less selective signal acquisition due to the fixed electrode placement.

o further investigate this aspect, an additional classification test was performed by removing both the *Five* and *Four* movements, which exhibited the poorest performance. This allowed for an assessment of their combined impact on classification performance.

7.3.1 Classifier performance all movements

The optimal neural network architecture consisted of 4 hidden layers with 200 neurons, delivering the best performance. As represented in Figure 7.4, the results were quite promising, showing excellent classification for most movements. The ones with the worst performance are the *Five* and *Four* movements, which, as previously described, are more problematic for classification.

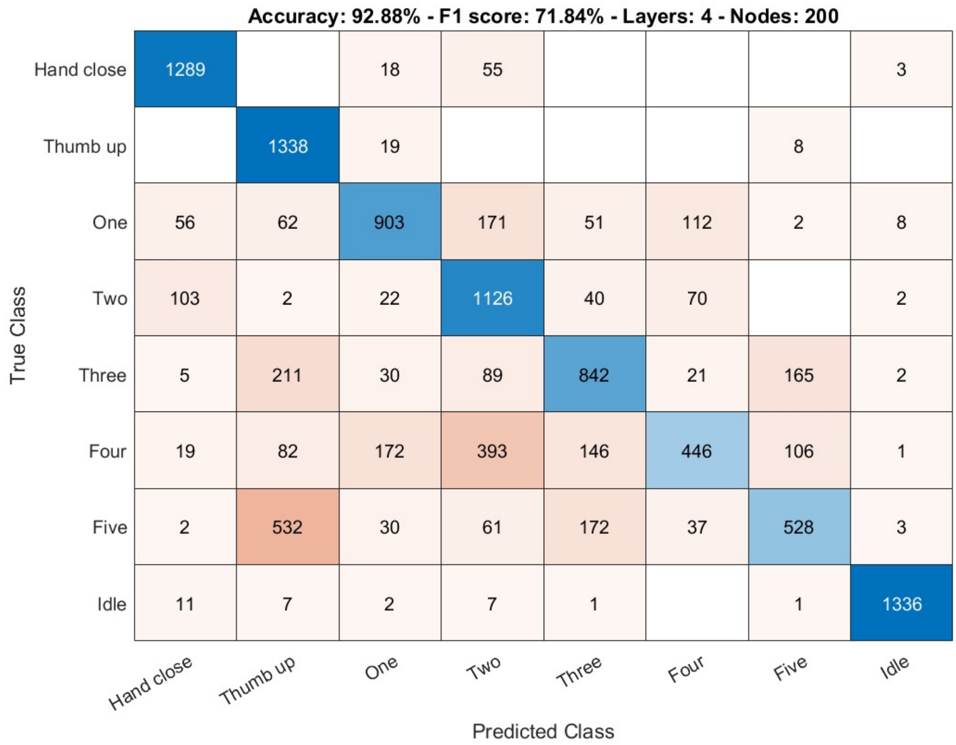

Figure 7.4: Confusion matrix for the finger movement classifier considering all the movements. The matrix shows the correspondence between true and predicted classes. Each row represents the actual class, while each column indicates the predicted class. The diagonal elements contain the correctly classified instances, while off-diagonal elements represent misclassifications. Darker blue cells indicate higher values, while lighter shades highlight lower occurrences.

The classification results demonstrated strong average performance, with particularly high accuracy for the majority of the movements. The model excels

Table 7.1: Classification performance metrics per movement

Movement	**Accuracy (%)**	**Precision (%)**	**Recall (%)**	**F1 Score (%)**
Hand close	98.11	92.39	92.53	92.46
Thumb up	89.84	55.81	90.11	68.93
One	92.70	74.19	63.81	68.61
Two	91.12	60.60	82.71	69.95
Three	91.58	68.28	61.03	64.45
Four	88.15	54.11	34.21	41.92
Five	88.17	54.33	33.55	41.49
Idle	99.51	97.33	98.83	98.07
Average	**92.88**	**72.18**	**71.50**	**71.84**

in recognizing the *Hand close* and *Idle* state, achieving near-perfect accuracy of 98.11% for *Hand close* and 99.51% for *Idle*, along with consistently high precision and recall values. Additionally, movements such as *Thumb up* and *Two* exhibit solid recall scores of 90.11% and 82.71%, highlighting the classifier's ability to correctly identify these gestures.

However, the classification of *Four* and *Five* movements shows lower performance compared to the others. The relatively low recall rates of 34.21% for *Four* and 33.55% for *Five* suggest that these movements are often misclassified.

Despite these limitations, the average F1 score confirm a well-balanced classification performance across most gestures, reinforcing the system's suitability for practical applications.

The misclassification results are due to inter-subject variability, as the movements between subjects are not always similar. Sometimes, a movement from one subject can exhibit the same activation pattern as a different movement from another subject as will be described later in section 7.5.

7.3.2 Classifier subset of movements evaluation

The architecture for the neural network featured 4 hidden layers, with 190 neurons per layer. As stated before, to verify that the classification is done correctly and that the issue lies in the high similarity of activation patterns between different movements for the same subject, a classifier was trained by removing the *Four* and *Four* movements from the initial set of movements. By removing these movements, the performance improves as represented in Figure 7.5, particularly noticeable in the F1 score, which increases from 71.84% to 86.86%, highlighting a significant improvement in classification.

Notably, the movements *Hand close* and *Thumb up* exhibit the highest F1 score values, indicating a strong ability to correctly identify these gestures, while the *Idle* class maintains the highest average classification performance.

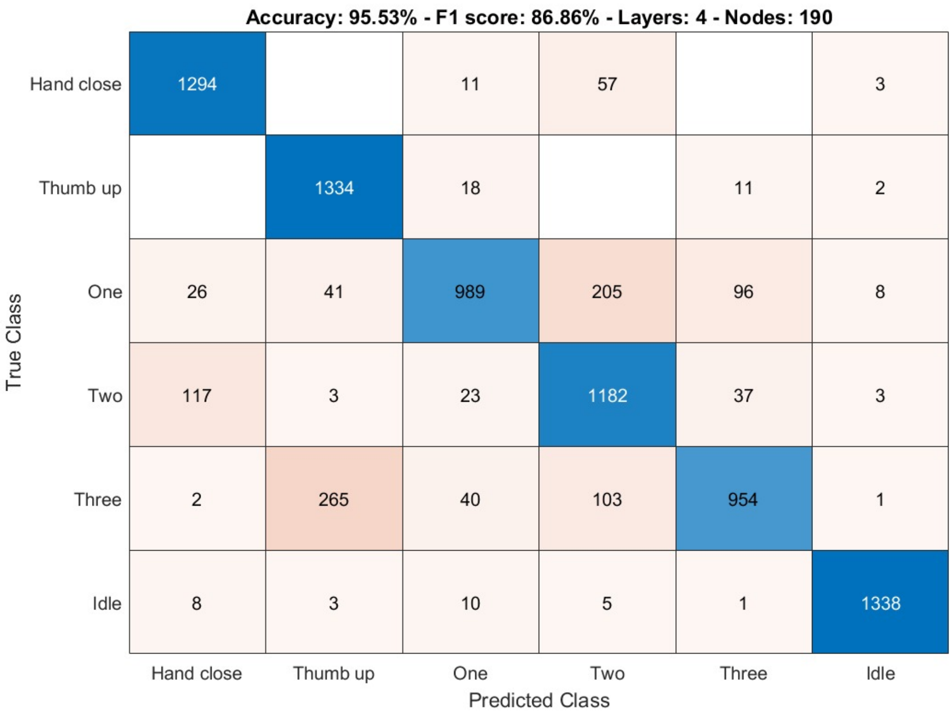

Figure 7.5: Confusion matrix for the finger movement classifier discarding the two most challenging movements. The matrix shows the correspondence between true and predicted classes. Each row represents the actual class, while each column indicates the predicted class. The diagonal elements contain the correctly classified instances, while off-diagonal elements represent misclassifications. Darker blue cells indicate higher values, while lighter shades highlight lower occurrences.

Table 7.2: Classification Performance Excluding Movements *Four-Five*.

Movement	**Accuracy (%)**	**Precision (%)**	**Recall (%)**	**F1 Score (%)**
Hand close	97.26	89.43	94.80	92.03
Thumb up	95.81	81.04	97.73	88.61
One	94.16	90.65	72.45	80.54
Two	93.25	76.16	86.59	81.04
Three	93.21	86.81	69.89	77.44
Idle	99.46	98.75	98.02	98.38
Average	**95.53**	**87.14**	**86.58**	**86.86**

7.4 Single subject classifier evaluation

To evaluate the network's classification ability, it was trained using data from a single subject, focusing on its capacity for accurate classification rather than generalization. A key aspect of this evaluation was that the recordings were conducted on two different days, as a robust classifier must reliably classify data even when faced with varying noise levels, changes in the subject's physiological state, and different sensor placements. Three repetitions of the acquisition protocol were used for the training phase, and the same number of repetitions was used for the testing phase.

7.4.1 Performance evaluation considering all movements

Using a dataset that includes all seven movements and the idle state, the ANN was trained following the method described in chapter 5. The best-performing architecture consists of 3 hidden layers with 160 nodes.

The classifier demonstrated excellent performance on the *Hand Close* movement, with both accuracy and F1 score reaching 100%. The *Thumb Up* movement also achieved high results, with an accuracy of 99.02% and an F1 score of 96.01%. As illustrated in Figure 7.6 Movements such as *One*, *Two*, and *Four* displayed strong performance with accuracy ranging from 96.64% to 98.29%, and corresponding F1 score varying from 81.74% to 93.20%. However, the classifier struggled more with *Three* and *Five*, achieving lower accuracy rates of 92.34% and 93.63%, respectively, and F1 score of 66.59% and 74.85%.

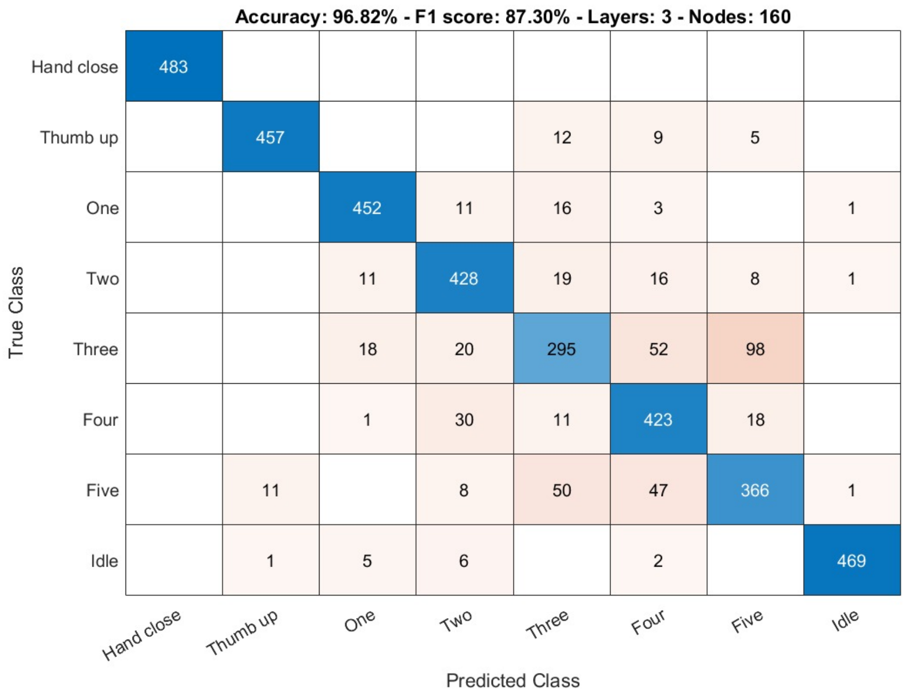

Figure 7.6: Confusion matrix for the finger movement classifier across all movements. Diagonal elements represent correct classifications, while off-diagonal ones indicate misclassifications.

Table 7.3: Classification Performance Single Subject.

Movement	**Accuracy (%)**	**Precision (%)**	**Recall (%)**	**F1 Score (%)**
Hand close	100.00	100.00	100.00	100.00
Thumb up	99.02	97.44	94.62	96.01
One	98.29	92.81	93.58	93.20
Two	96.64	85.09	88.61	86.82
Three	92.34	73.20	61.08	66.59
Four	95.11	76.63	87.58	81.74
Five	93.63	73.94	75.78	74.85
Idle	99.56	99.36	97.10	98.22
Average	**96.82**	**87.31**	**87.29**	**87.30**

7.4.2 Single subject classifier subset of movements evaluation

The optimal neural network architecture was based on 4 hidden layers, each having 150 neurons. For movements like *One* and *Two*, as represented in Figure 7.7, the classifier demonstrated very high performance, with accuracy values of 97.31% and 97.96%, and F1 scores of 91.99% and 94.05%, respectively.

The *Three* gesture, while still showing strong performance, presented a slightly more challenging classification, achieving an accuracy of 96.93% and an F1 score of 90.54%. Nevertheless, the classifier excelled in recognizing the *Idle* state, with an accuracy of 99.45% and an F1 score of 98.32%, further emphasizing the robustness of the model in handling both finger movements and the idle condition. These results indicate that the classifier can achieve remarkably high performance.

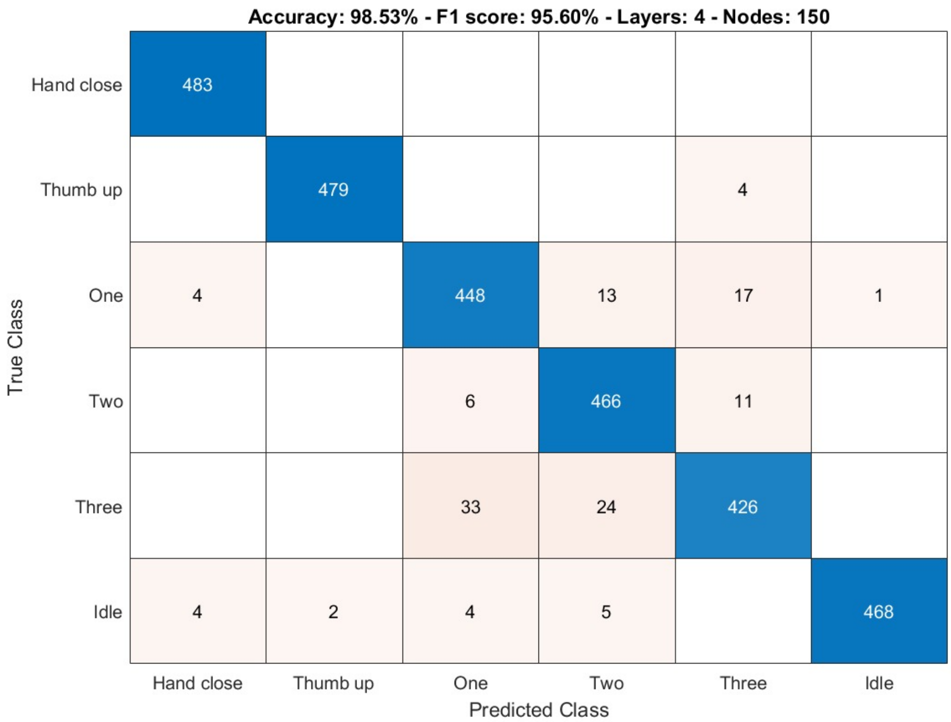

Figure 7.7: Confusion matrix for the finger movement classifier after removing the two most challenging movements. Diagonal elements represent correct classifications, while off-diagonal ones indicate misclassifications.

Table 7.4: Classification Performance Single Subject, Excluding Movements *Four-Five*.

Movement	Accuracy (%)	Precision (%)	Recall (%)	F1 Score (%)
Hand close	99.72	98.37	100.00	99.18
Thumb up	99.79	99.58	99.17	99.38
One	97.31	91.24	92.75	91.99
Two	97.96	91.73	96.48	94.05
Three	96.93	93.01	88.20	90.54
Idle	99.45	99.79	96.89	98.32
Average	**98.53**	**95.62**	**95.58**	**95.60**

7.5 Analysis of Signals for Inter-Subject Differences

As shown in Figure 7.8, the SSC signal profiles are remarkably similar between the two subjects for two different movements: specifically, the *One* movement of the subject 24, depicted in Figure 7.8a, and the *Five* movement of the subject 25. In general, it can be observed that activation patterns vary significantly, not only are there highly similar activations for different movements, but also substantial differences for the same movements. For instance, the *Thumb up* movement in the subject 24 exhibits a clear activation in the acquisition channel corresponding to Apollux 79, whereas no activation is present for the subject 25.

These evident differences in activation patterns highlight the considerable inter-subject variability. Although the acquisition devices were positioned according to an anatomically guided protocol, muscle activations can still vary, making classification more challenging. This issue can be mitigated by increasing the number of subjects in the training dataset, thereby exposing the model to a wider range of activation patterns and improving its generalization capabilities.

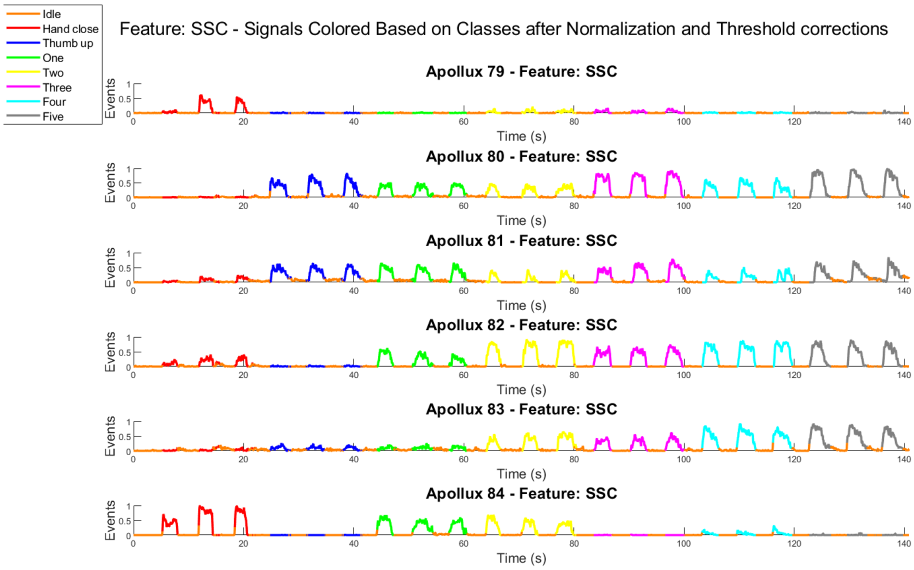

(a) SSC signal of subject 24.

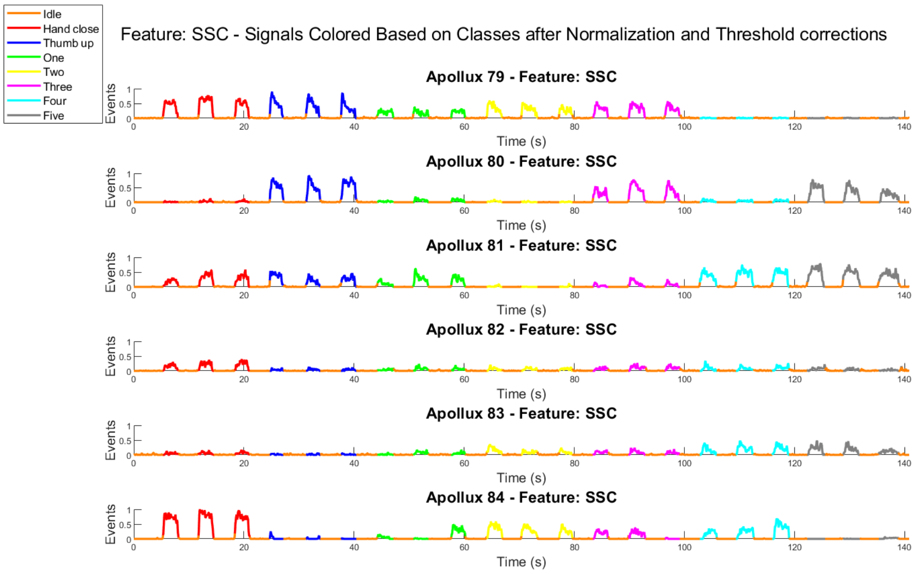

(b) SSC signal of subject 25.

Figure 7.8: SSC signal of subject 24 and subject 25. Each subplot represents a single acquisition channel. The samples are labeled to highlight the activation zones, with a color code assigned to each movement. The x-axis represents time, while the y-axis shows the normalized SSC events.

7.6 ATC and multi-features classification comparison

A comparison between the method utilizing a multi-feature classification approach and the classifier based solely on the ATC signal, as employed in previous studies by the research group, reveals notable differences in performance.

The classifier built using only the ATC signal achieved optimal performance with a neural network architecture consisting of four hidden layers, each containing 140 neurons.

It is observed that the ATC-based classification exhibits inferior performance; however, both approaches consistently show the poorest results for the *Four* and *Five* movements, as it is shown in Figure 7.9.

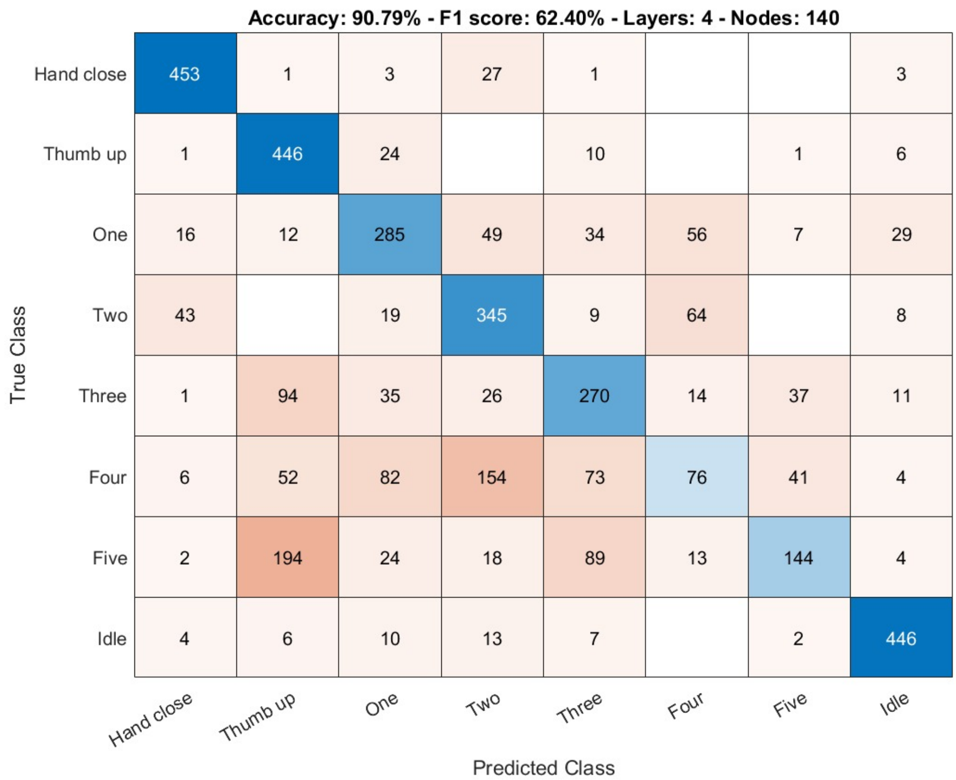

Figure 7.9: Confusion matrix of the ATC signal testing phase.

Table 7.5: Classification Performance Using ATC signals.

Movement	Accuracy (%)	Precision (%)	Recall (%)	F1 Score (%)
Hand close	97.23	86.12	92.83	89.35
Thumb up	89.73	55.40	91.39	68.99
One	89.75	59.13	58.40	58.76
Two	88.99	54.59	70.70	61.61
Three	88.70	54.77	55.33	55.05
Four	85.68	34.08	15.57	21.38
Five	88.93	62.07	29.51	40.00
Idle	97.26	87.28	91.39	89.29
Average	**89.92**	**61.68**	**63.14**	**62.40**

7.6.1 ATC subset movements performance

Eliminating the movements *Four* and *Five*, as previously described in subsection 7.3.2, results in a significant improvement in performance for both cases. Specifically, for ATC signals-based classification, the accuracy, as shown in Table 7.6, increases from 89.92% to 93.95%, and the F1 score improves from 62.40% to 81.86%.

This demonstrates that, although the classifier based on ATC signals achieves good performance, the incorporation of a multi-feature approach yields superior results by providing the classifier with a more comprehensive set of information.

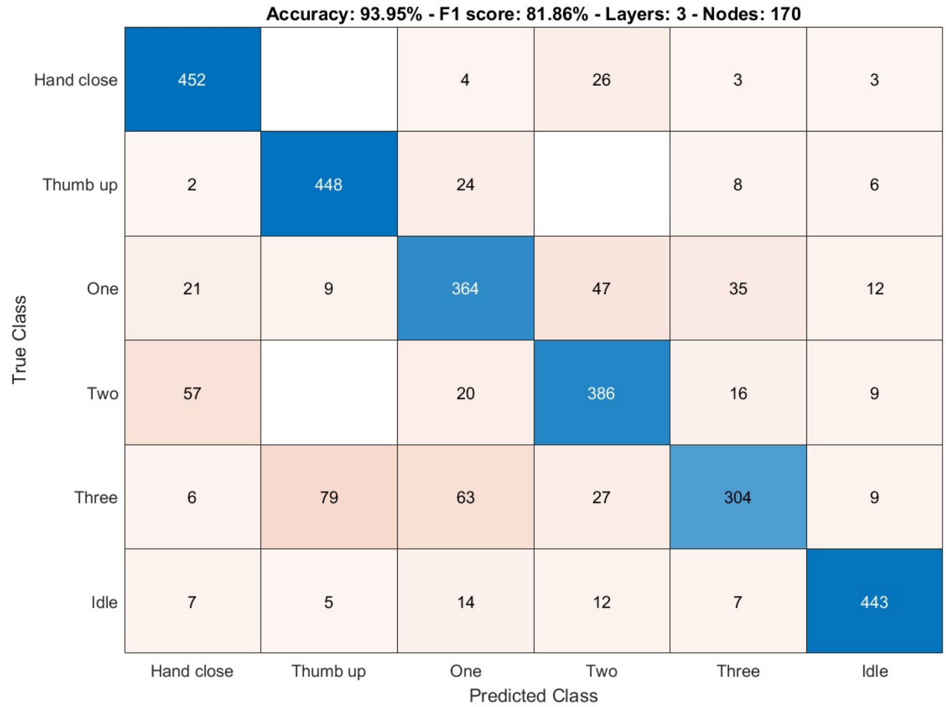

Figure 7.10: Confusion matrix of the ATC signal testing phase removing *Four* and *Five*.

Table 7.6: Classification Performance Using ATC signals without *Four* and *Five*.

Movement	**Accuracy (%)**	**Precision (%)**	**Recall (%)**	**F1 Score (%)**
Hand close	95.59	82.94	92.62	87.51
Thumb up	95.46	82.81	91.80	87.07
One	91.50	74.44	74.59	74.51
Two	92.69	77.51	79.10	78.30
Three	91.36	81.50	62.30	70.62
Idle	97.13	91.91	90.78	91.34
Average	**93.95**	**81.85**	**81.86**	**81.86**

Chapter 8

Conclusion and Future Developments

The thesis project proposed a wearable system and a setup designed to develop a classifier for finger movement recognition using sEMG signals, acquired from both intrinsic and extrinsic muscles. The system builds upon a previous prototype developed by the research team, incorporating its ANN-based classifier.

The acquisition system introduces a novel structure that enables the simultaneous recording of multiple modalities, including RMS, ATC, sEMG, and TC. This modification allows real-time extraction of different signals within the same recording session, providing the user with a broader dataset and greater flexibility for analysis.

Software improvements also included enhancements to the GUI, facilitating user interaction with the acquisition system. Additionally, a second GUI was developed to guide the subject during the recording process, thereby improving the quality of the acquired data.

To enhance signal quality, essential preprocessing steps were performed, including interpolation of NaN values, which can be lost during acquisition due to temporary disconnections between the Apollux device and the BLE dongle. Furthermore, a key processing step involved refining the labeling of the acquired signals, accounting for potential human errors. By correcting the labels associated with muscle activations, an optimized labeling process was achieved, significantly improving classification performance.

This was highlighted through the trial in which a classifier was built using a single subject, demonstrating that classification with this setup is optimal. Furthermore, it confirms that the electrode positioning protocol, designed to selectively target muscles so that they activate with a specific pattern for each movement, was effectively implemented.

The developed classifier demonstrates excellent performance. Moreover, it has been shown that the multi-feature approach achieves higher performance compared to the use of the ATC signal alone, as it provides a broader spectrum of information for classification.

However, classification challenges were observed for certain movements, primarily due to the well-known inter-subject variability in muscle activation patterns for hand movements. This issue is further emphasized by the limited number of subjects in the dataset. As noted in [78], having a sufficiently large dataset is crucial for improving the model's ability to generalize effectively.

The acquisition setup could be reconsidered, particularly the channels 80-81, which are very close to each other and therefore prone to cross-talk, especially in subjects with a thinner forearm. In this case, the activation signals of the extensor indicis and extensor pollicis brevis are recorded without being able to discriminate between them, which undermines the initial hypothesis of achieving selective muscle placement.

The classifier has been evaluated only in an offline setting. Future developments include implementing real-time prediction, enabling sample-by-sample movement classification.

In a real-time implementation, an initial calibration phase is required, during which the subject performs the target movements while relevant features are extracted. These features are used to compute the maximum and minimum values, which are subsequently employed for signal normalization. This approach ensures subject-specific normalization, preventing excessive distortion that could arise from a global normalization strategy. Specifically, a global approach could lead to an undesired flattening effect, where subjects with higher activation levels disproportionately influence the normalization of others. Once real-time classification is integrated, the complete development of the Two-Subject Stimulation system can be pursued.

Bibliography

[1] Henry Chim. *Hand and Wrist Anatomy and Biomechanics: A Comprehensive Guide*. Thieme Medical Publishers, 2017 (cit. on pp. 1, 13).

[2] Karen L. LaBat and Karen S. Ryan. *Designing for Hand and Wrist Anatomy*. 1st. CRC Press, 2019, pp. 335–377. ISBN: 9780429055690 (cit. on pp. 1, 5, 14, 15).

[3] TeachMeAnatomy.info. *Muscles of the Hand*. Accessed: March 10, 2025. 2024. URL: `https://teachmeanatomy.info/upper-limb/muscles/hand/` (cit. on pp. 3, 4).

[4] S. Gupta and H. Michelsen-Jost. «Anatomy and function of the thenar muscles». In: *Hand Clinics* 28.1 (Feb. 2012), pp. 1–7. DOI: `10.1016/j.hcl.2011.09.006` (cit. on p. 3).

[5] E. Okwumabua, M. A. Sinkler, and B. Bordoni. *Anatomy, Shoulder and Upper Limb, Hand Muscles*. Accessed: March 10, 2025. Treasure Island (FL): StatPearls Publishing, July 2023. URL: `https://www.ncbi.nlm.nih.gov/books/NBK537229/` (cit. on pp. 3, 6).

[6] J.A. Pasquella and P. Levine. «Anatomy and function of the hypothenar muscles». In: *Hand Clinics* 28.1 (Feb. 2012), pp. 19–25. DOI: `10.1016/j.hcl.2011.09.003` (cit. on p. 4).

[7] Basic Medical Key. *Anterior Forearm*. Accessed: March 10, 2025. 2024. URL: `https://basicmedicalkey.com/anterior-forearm/` (cit. on p. 5).

[8] Brett Mitchell and Leah Whited. *Anatomy, Shoulder and Upper Limb, Forearm Muscles*. [Updated 2023 Jun 5]. StatPearls Publishing. Treasure Island (FL), Jan. 2024. URL: `https://www.ncbi.nlm.nih.gov/books/NBK536975/` (cit. on pp. 5, 6).

[9] Basic Medical Key. *Posterior Forearm*. Accessed: March 10, 2025. 2024. URL: `https://basicmedicalkey.com/posterior-forearm/` (cit. on p. 7).

[10] Sean Yiu, Vernon Farewell, and Brian Tom. «Clustered Multistate Models with Observation Level Random Effects, Mover–Stayer Effects and Dynamic Covariates: Modelling Transition Intensities and Sojourn Times in a Study of Psoriatic Arthritis». In: *Journal of the Royal Statistical Society: Series C (Applied Statistics)* 67 (Apr. 2017). DOI: `10.1111/rssc.12235` (cit. on p. 8).

[11] Wikipedia contributors. *Carpal bones*. Accessed: March 10, 2025. URL: `https://en.wikipedia.org/wiki/Carpal_bones` (cit. on p. 11).

[12] Łukasz Jaworski and Robert Karpiński. «BIOMECHANICS OF THE HUMAN HAND». In: *Journal of Technology and Exploitation in Mechanical Engineering* 3 (June 2017), pp. 28–33. DOI: `10.35784/jteme.536` (cit. on p. 14).

[13] Irene Campanini, Andrea Merlo, Cathrin Disselhorst-Klug, Luca Mesin, Silvia Muceli, and Roberto Merletti. «Fundamental Concepts of Bipolar and High-Density Surface EMG Understanding and Teaching for Clinical, Occupational, and Sport Applications: Origin, Detection, and Main Errors». In: *Sensors (Basel)* 22.11 (May 2022), p. 4150. DOI: `10.3390/s22114150` (cit. on pp. 15–18, 20, 21).

[14] Kemal S Türker. «Electromyography: Some Methodological Problems and Issues». In: *Physical Therapy* 73.10 (Oct. 1993), pp. 698–710. ISSN: 0031-9023. DOI: `10.1093/ptj/73.10.698`. eprint: `https://academic.oup.com/ptj/article-pdf/73/10/698/10760206/ptj0698.pdf`. URL: `https://doi.org/10.1093/ptj/73.10.698` (cit. on pp. 15, 17).

[15] Nebras Hussein. «Simulation Study for Electrocardiography Contamination in Surface Electromyography». In: *2008 Cairo International Biomedical Engineering Conference, CIBEC 2008* (Dec. 2008). DOI: `10.1109/CIBEC.2008.4786097` (cit. on p. 16).

[16] Alper Cömert, Markku Honkala, and Jari Hyttinen. «Effect of pressure and padding on motion artifact of textile electrodes». In: *Biomedical engineering online* 12 (Apr. 2013), p. 26. DOI: `10.1186/1475-925X-12-26` (cit. on p. 17).

[17] Brandon B. Murphy, Benjamin H. Scheid, Quinn Hendricks, Nicholas V. Apollo, Brian Litt, and Fabio Vitale. «Time Evolution of the Skin-Electrode Interface Impedance under Different Skin Treatments». In: *Sensors (Basel)* 21.15 (July 2021), p. 5210. DOI: `10.3390/s21155210` (cit. on p. 17).

[18] Alberto Lozano, Javier Rosell, and Ramon Pallás-Areny. «Errors in Prolonged Electrical Impedance Measurements Due to Electrode Repositioning and Postural Changes». In: *Physiological Measurement* 16.2 (May 1995), pp. 121–130. DOI: `10.1088/0967-3334/16/2/004` (cit. on p. 18).

[19] Hermie J Hermens, Bart Freriks, Catherine Disselhorst-Klug, and Günter Rau. «Development of recommendations for SEMG sensors and sensor placement procedures». In: *Journal of Electromyography and Kinesiology* 10.5 (2000), pp. 361–374. ISSN: 1050-6411. DOI: https://doi.org/10.1016/S1050-6411(00)00027-4. URL: https://www.sciencedirect.com/science/article/pii/S1050641100000274 (cit. on p. 18).

[20] Martina Ladrova, Radek Martinek, Jan Nedoma, and Marcel Fajkus. «Methods of Power Line Interference Elimination in EMG Signal». In: *Journal of Biomimetics, Biomaterials and Biomedical Engineering* 40 (Mar. 2019), pp. 64–70. DOI: 10.4028/www.scientific.net/JBBBE.40.64 (cit. on p. 19).

[21] Aaron J. Beverwyk, Kenneth Mancuso, Amit Prabhakar, Jonathan Lissauer, Alan David Kaye, and Scott Francis Davis. «Electromyography (EMG)». In: *Principles of Neurophysiological Assessment, Mapping, and Monitoring*. Ed. by Scott Francis Davis and Alan David Kaye. Cham: Springer International Publishing, 2020, pp. 135–145. ISBN: 978-3-030-22400-4. DOI: 10.1007/978-3-030-22400-4_8. URL: https://doi.org/10.1007/978-3-030-22400-4_8 (cit. on p. 19).

[22] SlideServe. *Structure of Skeletal Muscle*. Accessed: March 10, 2025. URL: https://www.slideserve.com/ananda/structure-of-skeletal-muscle (cit. on p. 27).

[23] Brian R. MacIntosh, Phillip F. Gardiner, and Alan J. McComas. *Skeletal Muscle: Form and Function*. 2nd. Champaign, IL: Human Kinetics, 2006. DOI: 10.5040/9781492596912 (cit. on p. 26).

[24] David Exeter and David A. Connell. «Skeletal Muscle: Functional Anatomy and Pathophysiology». In: *Seminars in Musculoskeletal Radiology* 14.2 (June 2010). Epub 2010 May 18, pp. 97–105. DOI: 10.1055/s-0030-1253154 (cit. on p. 26).

[25] GeeksforGeeks. *Sliding Filament Theory*. Accessed: March 10, 2025. 2024. URL: https://www.geeksforgeeks.org/sliding-filament-theory/ (cit. on p. 28).

[26] Insights of Nature. *Muscle Series Part 3: The Sliding Filament Theory of Muscle Contraction*. Accessed: March 10, 2025. 2024. URL: https://medium.com/insights-of-nature/muscle-series-part-3-the-sliding-filament-theory-of-muscle-contraction (cit. on p. 29).

[27] David Aitchison Smith. *The Sliding-Filament Theory of Muscle Contraction*. Berlin, Germany: Springer, 2018 (cit. on p. 27).

[28] Y. Avissar, J.H. Choi, C. Rye, J. DeSaix, OpenStax College, V. Jurukovski, Rice University, and R.R. Wise. *Biology*. Online access: Center for Open Education Open Textbook Library. OpenStax College, Rice University, 2013. ISBN: 9781938168093. URL: https://books.google.it/books?id=iG4sngEACAAJ (cit. on p. 30).

[29] M Aubier and N Viires. «Calcium ATPase and respiratory muscle function». In: *European Respiratory Journal* 11.3 (1998), pp. 758–766. ISSN: 0903-1936. DOI: 10.1183/09031936.98.11030758. eprint: https://erj.ersjournals.com/content/11/3/758.full.pdf. URL: https://erj.ersjournals.com/content/11/3/758 (cit. on p. 28).

[30] Dinesh Bhatia, Gagan Bansal, R.P. Tewari, and K.K. Shukla. «State of Art: Functional Electrical Stimulation (FES)». In: *International Journal of Biomedical Engineering and Technology* 5.1 (2011). Copyright © 2011 Inderscience Enterprises Ltd., pp. 77–92 (cit. on pp. 31, 33).

[31] M. S. Sung, J. Y. Hong, Y. H. Choi, S. H. Baik, and H. Yoon. «FES-biofeedback versus intensive pelvic floor muscle exercise for the prevention and treatment of genuine stress incontinence». In: *Journal of Korean Medical Science* 15.3 (June 2000), pp. 303–308. DOI: 10.3346/jkms.2000.15.3.303 (cit. on p. 31).

[32] Shiyu Luo, Haonan Xu, Yi Zuo, Xiaogang Liu, and Angelo All. «A Review of Functional Electrical Stimulation Treatment in Spinal Cord Injury». In: *NeuroMolecular Medicine* 22 (Dec. 2020). DOI: 10.1007/s12017-019-08589-9 (cit. on p. 32).

[33] A. Prestia, F. Rossi, A. Mongardi, P. M. Ros, M. R. Roch, M. Martina, and D. Demarchi. «Motion Analysis for Experimental Evaluation of an Event-Driven FES System». In: *IEEE Transactions on Biomedical Circuits and Systems* 16.1 (Feb. 2022), pp. 3–14. DOI: 10.1109/TBCAS.2021.3137027. URL: https://doi.org/10.1109/TBCAS.2021.3137027 (cit. on pp. 34, 71).

[34] Fabio Rossi, Andrea Mongardi, Paolo Motto Ros, Massimo Ruo Roch, Maurizio Martina, and Danilo Demarchi. «Tutorial: A Versatile Bio-Inspired System for Processing and Transmission of Muscular Information». In: *IEEE Sensors Journal* PP (Aug. 2021), pp. 1–1. DOI: 10.1109/JSEN.2021.3103608 (cit. on pp. 34, 35, 37, 71).

[35] Aegis Softtech. *MLOps Revolution: The Game-Changer for Machine Learning Model Development and Deployment*. Accessed: March 10, 2025. URL: https://www.aegissofttech.com/insights/mlops-revolution-ml-model/ (cit. on p. 38).

[36] Yuan Chengping and Michel Fathi. «Reinforcement Learning: Beyond the Basal Ganglia». In: (Apr. 2021). DOI: 10.1007/978-3-030-84729-6_16 (cit. on p. 40).

[37] Steven Walczak and Narciso Cerpa. «Artificial Neural Networks». In: *Encyclopedia of Physical Science and Technology (Third Edition)*. Ed. by Robert A. Meyers. Third Edition. New York: Academic Press, 2003, pp. 631–645. ISBN: 978-0-12-227410-7. DOI: https://doi.org/10.1016/B0-12-227410-5/00837-1. URL: https://www.sciencedirect.com/science/article/pii/B0122274105008371 (cit. on pp. 39, 40).

[38] Knoldus Blogs. *Architecture of Artificial Neural Network*. Accessed: March 10, 2025. URL: https://blog.knoldus.com/architecture-of-artificial-neural-network/ (cit. on p. 41).

[39] Vipin Kumar and Sonajharia Minz. «Feature selection: A literature review». In: *Smart Computing Review* 4 (Jan. 2014), pp. 211–229. DOI: 10.1145/2740070.2626320 (cit. on p. 40).

[40] Verónica Bolón-Canedo, Noelia Sánchez-Maroño, and Amparo Alonso-Betanzos. «A review of feature selection methods on synthetic data». In: *Knowledge and Information Systems* 34.3 (Mar. 2013), pp. 483–519 (cit. on p. 41).

[41] A. Jović, K. Brkić, and N. Bogunović. «A review of feature selection methods with applications». In: *2015 38th International Convention on Information and Communication Technology, Electronics and Microelectronics (MIPRO)*. 2015, pp. 1200–1205. DOI: 10.1109/MIPRO.2015.7160458 (cit. on pp. 41, 42).

[42] S. Maldonado, R. Weber, and F. Famili. «Feature selection for high-dimensional class-imbalanced data sets using Support Vector Machines». In: *Information Sciences* 286 (2014), pp. 228–246 (cit. on p. 41).

[43] Andrzej Maćkiewicz and Waldemar Ratajczak. «Principal components analysis (PCA)». In: *Computers & Geosciences* 19.3 (1993), pp. 303–342. ISSN: 0098-3004. DOI: https://doi.org/10.1016/0098-3004(93)90090-R. URL: https://www.sciencedirect.com/science/article/pii/009830049390090R (cit. on p. 42).

[44] Tao Song, Zhe Yan, Shuai Guo, Yuwen Li, Xianhua Li, and Fengfeng Xi. «Review of sEMG for Robot Control: Techniques and Applications». In: *Applied Sciences* 13.17 (2023). ISSN: 2076-3417. DOI: 10.3390/app13179546. URL: https://www.mdpi.com/2076-3417/13/17/9546 (cit. on p. 43).

[45] Cometa Systems. *Cometa Systems*. Accessed: March 10, 2025. URL: https://www.cometasystems.com/?utm_term=cometa%20systems&utm_campaign=Wave%20Italia&utm_source=adwords&utm_medium=ppc&hsa_acc=2218685127&hsa_cam=78989008&hsa_grp=2690818288&hsa_ad=561899914206&hsa_src=g&hsa_tgt=kwd-26713972288&hsa_kw=cometa%20systems&hsa_mt=b&hsa_net=adwords&hsa_ver=3&gad_source=1&gc

lid=Cj0KCQiAkoe9BhDYARIsAH85cDM0znRWzh2cmK7HAcMh9R3RwSCezo3jPI_Ww6FkZBRiVFNqJacq3rgaAnLCEALw_wcB (cit. on p. 43).

[46] Biometrics Ltd. *Surface EMG Sensor*. Accessed: March 10, 2025. URL: https://www.biometricsltd.com/surface-emg-sensor.htm (cit. on p. 44).

[47] Marco Crepaldi, Marco Paleari, Alberto Bonanno, Alessandro Sanginario, Paolo Ariano, Duc Hoa Tran, and Danilo Demarchi. «A quasi-digital radio system for muscle force transmission based on event-driven IR-UWB». In: *2012 IEEE Biomedical Circuits and Systems Conference (BioCAS)*. 2012, pp. 116–119. DOI: 10.1109/BioCAS.2012.6418406 (cit. on p. 45).

[48] Fabio Rossi, Ricardo Rosales, Paolo Motto Ros, and Danilo Demarchi. «Real-Time Embedded System for Event-Driven sEMG Acquisition and Functional Electrical Stimulation Control». In: Mar. 2020, pp. 207–212. ISBN: 978-3-030-37276-7. DOI: 10.1007/978-3-030-37277-4_24 (cit. on p. 46).

[49] Andrea Mongardi, Fabio Rossi, Andrea Prestia, Paolo Motto Ros, Massimo Ruo Roch, Maurizio Martina, and Danilo Demarchi. «Hand Gestures Recognition for Human-Machine Interfaces: A Low-Power Bio-Inspired Armband». In: *IEEE Transactions on Biomedical Circuits and Systems* 16.6 (2022), pp. 1348–1365. DOI: 10.1109/TBCAS.2022.3211424 (cit. on pp. 46–48).

[50] Andrea Prestia, Fabio Rossi, Andrea Mongardi, Paolo Motto Ros, Massimo Ruo Roch, Maurizio Martina, and Danilo Demarchi. «Motion Analysis for Experimental Evaluation of an Event-Driven FES System». In: *IEEE Transactions on Biomedical Circuits and Systems* 16.1 (2022), pp. 3–14. DOI: 10.1109/TBCAS.2021.3137027 (cit. on pp. 46, 49).

[51] Davinder Kumar and Aman Ganesh. «A Critical Review on Hand Gesture Recognition using sEMG: Challenges, Application, Process and Techniques». In: *Journal of Physics: Conference Series* 2327 (Aug. 2022), p. 012075. DOI: 10.1088/1742-6596/2327/1/012075 (cit. on p. 47).

[52] Wei Li, Ping Shi, and Hongliu Yu. «Gesture Recognition Using Surface Electromyography and Deep Learning for Prostheses Hand: State-of-the-Art, Challenges, and Future». In: *Frontiers in Neuroscience* 15 (2021). ISSN: 1662-453X. DOI: 10.3389/fnins.2021.621885. URL: https://www.frontiersin.org/journals/neuroscience/articles/10.3389/fnins.2021.621885 (cit. on pp. 47, 48, 51).

[53] Nawadita Parajuli et al. «Real-Time EMG Based Pattern Recognition Control for Hand Prostheses: A Review on Existing Methods, Challenges and Future Implementation». In: *Sensors* 19.20 (2019). ISSN: 1424-8220. DOI: 10.3390/s19204596. URL: https://www.mdpi.com/1424-8220/19/20/4596 (cit. on p. 47).

[54] H. Yu, X. Fan, L. Zhao, and X. Guo. «A novel hand gesture recognition method based on 2-channel sEMG». In: *Technology and Health Care* 26.S1 (2018), pp. 205–214. DOI: 10.3233/THC-174567 (cit. on pp. 49, 50).

[55] Zhen Ding, Chifu Yang, Zhihong Tian, Chunzhi Yi, Yunsheng Fu, and Feng Jiang. «sEMG-Based Gesture Recognition with Convolution Neural Networks». In: *Sustainability* 10 (June 2018), p. 1865. DOI: 10.3390/su10061865 (cit. on p. 49).

[56] Manfredo Atzori and Henning Müller. «The Ninapro database: a Resource for sEMG Naturally Controlled Robotic Hand Prosthetics». In: *Proceedings of the 2015 Myoelectric Controls Symposium (MEC)*. Vol. 2015. Aug. 2015. DOI: 10.1109/EMBC.2015.7320041 (cit. on p. 50).

[57] H. Wang, Y. Zhang, C. Liu, et al. «sEMG based hand gesture recognition with deformable convolutional network». In: *International Journal of Machine Learning and Cybernetics* 13 (2022), pp. 1729–1738. DOI: 10.1007/s13042-021-01482-7 (cit. on p. 50).

[58] Simon Tam, Mounir Boukadoum, Alexandre Campeau-Lecours, and Benoit Gosselin. «A Fully Embedded Adaptive Real-Time Hand Gesture Classifier Leveraging HD-sEMG and Deep Learning». In: *IEEE Transactions on Biomedical Circuits and Systems* 14.2 (Apr. 2020), pp. 209–220. DOI: 10.1109/TBCAS.2020.2973456 (cit. on pp. 50, 51).

[59] Cheng Shen, Zhongcai Pei, Weihai Chen, Jianhua Wang, Jianbin Zhang, and Zuobing Chen. «Toward Generalization of sEMG-Based Pattern Recognition: A Novel Feature Extraction for Gesture Recognition». In: *IEEE Transactions on Instrumentation and Measurement* 71 (2022), pp. 1–12. DOI: 10.1109/TIM.2022.3141163 (cit. on p. 51).

[60] Kunkun Zhao, Zhisheng Zhang, Haiying Wen, and Alessandro Scano. «Intra-Subject and Inter-Subject Movement Variability Quantified with Muscle Synergies in Upper-Limb Reaching Movements». In: *Biomimetics* 6.4 (2021). ISSN: 2313-7673. DOI: 10.3390/biomimetics6040063. URL: https://www.mdpi.com/2313-7673/6/4/63 (cit. on p. 51).

[61] Yuzhou Lin, Ramaswamy Palaniappan, Philippe De Wilde, and Ling Li. «A normalisation approach improves the performance of inter-subject sEMG-based hand gesture recognition with a ConvNet». In: *2020 42nd Annual International Conference of the IEEE Engineering in Medicine & Biology Society (EMBC)*. 2020, pp. 649–652. DOI: 10.1109/EMBC44109.2020.9175156 (cit. on pp. 51, 52).

[62] Anke IR Kottink, Hermie J Hermens, Anand V Nene, Martin J Tenniglo, Catharina G Groothuis-Oudshoorn, and Maarten J IJzerman. «Therapeutic Effect of an Implantable Peroneal Nerve Stimulator in Subjects With Chronic Stroke and Footdrop: A Randomized Controlled Trial». In: *Physical Therapy* 88.4 (Apr. 2008), pp. 437–448. ISSN: 0031-9023. DOI: 10.2522/ptj.20070035. eprint: https://academic.oup.com/ptj/article-pdf/88/4/437/31666850/ptj0437.pdf. URL: https://doi.org/10.2522/ptj.20070035 (cit. on p. 52).

[63] N Kapadia, B Moineau, and MR Popovic. «Functional Electrical Stimulation Therapy for Retraining Reaching and Grasping After Spinal Cord Injury and Stroke». In: *Frontiers in Neuroscience* 14 (July 2020), p. 718. DOI: 10.3389/fnins.2020.00718 (cit. on p. 53).

[64] RehaMove2. *RehaMove2 User Manual*. Accessed: March 10, 2025. URL: https://static1.squarespace.com/static/5f16af2c5732983b810510ef/t/625445ebc1f33f681fa9ec3e/1649690115682/RehaMove2_User+Manual_2.4._ENG_CM_20170201.pdf (cit. on p. 54).

[65] SB O'Dwyer, DT O'Keeffe, S Coote, and G Lyons. «An electrode configuration technique using an electrode matrix arrangement for FES-based upper arm rehabilitation systems». In: *Medical Engineering & Physics* 28.2 (2006), pp. 166–176. DOI: 10.1016/j.medengphy.2005.07.008 (cit. on p. 54).

[66] M Goffredo, M Schmid, S Conforto, F Bilotti, C Palma, L Vegni, and T D'Alessio. «A two-step model to optimise transcutaneous electrical stimulation of the human upper arm». In: *COMPEL - The international journal for computation and mathematics in electrical and electronic engineering* 33.4 (2014), pp. 1329–1345. DOI: 10.1108/COMPEL-06-2013-0185 (cit. on p. 54).

[67] FESIA Technology. *FESIA Grasp*. Accessed: March 10, 2025. URL: https://fesiatechnology.com/en/fesia-grasp/ (cit. on pp. 54, 55).

[68] A Martin-Odriozola, C Rodríguez-de-Pablo, A Caceres-Salegi, A García-Calleja, JI Marín-Ojea, E Hernández, E Imatz-Ojanguren, T Keller, and H Zabaleta-Rekondo. «Analysis of the movements generated by a multi-field functional electrical stimulation device for upper extremity rehabilitation». In: *Artificial Organs* 46.10 (Oct. 2022), pp. 2027–2033. DOI: 10.1111/aor.14346. eprint: 2022Jun29 (cit. on p. 55).

[69] C De Marchis, T Santos Monteiro, C Simon-Martinez, et al. «Multi-contact functional electrical stimulation for hand opening: electrophysiologically driven identification of the optimal stimulation site». In: *Journal of NeuroEngineering and Rehabilitation* 13.1 (2016), p. 22. DOI: 10.1186/s12984-016-0129-6 (cit. on pp. 55, 56).

[70] L Popović-Maneski and I Topalović. «EMG Map for Designing the Electrode Shape for Functional Electrical Therapy of Upper Extremities». In: *Converging Clinical and Engineering Research on Neurorehabilitation III, Proceedings of the 4th International Conference on NeuroRehabilitation (ICNR2018)*. Pisa, Italy: Springer, Oct. 2018, pp. 1003–1007 (cit. on pp. 55, 56).

[71] I. Lypunova Petersen, W. Nowakowska, C. Ulrich, and L. N. S. Andreasen Struijk. «A Novel sEMG Triggered FES-Hybrid Robotic Lower Limb Rehabilitation System for Stroke Patients». In: *IEEE Transactions on Medical Robotics and Bionics* 2.4 (Nov. 2020). Member, IEEE, p. 631 (cit. on p. 56).

[72] Xinyu Jiang, Xiangyu Liu, Jiahao Fan, Xinming Ye, Chenyun Dai, Edward A. Clancy, Metin Akay, and Wei Chen. «Open Access Dataset, Toolbox and Benchmark Processing Results of High-Density Surface Electromyogram Recordings». In: *IEEE Transactions on Neural Systems and Rehabilitation Engineering* 29 (2021), pp. 1035–1046. DOI: 10.1109/TNSRE.2021.3082551 (cit. on pp. 59, 81).

[73] Abhishek Pradhan, Jing He, and Ning Jiang. «Multi-day dataset of forearm and wrist electromyogram for hand gesture recognition and biometrics». In: *Scientific Data* 9 (2022), p. 733. DOI: 10.1038/s41597-022-01752-7. URL: https://www.nature.com/articles/s41597-022-01752-7 (cit. on pp. 62, 63).

[74] Nordic Semiconductor. *nRF52840 Dongle*. Accessed: March 10, 2025. URL: https://www.nordicsemi.com/Products/Development-hardware/nRF52840-Dongle (cit. on p. 70).

[75] Python Software Foundation. *Pyserial*. Accessed: March 10, 2025. URL: https://pypi.org/project/pyserial/ (cit. on p. 73).

[76] University of Turin. *Comitato di Bioetica dell'Ateneo*. Accessed: March 10, 2025. URL: https://www.unito.it/ricerca-e-innovazione/fare-ricerca-unito/comitato-di-bioetica-dellateneo (cit. on p. 89).

[77] Néstor J. Jarque-Bou, Margarita Vergara, and Joaquín L. Sancho-Bru. «Does Exerting Grasps Involve a Finite Set of Muscle Patterns? A Study of Intra- and Intersubject Variability of Forearm sEMG Signals in Seven Grasp Types». In: *IEEE Transactions on Neural Systems and Rehabilitation Engineering* 32 (2024), pp. 1505–1514. DOI: 10.1109/TNSRE.2024.3383156 (cit. on p. 92).

[78] Patrick Kaifosh and Thomas R. Reardon. «A generic noninvasive neuromotor interface for human-computer interaction». In: *bioRxiv* (2024). CTRL-labs at Reality Labs (cit. on p. 116).